ENHANCING SAR SHIP WAKE DETECTION WITH MOTION ESTIMATES FROM ALONG-TRACK INTERFEROMETRY

by

TERRY NGO, CD., P.ENG.

B. A. Sc. Elec Eng, University of British Columbia 1990

A THESIS SUBMITTED IN PARTIAL FULFILLMENT OF

THE REQUIREMENTS FOR THE DEGREE OF

MASTER OF APPLIED SCIENCE

in

THE FACULTY OF GRADUATE STUDIES

DEPARTMENT OF ELECTRICAL ENGINEERING

We accept this thesis as conforming

to the required standard

THE UNIVERSITY OF BRITISH COLUMBIA

Aug 1997

In presenting this thesis in partial fulfilment of the requirements for an advanced degree at the University of British Columbia, I agree that the Library shall make it freely available for reference and study. I further agree that permission for extensive copying of this thesis for scholarly purposes may be granted by the head of my department or by his or her representatives. It is understood that copying or publication of this thesis for financial gain shall not be allowed without my written permission.

Department of ELECTRICAL ENGINEERING

The University of British Columbia
Vancouver, Canada

Date 8 SEP 97

DE-6 (2/88)

Abstract

A difficult problem in remote sensing is the detection of ships on the open ocean. For almost two decades, experimental spaceborne and airborne Synthetic Aperture Radars (SAR) have been used to image ships. However, SAR is inherently limited in (automated) ship detection because it relies on a single parameter, the radar Backscatter, to distinguish faint, small ship signatures from background. Along-Track Interferometry, a recently developed technique that uses two time displaced SAR images (from two along-track displaced antennas) to extract velocity estimates of the surface, holds some promise in enhancing the capability of SAR.

In this study, we examined the Along-Track Interferometry technique in detail and attempted to assign quantitative measures of its enhancement potential to SAR in ship wake detection. Specifically, we used representative data from an experimental airborne SAR ATI, the Canada Centre for Remote Sensing (CCRS) CV580 C-Band SAR ATI, to examine the effects of ATI processing on: a) the visual appearance of Backscatter and motion signatures of ships and ship wakes in magnitude and phase components of ATI images b) the (quantitative) detectability of ships and their wakes by Backscatter and motion; and c) the characteristics of the Backscatter and motion signatures, such as their spectra, coherence, and signal distribution. And we attempted to determine from our analysis and simulation/modeling, a quantitative measure of the potential of ATI to enhance SAR's performance in ship detection.

The results of this study suggest that Along Track Interferometry is capable of enhancing ship wake detection. Specifically, we found that: a) airborne SAR ATI is able to estimate differential (radial) velocity with sufficient accuracy to detect appreciable disturbances of the velocity field of the ocean, and that b) ship wakes, under the conditions of the data collected, were able to sufficiently disturb the velocity field of the ocean surface to be discriminated from ambient ocean structure. This study also suggests that in some circumstances, certain ocean features which may not have been detectable from its Backscatter by a conventional SAR, could be detected from its motion by ATI. And lastly, this study demonstrates that the additional, and in some cases singularly unique, motion information provided by ATI, when fused or combined with conventional Backscatter information, can indeed yield improved detection of ships and wakes overall by the SAR sensor.

Table of Contents

List of Tables

List of Figures

Acknowledgment

I would like to thank my supervisor, Professor Ian Cumming, and co-supervisor, Maria Rey of the DREO, for providing me with this opportunity to work in this fascinating and challenging field of research: Prof. Cumming for his knowledge of SAR and academic guidance; and Maria Rey for her invaluable advise and access to data at the DREO and CCRS.

I would also like to thank Dr. Lawrence Gray and Dr. John Campbell of the CCRS for their technical advise and provision of data and other information crucial to this work, CICSR Director, Prof. Rabab Ward, for her constant encouragement of graduate students, and my fellow students for their support and friendship during my time here at UBC.

But most of all I'd like to express my gratitude to my family for their lifelong encouragement and support; and especially my mother who taught me from childhood to find joy in every matter of learning.

The work of this study was conducted in collaboration with the Defence Research Establishment Ottawa (DRE0) at the Natural Science Engineering Research Council (NSERC) and MacDonald Detwiller & Associates (MDA) sponsored laboratory in Radar Remote Sensing at the University of British Columbia's (UBC) Centre for Integrated Systems Research (CICSR).

Chapter 1 Introduction

The following document is a thesis report on research carried out towards a Master of Applied Science degree at the University of British Columbia in the Department of Electrical Engineering. The work covered in this report was conducted in collaboration with the Defence Research Establishment Ottawa (DREO). The major results of this work have been submitted to the DREO under cover of four Technical Notes [1] [2] [3] [4] and a final report [5].

1.1 Motivation

A difficult problem in remote sensing is the detection of ships on the open ocean by airborne and spaceborne platforms. From such altitudes, ships are very small against the vast (relative) emptiness of the ocean. And they are difficult to discriminate from the surrounding waves; which can often be several times larger than even the largest ships. The difficulty in detecting small ships in a large ocean is further complicated by darkness and the frequently poor weather and dense cloud cover that blankets much of the world's oceans.

When first introduced as the experimental Seasat in 1978, Synthetic Aperture Radar (SAR), a high resolution active sensor that marries radar and advanced signal processing technologies, offered the promise of a best solution to this problem. Because SAR uses active RAdio Detection And Ranging (RADAR), it is immune to the effects of darkness, weather and cloud cover, and because it uses highly efficient digital signal processing, it is able to achieve very high resolutions over large imaged areas. Indeed, some of the earliest images of the ocean produced by Seasat, many of which were taken at night and in poor weather, contained ship targets which became some of the first images of ships seen from space. Current state-of-the-art SAR sensors like ERS-1/2, Radarsat, the Canadian Armed Forces experimental Spotlight SAR, and the CCRS CV580 SAR routinely produce high quality images of ocean scenes which contain surprisingly clear and distinct images of medium and large sized ship targets. However, despite SAR's unique, and arguably superior, ability over other remote sensor technologies to image ships over a vast search area in darkness and poor weather, SAR has significant limitations which prevent its more widespread use as a ship detector in other than experimental systems. The first is that it is highly computationally intensive. Most current systems must employ off-line focusing and detection processing; using very large general purpose computers and often taking several hours to produce a single image and detect ship targets in it. Real-time systems are currently beyond the realm of practicality for all but the largest and most expensive SAR platform; the USAF E-8C JSTARS. Even using the best SAR images,

requiring frightening amounts of computing power to achieve the best resolution and clarity, the false alarm rate in ship detection mode is often unacceptably high and practical ship detection cannot be attempted without the intervention of highly skilled human interpreters.

We believe that SAR, like other radio wave based detection systems such as conventional radar, is fundamentally limited by its reliance on just the radio wave Backscatter signature of features to image scenes and detect targets. In ship detection, this is particularly true because a ship's Backscatter signature is quite small on an ocean surface, which is itself a large reflector of radio energy. However, in recent years, a new technique has emerged which we believe holds some promise in enhancing the capability of SAR to better address the ship detection problem. This technique, called Along-Track Interferometry (ATI), uses two or more SAR images of the same scene, simultaneously acquired by two laterally displaced antennas (or a split antenna with two displaced phase centres) on the same sensor, to estimate the radial velocity of scatterers in the scene. The resulting high resolution velocity estimate yields motion information about the scene and moving targets in it. Because moving ships can generate large wake disturbances which may be significantly differentiated from the surrounding ocean, such a high resolution motion estimate could offer a unique enhanced capability to SAR; allowing it to detect moving ships by both their Backscatter and motion signatures. We believe that using the motion estimate from ATI can significantly reduce the false alarm rate of ship detection by SAR, allowing lower resolution SAR images, which require significantly smaller computation (and possibly produced in real-time) to achieve acceptable ship detection performance.

1.2 Objectives of the Research

The objective of this study was to examine the technique of Along-Track Interferometry (ATI) applied to Synthetic Aperture Radar (SAR) and investigate the potential of this technique in enhancing the detection of ship wakes from airborne SAR sensors. SAR Along-Track Interferometry, also called Displaced Phase Centre Aperture (DPCA) SAR, is a relatively new technique in radar remote sensing. It has been used successfully in experimental systems to study natural ocean features, such as ocean currents and waves, and it is operational employed in advanced Moving Target Indication (MTI) systems such as that on the United States Air Force (USAF) E-8C JSTARS (Joint Surveillance and Target Attack Radar System) aircraft [6].

One of the challenges of modern remote sensing is the efficient search, detection and classification of ships over large search areas of the ocean. This is particularly important to a maritime nation like

Canada, whose territory straddles the world's three largest oceans. Maintaining constant (day/night, all weather) observation over 243,000 km of coastline (the longest in the world), tracking a large number and variety of shipping to maintain sovereignty over territory and environment, is a monumental task that can only be accomplished with the help of advanced remote sensors capable of detecting ships quickly and accurately. For this purpose, Canada has, over the years, developed and employed a number of advanced airborne and spaceborne SAR sensors, which include the CCRS (experimental) airborne SAR, the recently launched Radarsat spaceborne SAR, and the currently-in-development Spotlight SAR upgrade to the CP-140 maritime patrol aircraft fleet. However, there are some significant limitations to these SAR sensors in specifically detecting ships. This is because conventional SAR, like conventional radar, principally relies on the radio wave Backscatter of a target to find it in a vast ocean scene and discriminate it from the surrounding clutter. Although, the metal corner reflector-like surfaces of a ship's superstructure, and to a lesser degree, it's hull give very strong radar returns and normally show up as quite bright in SAR imagery, the ambient ocean is quite often bright itself, either throughout or in important regions, due to a high incidence angle (of the sensor) or high surface wind action. Additionally, ships are quite small in comparison to the vast dimensions of an ocean scene. Even a large ship, on the order of say 100m in length and 30m wide, would only represent a very small fraction (about $3x10^{-5}$ percent) of the data space of a typical SAR imaged scene, which can typically cover a surface area of approximately 100 km by 100 km. At a typical resolution of 6m x 25m (6m x 40m slant range) per pixel for an ERS-1 spaceborne SAR image, such a ship would be represented by less than 20 pixels in an image of over 67 million pixels! This is called the small ship/large ocean problem and is a very difficult challenge for sensors employed in ship detection.

One important observation of ships is that all moving ships leave a distinctive trail, called a wake. This wake can serve as a unique signature of an unnatural event (i.e. the ship's traverse) across a background containing only otherwise naturally generated clutter. Additionally, the wake signature of a moving ship can be quite large, being from 20 to 100 times longer and 10-20 times wider than the length and width of the ship itself, making it a much larger target than the signature (i.e. such as Backscatter) of just superstructure and hull. Thus in a typical remote sensor image, a ship's wake would represent a much larger percentage of the data space than the ship by itself. However, wakes because they are a result of the interaction of ship and ocean have physical characteristics so similar to that of the surrounding ocean, that the contrast of their signature (i.e. Backscatter) against the background ocean is much less than that of a ship's hull and superstructure; making them inconsistent detection indicators at best.

Another important observation is that moving ships and their moving wakes are just that...moving.

Thus their inherent and unique (i.e. unnatural, man-made) motion signature or velocity profile should make them quite differentiated from the natural motion or general stationarity of the ambient ocean; even when the contrast of any other signature (i.e. Backscatter) isn't great, if a ship is moving, then its motion signature should be quite substantial.

These two important observations would indicate that, given an appropriate sensor which could detect differential motion of both ship and wake and appropriate detection schemes which could exploit the longer and wider dimensions of ship wakes, the detection of ship wakes by conventional SAR could be improved.

In 1987, Goldstein and Zebker of NASA's Jet Propulsion Labs, demonstrated that a SAR sensor with two displaced phase centres could produce interferograms whose phase component contained motion information [7]. Their first images were of the Northern California coastline where they showed that tidal currents and internal waves could be quite easily distinguished from the background ocean by motion alone. In Canada, this work has been continued and extended by the Canada Centre for Remote Sensing (CCRS) which has shown that other complex ocean features, such as surface and subsurface travelling waves and internal wave features associated with submerged structures (such as sand dunes), can also be imaged by their velocity signatures. Recently, the DND and DREO have extended this work to include the investigation of the potential application of ATI in enhanced airborne SAR sensors that detect ships by their motion and wake. The work of this study was a part of this investigation and sought to determine the ship detection enhancement capability of ATI by examining the ATI processing technique and measuring and comparing the Backscatter and motion signatures of ships and wakes. To our knowledge, a quantitative comparison of the detectability of the ship and wake features by their Backscatter and motion signatures has not been investigated to date.

The specific goals of our research were to determine:

1. if airborne SAR ATI is able to estimate differential velocity with sufficient accuracy to detect appreciable disturbances of the velocity field of the ocean;
2. if ship wakes, under the conditions of the data collected, are able to sufficiently disturb the velocity field of the ocean surface to be discriminated from ambient ocean structure (by SAR ATI); and
3. whether the additional motion information provided by ATI would be able to improve the detection of ship wakes by SAR.

In order to accomplish this, representative data from an experimental SAR ATI sensor, the CCRS

airborne C-band SAR ATI, was processed and analyzed. The effects of ATI processing on the visual presentation and quantitative (numeric) and qualitative (visual) detectability of ship and wake targets in the Backscatter and phase components of interferograms, as well as on the spectrum, coherence, and signal information distribution was examined by direct analysis of the raw SAR data and processed interferograms. Simulations and models were built and used where necessary. And the performance of a typical target detector (a CA-CFAR detector) to detect ships, ship wakes and other significant ocean features, was measured. Additionally, a simple fusion of the detected Backscatter and motion signatures was briefly attempted to demonstrate the practical application of the additional motion information provided by ATI to improving overall detection of ships and wakes.

1.3 Outline of the Report

This thesis report is composed of the following chapters and attachments:

- **Chapter 2: Background**. Reviews the basic principles of SAR and Along-Track Interferometry.
- **Chapter 3: Interferogram Processing Analysis**. Describes the CCRS C-band data set and the methods used to generate the ATI interferograms used in the subsequent analysis. The effect of the different ATI processes and parameters used in ATI interferogram formation on the Backscatter magnitude and motion bearing phase information of the resulting interferogram is examined.
- **Chapter 4: Signal Information Analysis**. Examines scene and surface target information content of ATI interferograms. The effect of the dual antenna ATI configuration and the correlation operations of the ATI interferogram formation process is examined from the signal statistics of ATI phase and magnitude images. Observed results are compared with a simulation model.
- **Chapter 5: Theoretical Performance**. Examines the theoretical performance of C-band ATI systems from parametric analysis.
- **Chapter 6: Detection Performance Analysis**. A detection performance figure of merit is established and the detectability and detection potential of ship and wake targets in Backscatter and motion imagery are quantified and compared.
- **Chapter 7: Conclusions.** Summarizes the main results and conclusions of the study.

- **Appendix A: SAR Imaging Mechanisms of Ship Wakes**. Describes the physical mechanism by which radar and SAR image ocean features.
- **Appendix B: Feature Detection**. Describes the detection principles and feature detectors used in the analysis of this report.
- **Appendix C: Catalogue of Data Sets (Scenes)**. Provides a visual catalogue and detailed description of the data set used in the analysis of this report.
- **Appendix D: Filtered and Unfiltered Chip Images**. Provides a visual catalogue of filtered and unfiltered Backscatter intensity and phase images used in the analysis of this report.
- **Appendix E.: Signal and Statistics of Targets**. Lists the observed Backscatter and phase signal measurements and calculated signal statistics of background, targets and features in the data set and processed images.
- **Appendix F: CFAR Detection Results**. Provides a visual catalogue of the results of a CA-CFAR detector's performance on the Backscatter and motion images of representative chip images containing ships and wakes and a significant (naturally occurring) ocean feature.

Chapter 2 Background

In order to define the techniques and terms employed in this report, a brief introduction to Synthetic Aperture Radar applied to Along-Track Interferometry is provided. A more detailed discussion of the mechanism by which Ocean features and ship wakes are imaged by SAR is presented in Appendix A.

2.1 Synthetic Aperture Radar

Synthetic Aperture Radar (SAR) is an active imaging system that allows day / night, all weather remote imaging of wide areas of the earth's surface at high resolutions. It is an active microwave sensor and like it's parent technology, conventional radar, SAR uses transmitted microwave energy to illuminate targets in a ground scene. But unlike conventional radar, SAR exploits the relative motion between sensor platform and the ground scene to produce high resolution two-dimensional maps by Digital Signal Processing (DSP) of the Backscatter signal.

Figure 2.1 below shows the basic SAR imaging geometry. Most SAR sensors are side looking with the radar beam pointing into the imaged scene and the sensor platform travelling across it. By definition, the scan direction of the radar parallel to the path of the sensor platform is called the *Azimuth* or the *Along-Track* dimension, while the scan direction that is perpendicular to the platform track is called the *Slant Range*. Projected onto a horizontal plane, this becomes the *Range* dimension. The direction of lines running between the sensor and scatterers is called the *Radial* direction. In this figure, v is the platform velocity in the azimuth direction, t is the azimuth time coordinate (also called slow time), ζ is the range time coordinate (also called fast time), and the position of the platform at its closest approach to the target is, vt_i.

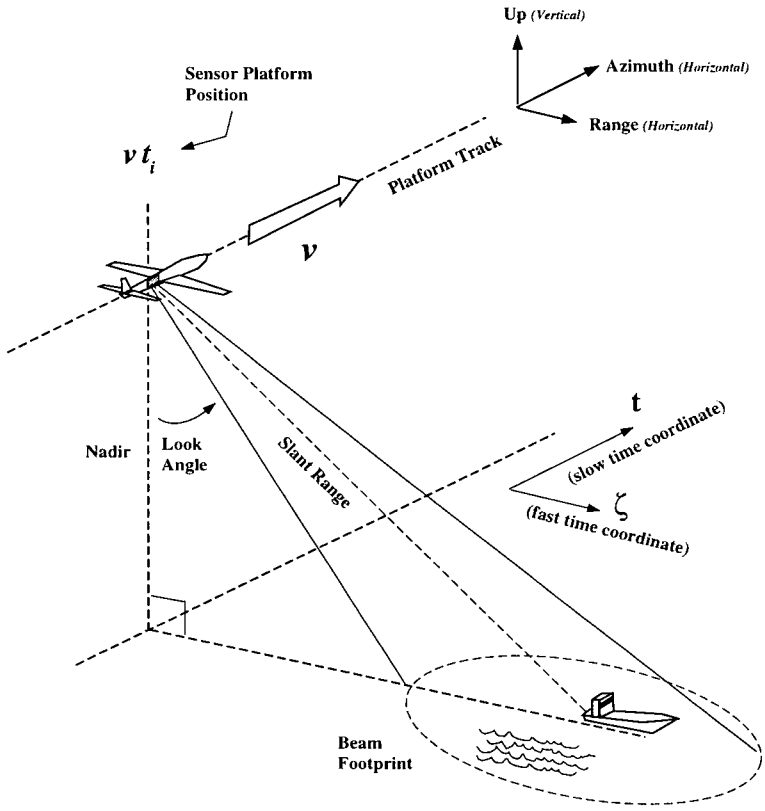

Figure 2.1 Basic SAR Imaging Geometry

The key to SAR's high resolution performance is coherent processing, in which the phase relationship between transmitted pulse and received signal is preserved or coherent from pulse to pulse. This relative phase change, or phase modulation, is due to the Doppler shift resulting from the relative motion of the platform over the scene and is used by a SAR processor to resolve individual scatterers into fine scale azimuth bins to provide the high resolution output images typical of SAR.

We can illustrate this by examining the output image of a coherent radar signal before and after SAR processing. The transmitted signal of such a radar can be expressed as:

$$S(t, \zeta - \zeta_j; r) = W(\theta)p(t - t_i)\exp\left(\frac{-j4\pi r}{\lambda}\right) \tag{2.1}$$

where $W(\theta)$ is the antennas beam pattern, $p(t\text{-}t_j)$ is the coded transmitted pulse (usually of the form of a linear FM or 'chirp' pulse), θ is the look angle, and r is slant range coordinate, which is:

$$r = \frac{1}{2\sin(\theta)} c\zeta \tag{2.2}$$

where C is the speed of light. The received signal, at the platform's instantaneous position t_i called its closest approach azimuth coordinate, can be expressed as a convolution of a the Backscatter of the distribution of point scatterers $\sigma(t_i, \zeta_j)$ on the ground (seen from the position of the closest approach coordinate) and the transmitted signal:

$$d(t_i, \zeta_i) = \iint \sigma(t_i, \zeta_i) S(t - t_i, \zeta - \zeta_i; r) dt_i d\zeta_i \tag{2.3}$$

This is essentially the output image of the coherent radar before any SAR processing and we note that the resolution is quite coarse as the spatial spread of the convolution kernel, $S(t - t_i, \zeta; r)$, which is essentially the 'footprint' of the radar beam on the ground, is quite large at airborne and spaceborne altitudes.

SAR processing can be expressed as the convolution of the received radar signal d(t, ζ) and a coherent matched filter:

$$S^*(t - t_i; \zeta, r) \tag{2.4}$$

The output of the SAR processor then being:

$$i(t_i, \zeta_j; r) = \iint d(t_i, \zeta_j) S^*(t - t_i, \zeta - \zeta_j; r) dt_i d\zeta_j \tag{2.5}$$

or

$$i(t_i, \zeta_j; r) = \iint \sigma(t_i, \zeta_j) [\iint S(t - t_i, \zeta - \zeta_i; r) S^*(t - t_i, \zeta - \zeta_i; r) dt d\zeta] dt_i d\zeta_j \tag{2.6}$$

We note that the term: $[\iint S(t - t_i, \zeta - \zeta_j; r) S^*(t - t_i, \zeta - \zeta_j; r) dt d\zeta]$ is a narrow point spread function. The solution to this equation can be thought of in the form

$$i(t_i, \zeta_j; r) = [\iint (\sigma(t_i, \zeta_j) \cdot \hat{\Phi}(r_j)) F(t - t_i, \zeta - \zeta_j) d\eta d\zeta] = \hat{\sigma}(t_i, \zeta_j) \cdot \hat{\Phi}(r_j) \tag{2.7}$$

where $\hat{\sigma}(t_i, \zeta_j)$ is the SAR Backscatter magnitude image; which is essentially the surface scatterer distri-

bution sampled by a fine grid, $F(t-t_i, \zeta-\zeta_i)$, and $\hat{\Phi}(r_j)$ is the phase distribution of the surface Backscatter, where each element of the distribution has the form $\exp\left(\frac{-j4\pi r}{\lambda}\right)$; this is essentially the phase image of the interferogram.

2.2 Interferometric SAR

Interferometric SAR is a variation of basic SAR, where two or more antennas or phase centres of a single antenna[1] simultaneously acquire images of the same scene, but slightly displaced in the along-track direction. One antenna or phase centre is called the *Forward* antenna and the other called the *Aft* antenna. This dual displaced antennas configuration is shown below as Figure 2.2:

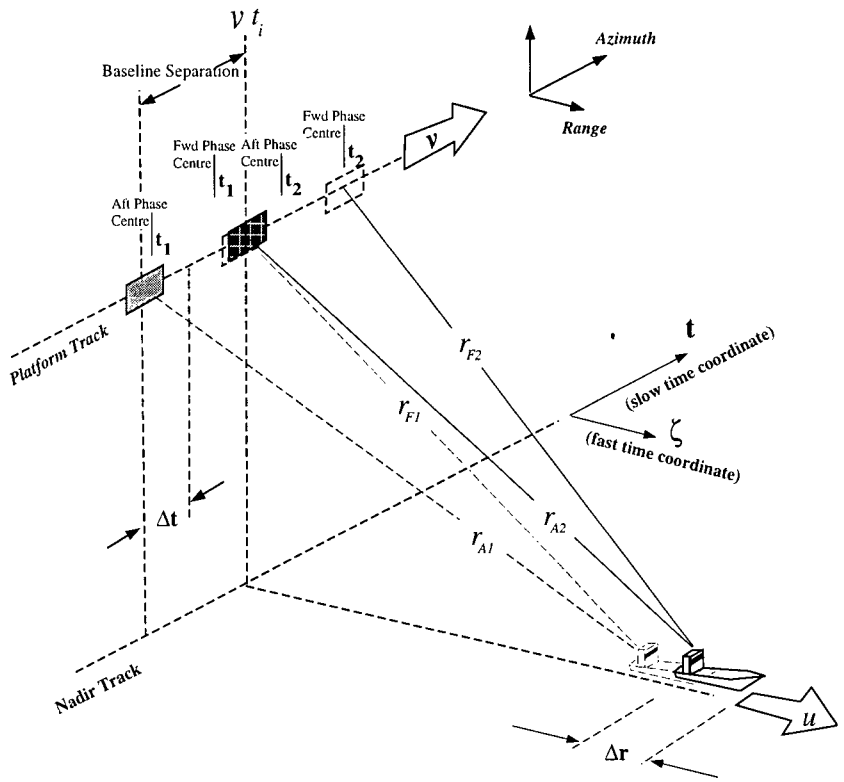

Figure 2.2 Basic SAR ATI Imaging Geometry

[1] also called Displaced Phase Centre Antenna (DPCA)

In this diagram, v is the platform's velocity in the Along-Track direction, u is the radial velocity of a surface target or scatter in the scene, r_{A1} and r_{A2} are the slant range from the aft antenna to the scatterer at times t_1 and t_2 and r_{F1} and r_{F2} are the slant range from the forward antenna to the scatterer at times t_1 and t_2. The spatial separation between the two antennas is called the *Baseline Separation*. This separation distance and the platform velocity results in a time displacement, Δt, between the acquisition of the return signal from the scene at a time t_1 and a short time later, t_2, in which both the platform and the scene have moved. The change in the slant range to a a moving surface target from the time of the forward antennas acquisition of the return signal to the aft antennas acquisition, results in a difference in the phase of the two complex images. We can see this by examining the return signal, after SAR processing, of corresponding forward and aft SLC images. From equation (2.5) and (2.3) we express the time domain and frequency domain expression of the target in the forward image as:

$$i(t_1, \zeta_1)\Big|_{r = r_1} = \hat{\sigma}(t_1, \zeta_1) \cdot \hat{\Phi}(r_1) \Leftrightarrow I\left[-j\left(\omega - \frac{4\pi r_1}{\lambda}\right)\right] \tag{2.8}$$

where t_1 is the closest approach azimuth coordinate of the forward antenna and $\omega = \frac{4\pi r}{\lambda}$. Similarly we can express the target in the aft image as:

$$i(t_2, \zeta_2)\Big|_{r = r_2} = \hat{\sigma}(t_2, \zeta_2) \cdot \hat{\Phi}(r_2) \tag{2.9}$$

where t_2 is the closest approach azimuth coordinate of the aft antenna which has moved a distance of $\Delta r = (\tau_2 - \tau_1)U$ and $r_2 = r_1 - \Delta r$ in time, Δt between closest approach of the two antennas and $r_2 = r_{A2}\cos(\theta)$. However, the two images are acquired simultaneously and the closest approach coordinate of the aft antenna is separated from the closest approach coordinate of the forward antenna by a distance of $v\Delta t = (t_1 - t_2)v$. Expressing the aft equation in the coordinates of the forward image, this becomes:

$$i(t_1 - \Delta t, \zeta_2) = \hat{\sigma}(t_1 - \Delta t, \zeta_2) \cdot \hat{\Phi}(r_1 - \Delta r) \Leftrightarrow \tag{2.10}$$
$$I\left[-j\left(\omega - \frac{4\pi(r_1 - \Delta r)}{\lambda}\right)\right]\exp(-j\omega\Delta t)$$

We can see from (2.8)and (2.10) that there exists a spatial domain phase difference of the form $\Delta\Phi = \frac{4\pi\Delta r}{\lambda}$ between the image pair, which is proportional to the radial velocity of the target $U = \frac{\Delta r}{\Delta t}$, and a frequency domain phase difference of the form $\Delta\Psi = \omega\Delta t$ which is related to the spatial displacement between the Backscatter fields of the two images and the separation between antennas (in the spatial domain, this is called the *spatial misregistration* of the images).

The spatial domain phase difference, which describes the motion of the target, is the primary information of interest in ATI. From the ATI geometry of Figure 2.2, where $\Delta r = \left(\frac{B}{v}\right)U$, we resolve this phase into radial velocity as:

$$U = (\Delta\Phi)\left(\frac{\lambda v}{4\pi B}\right) \tag{2.11}$$

which we call the *ATI equation*. This time domain phase information is extracted by conjugate multiplication or *Mixing*. Thus we can see that the dual displaced antennas of the ATI configuration give us two images, which after SAR focusing and mixing result in an image of the motion in the scene and estimates of the radial motion of moving targets.

The frequency domain phase difference is, however, not immediately useful and if uncorrected, causes phase decorrelation in the mixed image. This frequency domain phase offset can be removed by a *Coregistration* of the two images prior to *Mixing*. From this equation (2.10) we can see that coregistration can be implemented either as an azimuth subsampling in the spatial domain or a phase multiplication in the frequency domain.

We also note that in equation (2.6), the convolution operation of the SAR processor assumes that the ground scene $\sigma(t_i, \zeta_i)$ is stationary and that only the radar is moving (in the azimuth direction) with respect to the coordinate system (t, ζ). However, in practice, the ocean scene can have significant random motion, which if sufficiently large in the azimuth direction can cause defocusing in the image. This can be corrected by an azimuth refocusing operation or alternatively it can partially compensated by an azimuth resampling or realignment process. And additionally, it was assumed in equation (2.10) that the Backscatter field of the two images is relatively unchanged $\hat{\sigma}(t_1, \zeta_1) \approx \hat{\sigma}(t_1 - \Delta t, \zeta_2)$ between closest

approaches. This assumption holds only if the scene remains coherent within the time displacement Δt. In some cases this is not true; either because the platform is moving too slowly with respect to a quickly changing or decorrelating scene or the baseline separation is too large with respect to the velocity of the sensor platform and the wavelength of the radar.

From the above, we can see that the essential steps of ATI processing, from raw radar data acquisition to output of the final interferogram, include: the basic convolution or match filtering processing to form the SLC image pair (called the *SAR processing* or *SAR focussing*), Coregistration of the forward and aft SLC image pair, Mixing of the SLC image pair to form the complex interferogram, and an optional azimuth refocusing process. We show this sequence of processes as a flow diagram in Figure 2.3 below:

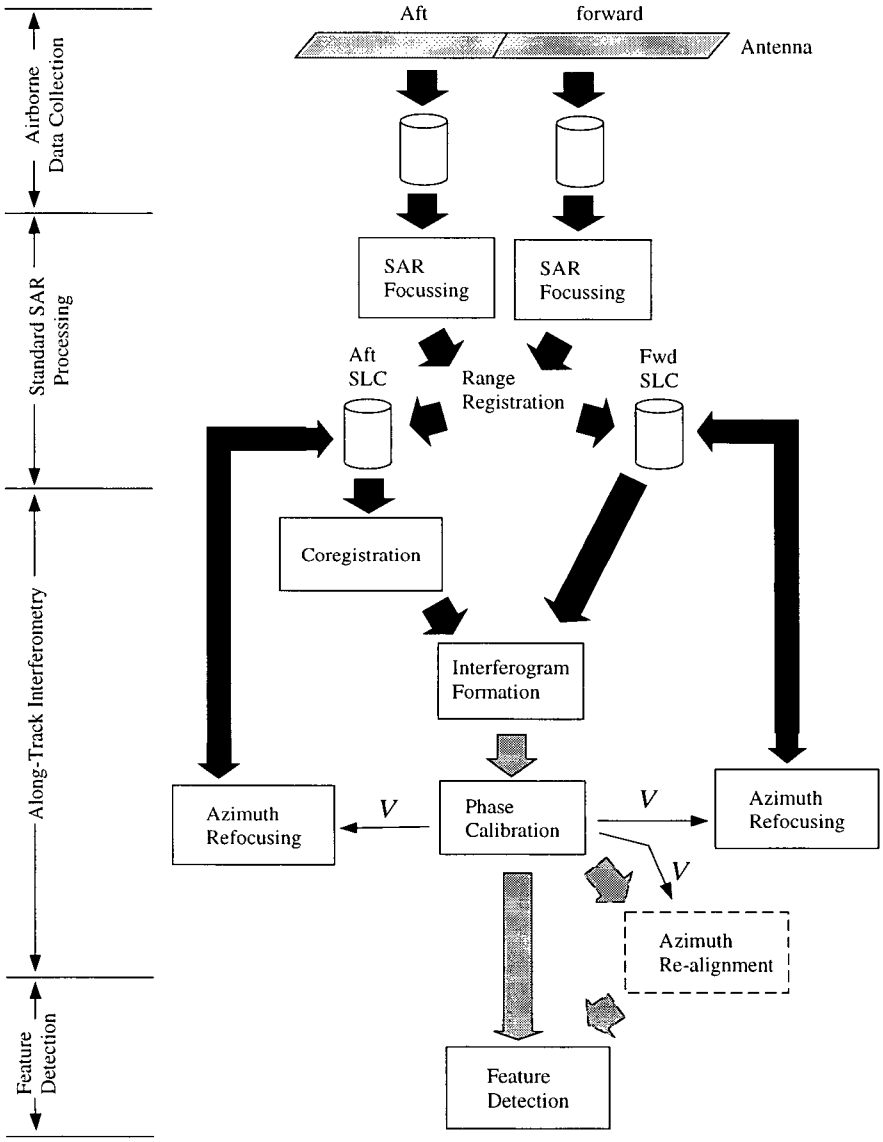

Figure 2.3 SAR ATI Processing Stages

2.3 Feature Detection

Once the raw radar data is transformed, through the basic ATI processes illustrated above, into an interferogram containing usable Backscatter and motion information, features and targets may be detected and extracted. Although there is sufficient Backscatter bearing magnitude and motion bearing phase information in the raw complex interferogram to distinguish large or bright features, without further operations, the interferogram appears noisy and cluttered and fine details are not easily distinguishable.

Operations in this subsequent phase of processing to reduce noise and clutter, which we will call Feature Detection, include: *Multilooking*, *Filtering*, and finally *Target Detection*. Multilooking and filtering will be examined in Chapter 3 and target detection will be examined in Chapter 4 and 6.

2.4 Detection Metrics

In order to examine the effect of various processing stages on the detectability characteristics of features in ATI images, we required a set of metrics to quantify then compare and contrast key features in data and images before and after various processing stages and in the final form interferogram images.

The characteristics that are of most interest to us in this work are those that relate to detection, which we define here as the observation of sufficient characteristics of a feature to identify it as being or belonging to an expected target. We chose *Contrast* and Image *Target to Background Ratio (TBR)* , an analogue of Signal to Noise Ratio (SNR), because these are the two basic criteria by which two common numeric detectors, the general non-adaptive Maximum-Likelihood detector and a common adaptive CFAR / Neyman-Pearson detector, select detection thresholds. Contrast and TBR are discussed below in detail. A more extended discussion of basic numeric detection theory and its application to ship wake features in ATI images is included as Appendix B.

We note that, although we confine our primary observations to quantitative (numeric) results, we also include visual presentations of features in the discussions of subsequent chapters to qualitatively support quantitative observations and conclusions. It should also be noted that we also considered pattern, linearity, and persistence as important detection criteria. However, like visual detectability which is not easily quantifiable, we have avoided their treatment in this current work. Possible future work, however, could include an assessment of pattern and linearity detection and their inclusion in a generalized SAR ATI ship wake detector.

2.4.1 Contrast

Contrast is defined here as the relative level of a feature's characteristic signal above its background. In this research, the characteristic signal is either interferometric magnitude, which is related to radar Backscatter, or interferometric phase, which is related to velocity. In this study we define and use a non-dimensional *Contrast Index*, CI, which is a weighted sum of normalized general and local background differences, defined according to Weber's law [8]. It is expressed as follows:

$$CI = 0.7\left(\frac{|\mu_{feature} - \mu_{vicinity}|}{\mu_{vicinity}}\right) + 0.3\left(\frac{|\mu_{feature} - \mu_{scene}|}{\mu_{scene}}\right) \quad (2.12)$$

where μ is the ensemble average of signal levels in a region and *vicinity* is defined as the region immediately adjacent to the feature of interest and *scene* is defined as the ensemble average of the regions in the image not containing any features of interest.

Magnitude or Backscatter Contrast: Contrast in conventional SAR images and the magnitude component of interferogram images is the relative radar brightness of a target above the mean brightness of its surroundings. The term brightness is appropriate to describing radar Backscatter because its analogy to visual luminance is quite close and standard SAR images tend to look very photograph-like.

Brightness in Backscatter or magnitude images of the ocean is a function of several factors, primarily the presence and number of Bragg resonant scatterers on the surface, the incidence angle of the radar beam, the local tilt angle of the surface, and velocity bunching. Ocean features are primarily imaged through Bragg resonant scattering and, to a lesser degree, by velocity bunching. On the ocean surface, the primary Bragg scatterers are very short scale wind-generated capillary waves, whose presence and strength is determined primarily by wind speed. Features are generally imaged by their modulation or damping of these waves. The Backscatter contrast of a feature is directly influenced by the density of Bragg scatterers and their modulated strength. Incidence angle directly influences the general brightness of the ocean background. Low incidence angles, particularly in spaceborne SAR images, result in specular reflection and bright ocean background, making it difficult to distinguish small features. Higher incidence angles, generally the case in airborne SAR images, result in more diffuse reflection and relatively dark ocean background, making it easier to detect smaller features. However, at low incidence angles, there is less return from all surface roughness, reducing the visibility of features (such as turbulent wakes and internal waves) which are imaged predominantly by the damping effect of Bragg scatters. Likewise, the local incidence angle or tilt angle of the surface influences radar brightness. However, unlike incidence angle, which determines the general brightness and range of brightness of the entire scene, the local brightness features and regions in a scene may vary significantly from the mean brightness of the scene because of their tilt angle. Two regions having equal density and strength of Bragg scatterers and imaged at the same general incidence angle may have differing rightness depending if their tilt angles are different. This is more applicable to very long waves travelling in the range direction. Backscatter contrast then is a function of wind speed and incidence angle of the sensor as well as its modulation of Bragg scatterers and its tilt angle.

Phase or Velocity (Motion) Contrast: In SAR ATI, interferometric phase is a measure of the surface radial velocity of scatterers and the Doppler spectrum in the scene (this will be shown in more detail in Chapter 4). Phase contrast is therefore the spatial differential velocity (i.e. differential motion over space) and the spatial difference of Doppler frequencies in the scene.

Unlike radar Backscatter, the velocity of a feature is less dependent on the incidence angle of the sensor or on the local tilt angle of the feature or its background than surface current or wind speed. Differential velocity, and therefore phase contrast, is only loosely dependent on wind speed and Bragg scatterers. It is loosely dependent on wind and Bragg scattering in the sense that the wind may impart a general velocity to the ocean background which will be detected by phase and in that because ATI is still a form of radar, it still needs a minimum amount of Bragg scattering in order to 'see' the scatterers that make up the visible surface, however the density of Bragg scatterers does not influence the phase contrast.

2.4.2 Target to Background Ratio

We define image Target to Background ratio as the feature excess over the background normalized by the local Standard Deviation. This is a statistical quantity has been used by Tough and Ward [9] to model the discrimination of interferometric phase signals from areas of two homogeneous surfaces with different power spectra. We express image TBR as follows:

$$TBR = \frac{|\mu_{feature} - \mu_{vicinity}|}{\sigma_{feature} + \sigma_{vicinity}} \tag{2.13}$$

where $\mu_{feature}$ and $\mu_{vicinity}$ are the mean signal level of the feature and the background and σ_{feature} and σ_{vicinity} are the standard deviation of feature and local background. The background distribution, σ_{vicinity}, is measured in small regions of relatively consistent signal levels taken in the vicinity of the target feature(s); with each region chosen to avoid any features or significant anomalies.

It should be noted that we use the term TBR in the detection sense, where our target is a region in an image containing an expected feature and the noise is the noise in the background of the image. Although Tough & Ward term this 'the analogue of signal to noise' [9], we stress that our use of TBR in this research should not be confused with classic receiver sense of SNR, in which the signal is the returning radar pulse and the noise is thermal noise in the receiver or antenna system.

Chapter 3 Interferogram Processing Analysis

In this chapter and Chapter 4, we examine the effect and effectiveness of the various processes involved in the formation of ATI interferograms from focused SLC image pairs on the visual quality and quantitative detectability of ships, wakes and other features in the scene. In this chapter, we examine coregistration, azimuth refocusing and pre-detection filtering in detail (and phase calibration and multilooking in brief) by analyzing various characteristics of the processed images, including frequency distribution and coherence. The effect of the mixing operation will be discussed in Chapter 4 where we examine the raw signal information in the SLC image pairs and the Backscatter and motion signal information after interferogram formation.

3.1 The CCRS C-band SAR ATI Data Set

The CCRS C-band SAR ATI sensor is a special configuration of the experimental CCRS airborne C/X-band SAR operating aboard a Convair CV580 twin engined turbopropeller aircraft. The radar is sidelooking with two antenna systems. The *Main* (transmit) antenna is mounted on a 3 axis joint inside a pod under the empennage (aft section) of the aircraft and the *InSAR* (Interferometric SAR) receive antenna is mounted on a similar 3 axis joint inside a pod on the starboard (right) side of the empennage. The InSAR receive antenna is strip-type and measures approximately 1m in length. In the ATI mode, it is split to provide 0.46m displaced forward and aft phase centres.

The radar can be operated in one of three geometries, or modes: *Nadir Mode* in which the radar views a narrow swath from 0^0 to 74^0 off nadir (i.e. out to approx. 22km at an altitude of 21,000 ft.) in high resolution (6m in range x 6m in azimuth), *Narrow Swath Mode* in which it views a narrow swath from 45^0 to 76^0 off nadir in high resolution, and *Wide Swath Mode* in which the radar views a maximum coverage wide swath from 45^0 to 85^0 off nadir in low resolution (20m in range x 10m in azimuth). In the ATI configuration, the radar is normally operated in Nadir Mode. The published operating characteristics of the CCRS C-band ATI are summarized below as Table 3.1 [10]:

Table 3.1 Operating specifications of the CCRS Convair 580 C-band SAR ATI

Operating frequency	5.3 GHz (C-band) λ=0.0566 m
Peak Power	64 kW, 16 kW, 1.2 kW
Polarization	H transmit, H receive

Table 3.1 Operating specifications of the CCRS Convair 580 C-band SAR ATI

PRF	2.32 or 2.57 Hz/m/s
(estimated) Noise-Equivalent Backscatter	-40dB
Sensitivity-Time Control (attenuator)	38dB
Azimuth Beam Width (-3dB)	3.03^0
Elevation Beam Width (-3dB)	28.0^0
Antenna Gain (one-way)	26.0dB
I,Q sampling frequency	37.5 MHz
I,Q bandwidth	26.3 MHz

Its performance specifications, from published calibration tests, are summarized below as Table 3.2 [11] [12]:

Table 3.2 Performance specifications of the CCRS Convair 580 C-band SAR ATI

Along-track pulse separation	0.0195 m
Along-track antenna separation	0.46 m
Azimuth (processed) BandWidth	4 degrees (0.0698 radians)
Range bandwidth	27 MHz
Radial velocity sensitivity	24 degrees per m/s (0.4189 rad per m/s)
Unambiguous radial velocity range	+/- 7.5 m/s per +/–π radians (15 m/s per 2π radians)
Unambiguous azimuth angular range	8.3 degrees (0.1449 rad)
Reported radial velocity error	2-10 cm/s

Three CCRS C-band ATI data sets or scenes were used in the work of this study. These scenes were collected by CCRS in June and August 1995 during a CCRS West Coast data acquisition campaign and the DND MARCOT 95 series of military trials. They are described below as Table 3.3 and a visual catalogue of the three scenes and detailed descriptions of their format are included in Appendix C.:

Table 3.3 Sample C-band ATI Data Sets (Scenes) used in Analysis

Name	Catalog #	Description	Size
Scene A	June 23 Line 4 Pass 2	Continental Shelf off coast of Nova Scotia	5968 (Az) x 2048 (Rng) pixels 24 km (Az) x 8 km (Rng)

Table 3.3 Sample C-band ATI Data Sets (Scenes) used in Analysis

Scene B	June 23 Line 8 Pass 3	Continental Shelf off coast of Nova Scotia	2894 (Az) x 2048 (Rng) pixel 12 km (Az) x 8 km (Rng)
Scene C	August 21 Line 16 Pass 7	Active Pass & Strait of Georgia off coast of BC	2804 (Az) x 2048 (Rng) pixels 11 km (Az) x 8.2 km (Rng)

For convenience, these scenes will herein after be referred to as Scenes A, B, and C. To facilitate the detailed analysis of ship features in this study, representative ship features were extracted from the three scenes as five smaller chip scenes. These chip scenes are listed below in Table 3.4 with a description of their principle features, the parent scene from which they were extracted, and their size:

Table 3.4 Description of Chip Scenes

Chip #	Parent Scene	Description of Features	Size (pixels) rnge x az
Chip #1	Scene A: June 23, Line 4, Pass 2	1x frigate sized ship w/ DTW and 2x Kelvin arms.	512 x 1024
Chip #2	Scene A: June 23, Line 4, Pass 2	1x wake arm of an unidentified small vessel (vessel is not visible).	256 x 512
Chip #3	Scene C: Aug 21, Line 16, Pass 7	3x pax ferries each w/ DTW, 2x Kelvin arms, and stern wake.	1024 x 1024
Chip #4	Scene B: June 23, Line 8, Pass 3	1x large bright land feature and current shadow.	1024 x 512
Chip #5	Scene B: June 23, Line 8, Pass 3	3x small slow moving ships with little or no apparent wakes	256 x 1024
Chip #6	Scene C: Aug 21, Line 16, Pass 7	1x very long linear wake	256 x 512
Chip #7	Scene C: Aug 21, Line 16, Pass 7	3x small fast moving ships with prominent linear wakes trailing	256 x 512
Chip #8	Scene C: Aug 21, Line 16, Pass 7	Edge of bright land feature and tidal current.	1024 x 256

Table 3.4 Description of Chip Scenes

Chip #	Parent Scene	Description of Features	Size (pixels) rnge x az
Chip A	Scene A: June 23, Line 4, Pass 2	2x frigate sized ships w/ associated turbulent and Kelvin wakes	1034 x 1024

The location of each chip in their respective parent scenes are shown as dashed boxes in Figure 3.1, Figure 3.2, and Figure 3.3 of Appendix C.

3.2 SLC Image Quality

We can verify the proper basic processing or SAR focusing of the SLC image pair by examining the azimuth spectrum of a chip of the forward SLC image of Scene A. The spectrum of the forward SLC image, extracted by taking 512 point FFTs in the azimuth direction, detecting the spectrum, and averaging over 20 range cells (i.e. the representative azimuth spectrum of a representative group of range cells), is shown below as Figure 3.1:

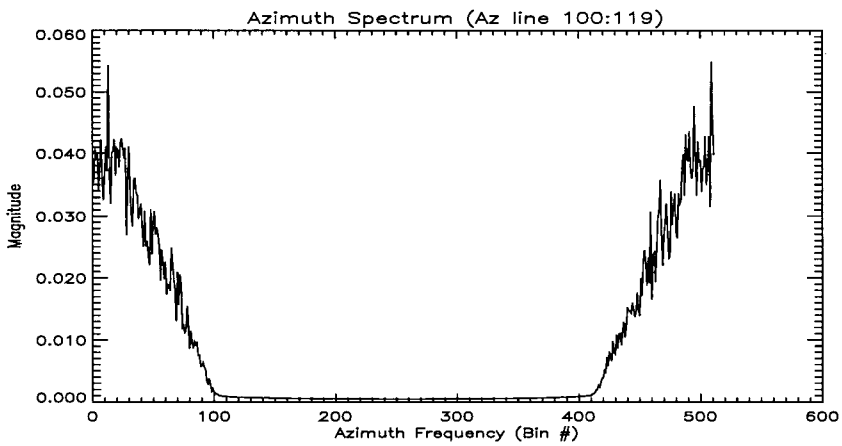

Figure 3.1 Azimuth spectrum of 20 range cells

We can see from this figure that the information content of the signal is confined to within the first 2/5 of the azimuth spectrum. This is because the PRF of the radar is approximately 2.5 times the Doppler bandwidth generated by the 1 m transmit antenna, and only 3 degrees of the azimuth beamwidth was processed by the azimuth matched filter. This corresponds to about 184 Hz of processed bandwidth at 100 m/s, when the PRF is 464 Hz. It can be seen that the azimuth signal energy extends to about 180 Hz,

agreeing with the processed bandwidth. We note that the data has been processed to zero Doppler, as expected.

3.3 Correlation, Phase Noise and Coherence Magnitude

We noted in equation (2.10) of Section 2.2 that the principal information of interest in ATI interferograms is the motion bearing spatial domain phase. Ideally in interferograms produced from highly correlated SLC image pairs the only phase present is information resulting from the motion of targets in the scene. By *Correlated*[1] we mean that the phase in the two images (the forward and aft SLC image pair) have a high degree of similarity. However, in practice, phase noise from various sources results in significant decorrelation, or loss of similarity, which results in loss of target discrimination and velocity estimation accuracy in the interferogram. Sources of phase noise include:

1. *spatial misregistration* in the SLC image pair;
2. receiver noise; and
3. random scatterer motion in the scene.

In order to maximize the accuracy of the estimation of velocity from phase in the interferogram, it is important remove from the SLC image pair as many sources of phase noise as possible. We will examine the different processing steps and operations that are employed to remove and reduce phase decorrelation in SLC images prior to mixing and in the final raw interferogram.

3.3.1 Coherence Magnitude

In order to quantify the effects and effectiveness of an operation, in this case an ATI processing stage, to remove or reduce decorrelating phase noise, we need a simple measure of correlation. We chose *Coherence*, a measure of correlation or the similarity between time separated images, as this metric. Coherence, γ, is defined as the normalized cross-correlation of two signals or images, x and y. It is a measure of the correlation or similarity between the images. We can express this in equation form as:

$$\gamma = \frac{E\{xy^*\}}{\sqrt{E\{|x|^2\}E\{|y|^2\}}} \tag{3.1}$$

[1] We note that this is image to image correlation as opposed to pulse to pulse correlation which is of concern in SAR focusing.

where x and y are complex values, and * denotes the complex conjugate.

In practice, coherence is estimated by taking a sample average over the image pair, x and y, which we express as:

$$\gamma \approx \frac{\sum xy^*}{\sqrt{\sum |x^2| \sum |y^2|}} \tag{3.2}$$

where the domain of the summation is over a small area or *Window* of the image. By passing a moving window across the SLC image pair, calculating their coherence, and assigning the estimated coherence value to the central pixel in the averaging window, we can create a 2-dimensional *Coherence Map*. Essentially, this is an averaged interferogram of the SLC images, with the phase of this 'interferogram' being the averaged differential phase of the two SLC images and the magnitude, $|\gamma|$, being the *Coherence Magnitude* (CM). For our purposes, we consider CM a sufficient measure of complex correlation[2] and a good indication of the quality of interferometric processing. The range of valid CM values is between 0 and 1, with 1 representing perfect coherence and 0 representing no coherence between the pixels of the image pair. The maximum achievable CM in practice is never 1 because residual phase noise (usually from the receiver) is present in all practical systems and results in a maximum CM that is slightly lower than 1.

In calculating CM, it is important that an appropriate window size be used in producing coherence maps and calculating CM. The choice of window size is a compromise between statistical smoothness of the estimate and estimate bias caused by spatial diversity of differential phase (i.e. radial velocity). For statistical smoothness, 10 - 40 samples are usually averaged, and to minimize the effects of spatial diversity, the averaging window is selected to be roughly square in ground coordinates. We select an averaging window size of 1 x 19 pixels is selected such that the window size in ground range coordinates is sufficiently large and square (4 x 4.1 m), so that we can assume the radial velocity of the scattering surfaces is reasonably constant within this area. In this case, the larger-scale spatial diversity of the surface velocity field should not bias the local CM estimate.

---

[2] CM is affected more by how well the phase matches between the images, as opposed to how well the magnitude matches. Thus, CM is a measure of how well matched the phase pattern is between points from image to image regardless of the phase change from pixel to pixel. If the phase from pixel to pixel in a SLC image is random, but matches well with the phase of the second SLC image, then the CM will be high. In this way, CM is a measure of the local standard deviation of differential phase.

CM can also be used as a measure of the signal to noise ratio (SNR) of the image, as phase noise in a SLC image is directly related to SNR. The relation between SNR and CM is expressed as:

$$SNR = \frac{|\Upsilon|}{1-|\Upsilon|} \tag{3.3}$$

It should be noted that CM is not a linear measure of phase noise and that phase noise produces a larger variation of CM in pixels with low CM values than it does with higher CM values. Additionally, pixels with lower intensity levels will typically have lower mean CM values due to the fact that their relatively higher component of receiver noise leads to higher phase noise.

3.3.2 Inherent Correlation

In Section 2.2 we noted that the forward and aft SLC images are nearly identical except for the motion of the target between closest approaches of the two antennas. If the baseline separation were small (which is true of the 0.5m baseline of the CCRS C-band ATI) and the platform were moving fast (which is roughly true of the 126m/s ground speed of the CV-580 aircraft), then the *Inherent Correlation* or correlation prior to any interferometric processing, should be quite high.

We can verify that this is the case in the CCRS C-band ATI data set by examining the inherent correlation of a representative scene. Additionally, we can use the inherent correlation to:

- validate the assumption that misregistration in ATI SLC images involves only linear translation,
- establish a lower bound of coherence in the ATI SLC image pair, and
- validate the statistical consistency of the CM estimation technique.

To accomplish this, we first produced a coherence map, calculated from a 400 pixel by 400 pixel region in the centre of the unregistered SLC image pair of Scene A. Its calculated distribution is plotted in Figure 3.2 below:

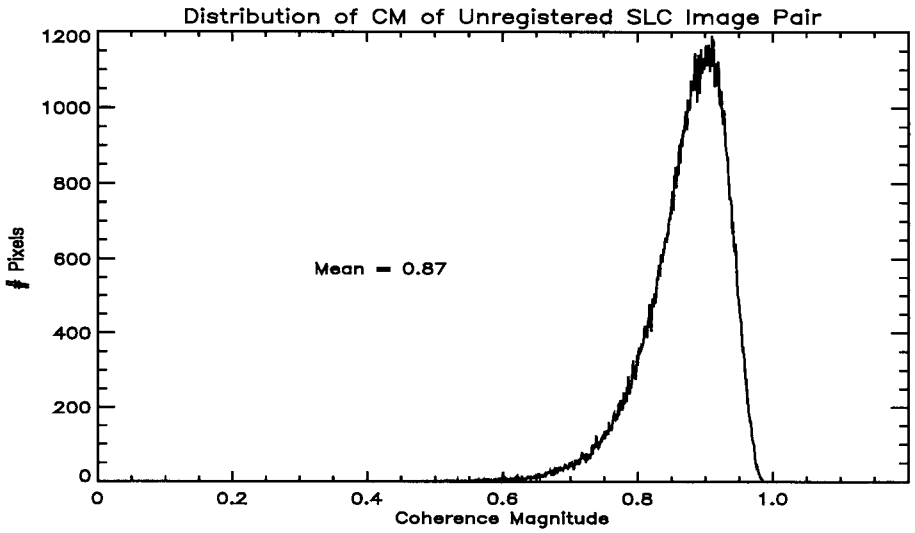

Figure 3.2 Distribution of CM values of unregistered image pair.

We can see from this distribution that the scene has an average inherent CM value of 0.87 and a most probable inherent CM value of around 0.90. This relatively high CM was not unexpected since the misregistration (0.5 m) is small compared with the processed resolution (about 1 m). Assuming that misregistration is equal everywhere, the high CM values indicates a high degree of inherent coherence in the scene; establishing a lower bound of coherence for any subsequent coregistration operation. Receiver noise and random scatterer motion, however, will still cause some loss of coherence after the misregistration is corrected.

Next we calculated the CM variation over azimuth and range and examined the variation and distribution. The CM variation over azimuth was calculated from a coherence map of a 200 pixel by 56344 pixel range band in the middle of the scene. The CM variation over range was calculated from a coherence map of a 1250 pixel by 200 pixel azimuth band in the middle of the scene. These are shown below as Figure 3.3.

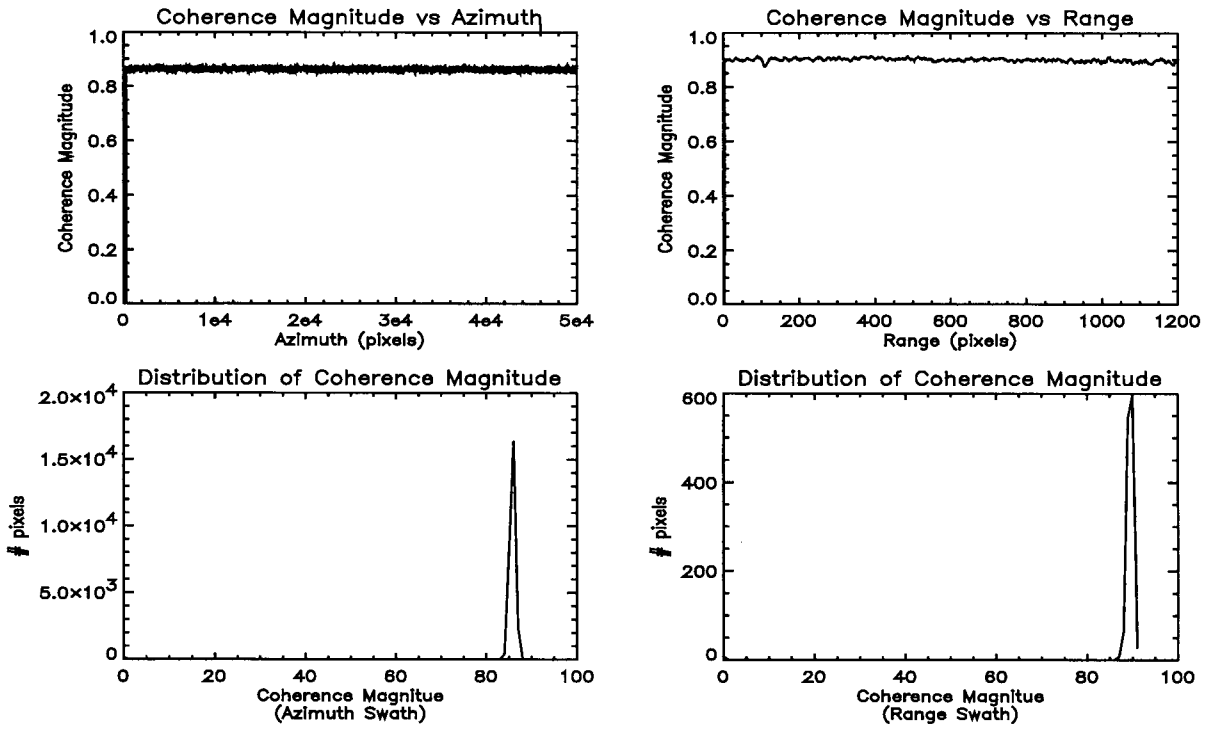

Figure 3.3 Variation of CM over azimuth and range

We can see from this figure that the variation of CM from pixel to pixel in both azimuth and range was quite small, on the average of between +/- 0.015, indicating that there is little statistical variation between samples. This shows that the averaging window used, 21 pixels in azimuth by 4 pixels in range, to estimate CM is large enough to give acceptable statistical smoothness.

We can also see that the CM variation over the azimuth strip was negligible. This would appear to validate the assumption that decorrelation due to misregistration arises from linear translation only (i.e. a constant spatial shift in azimuth and/or range) with little or no effect from any stretching or rotation. If there were a scale change or a rotation between the two SLC images, we would expect that the CM would exhibit a variation over azimuth. This is what would be expected from the geometry of the small baseline along-track separation.

It is also noted that the CM value dropped by approximately 0.01 from near to far range. This small drop in CM is caused by a drop in SNR over range. The fact that the change in CM is so small is an indication that the SNR is sufficiently high that receiver noise is not having a great effect on coherence.

3.4 Coregistration

The largest source of decorrelating phase noise in ATI images is spatial misregistration in the SLC image pair. We showed in equation (2.10) of Section 2.2 that this decorrelation was of the form of a frequency domain phase offset and that it was due to the physical displacement of the two antenna phase centres. It can be seen from this equation that the misregistration can be removed by a coregistration operation, which can be implemented either as a resampling in the spatial domain or a phase multiply in the frequency domain.

In operation, coregistration of two images requires:

1. an estimation of the amount and direction of the spatial misregistration; and
2. a correction for the misregistration by removing the spatial shift in one of the images.

Techniques for determining the direction and amount of misregistration include:

1. estimation from the known physical geometry of the sensor. In the case of airborne ATI, the spatial shift is often assumed to be an azimuth shift equal to one half the distance between antenna phase centres; or
2. determination by an iterative search in which successive (rule based) shifts are applied until a specific metric is maximized. Rules and metrics commonly used in general coregistration include: point target or feature matching, maximization of local CM[3](with and without fringe frequency compensation), minimization of phase residues, and maximization of the contrast of fringe lines.

Spatial misregistration between image pairs is generally corrected in two steps: a correction for integer size shifts and a correction for sub-pixel size shifts. Integer sized pixel shifts are quite easily corrected by simply changing the index of pixels in one of the two images. Sub-pixel shift correction is more involved and is generally accomplished by some form of resampling or interpolation. For simplicity, the term, 'shift' is often used generally to mean the more complicated sub-pixel shift portion of the operation and is often used interchangeably to mean interpolation. Some common sub-pixel shift methods include:

1. time (spatial) domain resampling using a spline fitted interpolator;

---

[3] Although CM is essentially the result of a correlation operation, most CM maximization methods do not use the CM itself as a measure of the amount of corrective shifting required, but rather it is used as an indicator of when the correct shift has been found by iteration.

2. time (spatial) domain resampling using a sinc-fitted FIR interpolation filter[4];
3. oversample, integer shift, subsample; and
4. frequency domain phase multiply.

3.4.1 Misregistration estimation methods

We examined two misregistration estimation methods, a 1-D azimuth a priori determined shift and a 2-D exhaustive iterative search shift estimation. We use CM as a metric to compare the effectiveness of the two methods.

The 1-D a priori shift estimation is not actually an estimation method but rather an assumption; that the optimum misregistration can be determined a priori from the geometry of the ATI system. This assumption is based on a) the misregistration being constrained in the azimuth direction; and b) the misregistration being continuous throughout the data or scene. In the case of the CCRS C-band ATI, the misregistration is assumed to be one half the phase separation of the antenna or 0.23m. Given an azimuth resolution of 0.216m/pixel, this translates into a shift of 1.1 azimuth pixels. In the following analysis, the corrective azimuth shift was implemented as a time domain convolution with a 4-point cubic spline interpolation kernel. This is the method routinely employed by CCRS to coregister ATI SLC image pairs.

Exhaustive 2-D iterative search estimators are commonly employed in coregistration of Across-Track Interferometric (XTI) SLC image pairs, where the above two assumptions cannot be made. In these estimators, misregistration is determined by taking regular samples in the image pair and iteratively shifting samples in one image until a particular metric is either maximized or minimized. In this case we use CM as the metric operating on a window size of 50 x 50 pixels. Iterative estimate/shifting stops when CM is maximized locally and the CM variation is less than 1/10000. The corrective bulk (linear) azimuth shift is applied by a frequency domain phase multiply and any required corrective bulk range shift is applied by FIR filtering using a Hamming weighted sinc interpolation filter. The two resampling filters in the azimuth and range directions allow for variable shifts in range and azimuth as well as rotation; essentially giving 3 degrees of freedom. This assumes unimodal CM maximum as borne out in Figure 3.5

The SLC image pair of scene A was coregistered using a 1-D a priori determined shift with a 4-point cubic spline interpolation shift and coregistered using a 2-D iterative search (CM maximization)

[4] interpolation methods 1 and 2 can both be modeled as a time domain interpolation using a short length FIR filter; with either a spline fit or windowed sinc fit. In the present implementation, the spline interpolation is modeled as a numeric fit to a polynomial.

estimator developed for spaceborne XTI by Mike Seymour of the UBC Radar Remote Sensing Group. After forming a coherence map of a 128 x 128 pixel in the centre of the registered image pairs, the CM distribution of each was computed and compared with the (inherent) CM of the unregistered image pair. This is shown below as Figure 3.4. Only the significant CM value range from 0.8 to 1.0 is shown.

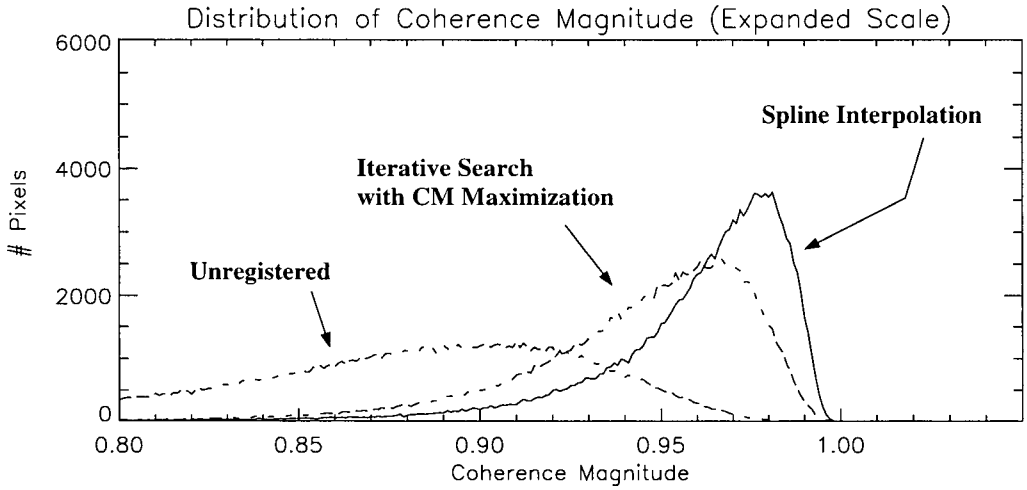

Figure 3.4 Relative CM performance of various coregistration techniques

From this figure, we can see that both estimation and shift methods improved CM considerably over the original unregistered image pair. However, it would appear that the 2-D iterative search using CM maximization method did not perform as well as the 1-D a priori determined shift. We suspect that this is because the 2-D estimation and subsequent 3 degrees of freedom resampling (shift) introduces more phase noise than the 1 degree of freedom (azimuth only) shift of the cubic spline interpolator; since all practical interpolators cannot produce exact shifts.

Thus it would appear then that 1-D a priori determined estimate of misregistration is sufficient for this type of data. Further, it would appear that limiting the shift operations to only one degree of freedom (azimuth translation only) minimizes the introduction of phase noise from imperfect interpolators.

3.4.2 Verify Optimal Azimuth Shift

We examine the correctness of the *a priori* determined shift estimate of 1.1 pixels by comparing it to the optimal azimuth shift which achieves maximum CM in the image pair. We determine this optimal

value by shifting the aft image in small shift increments until CM is maximized. Starting with the unregistered SLC image pair, the aft image was shifted in units of 0.1 pixels in azimuth, and the CM measured at each shift. Curves of CM versus shift were also computed for shifts in units of 0.02 pixels and 0.01 pixels in azimuth.

Azimuth pixel shifts were implemented by a frequency-domain interpolator, where a phase ramp in azimuth was used to shift the aft image the specified amount. A feature-less region of 128 x 2048 pixels in the centre of the Scene A was selected as the sample chip. As the interpolator, which implements a circular shift, has end effects, the CM was measured over a 128 x 1600 area in the middle of the chip. CM was calculated using a window of size 1 x 19, spaced at every 10th pixel to ensure a reasonable degree of statistical independence.

Figure 3.5 shows the plot of the CM versus pixel shift for shifts in units of 0.1, 0.02, and 0.01

pixels.

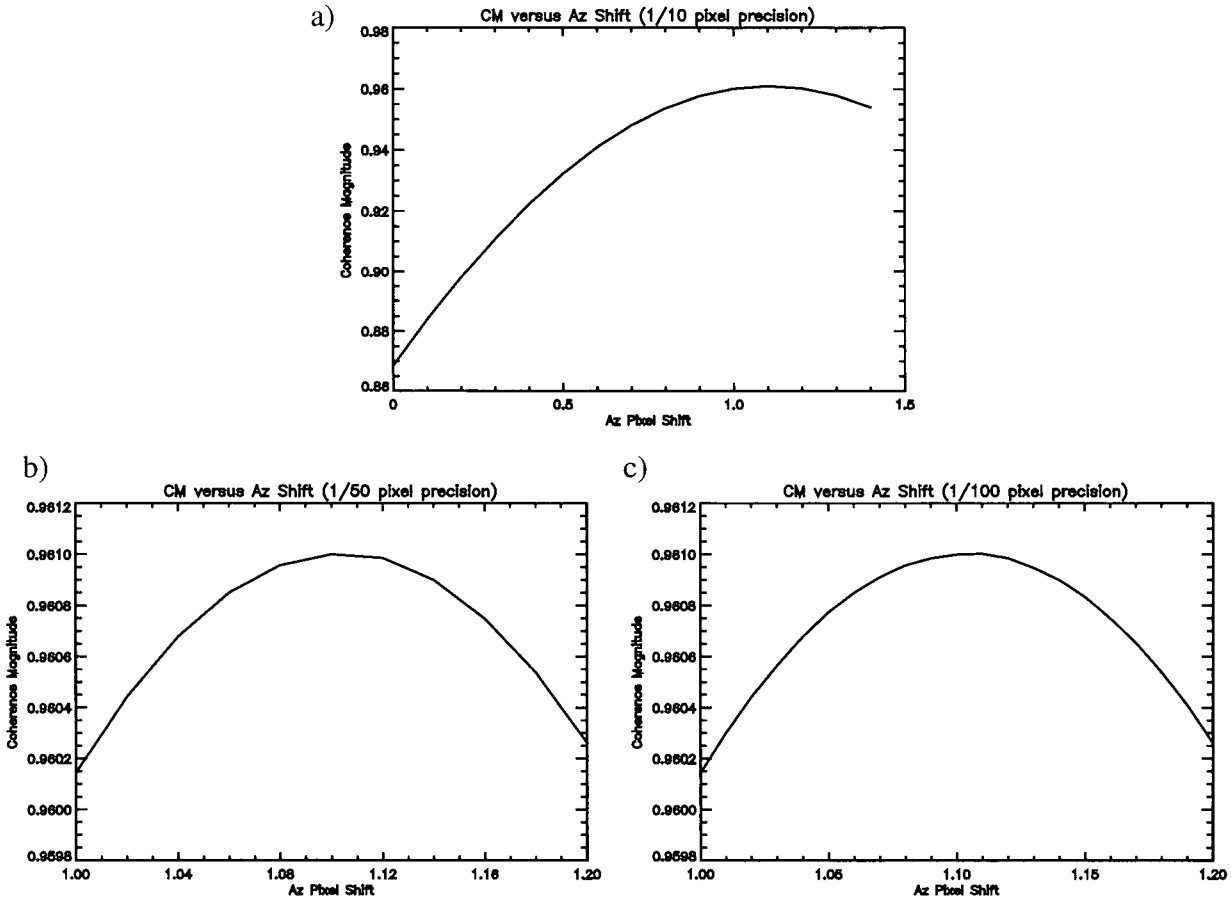

Figure 3.5 Coherence Magnitude of registration over various azimuth shift

Figure 3.5a shows the CM curve between 0.0 pixels and 1.5 pixels evaluated at shift intervals of 1/10 pixel. We can see from this curve that as expected, the best shift is 1.1 pixels. Beyond 1.1 pixel shifts, the CM gradually drops off. Figure 3.5b and 3.5c show the CM curve for the data re-evaluated between the shift intervals of 1.00 pixels and 1.20 pixels at shift intervals of 1/50 and 1/100 pixels respectively. Calculated CM values around the optimal shift at each precision level are summarized below as Table 3.5:

Table 3.5 CM vs. 1/50 and 1/100 Pixel Shifts

1/10 pixel precision		1/50 pixel precision		1/100 pixel precision	
Shift	CM	Shift	CM	Shift	CM
1.0	0.960144	1.08	0.960956	1.10	0.960999
1.1	0.960999	1.10	0.960999	1.11	0.961002

Table 3.5 CM vs. 1/50 and 1/100 Pixel Shifts

1/10 pixel precision		1/50 pixel precision		1/100 pixel precision	
Shift	CM	Shift	CM	Shift	CM
1.2	0.960261	1.12	0.960985	1.12	0.960985

It would appear from Table 3.5 above, that the optimum azimuth pixel shift, to a precision of 1/100 of a pixel, is actually 1.11 pixels. The maximum error in CM resulting from restricting shifts to 1/50 of a pixel is at most 0.00015 (calculated between 1.11 and 1.13 and between 1.10 and 1.12) and at most 0.00074 from restricting shifts to 1/10 of a pixel (calculated between 1.1 and 1.2 and between 1.11 and 1.21 pixels). In this data, the improvement in CM between a pixel shift of 1.1 and 1.11 is only 0.000003. It would appear then that a precision of 1/10 of a pixel is sufficient for corrective azimuth shifts in this data.

3.4.3 Verify Accuracy of Cubic Spline Interpolator

For practical coregistration processes, spatial domain interpolators are preferred over frequency domain techniques because of their computational simplicity; and Spline Interpolators[5] (implemented as either a 4-point or 6-point interpolation kernal) is considered a good choice for ATI. However, short length filters, such as the Cubic Spline Interpolator, introduce some phase distortion which can result in decorrelation and loss of accuracy of resulting interferometric products. The filter coefficients vary with intersample spacing so the filters have magnitude and phase responses which are different for different intersample spacing values. Although it is desireable to have different magnitude values for non-uniform spacing, the phase must be preserved over shifts of all spacings, otherwise the phase coherence in the final interferogram is distorted and the motion estimate may be lost. Additionally, interpolation introduces aliasing terms which result in phase errors and a reduction in coherence [14].

We examine the phase distortion, which we use to represent the accuracy, of a typical Cubic Spline Interpolation filter by comparing the phase response of a signal shifted by a Cubic Spline with a

---

[5] [13] A Cubic Spline Interpolation is a sub-pixel fit to a third order polynomial, which has the property of being smooth in the first derivative and continuous in the second derivative. The interpolated value, y, for the point, x, between integer pixels x_j and x_{j+1} is estimated by the following second order differential equation: $y = Ay_j + By_{j+1} + Cy''_j + Dy''_{j+1}$ where $A = \frac{x_{j+1} - x}{x_{j+1} - x_j}$ and $B = 1 + A$ are the coefficients of the linear case of a general Lagrange interpolation formula and $C = \frac{1}{6}(A^3 - A)(x_{j+1} - x_j)^3$ and $D = \frac{1}{6}(B^3 - B)(x_{j+1} - x_j)^2$

benchmark; the same signal shifted by a frequency domain phase multiply. For this analysis, we used a simulated signal generated by adding together a real and imaginary ramp (i.e. a complex signal, of length 32768 samples, with increasing magnitude and constant phase) and actual data consisting of an azimuth line of 32768 range cells extracted from the middle of the first 1/3 of the range swath of the forward SLC data of Scene A. The azimuth line was chosen so as not to contain any significant bright features and only those pixels well in from the ends of the array were examined in order to avoid the effects of circular convolution.

A plot of the time domain and frequency domain phase distortion of the Cubic Spline interpolator for shifts between 0 and 1.2 pixels is shown as Figure 3.6 below.

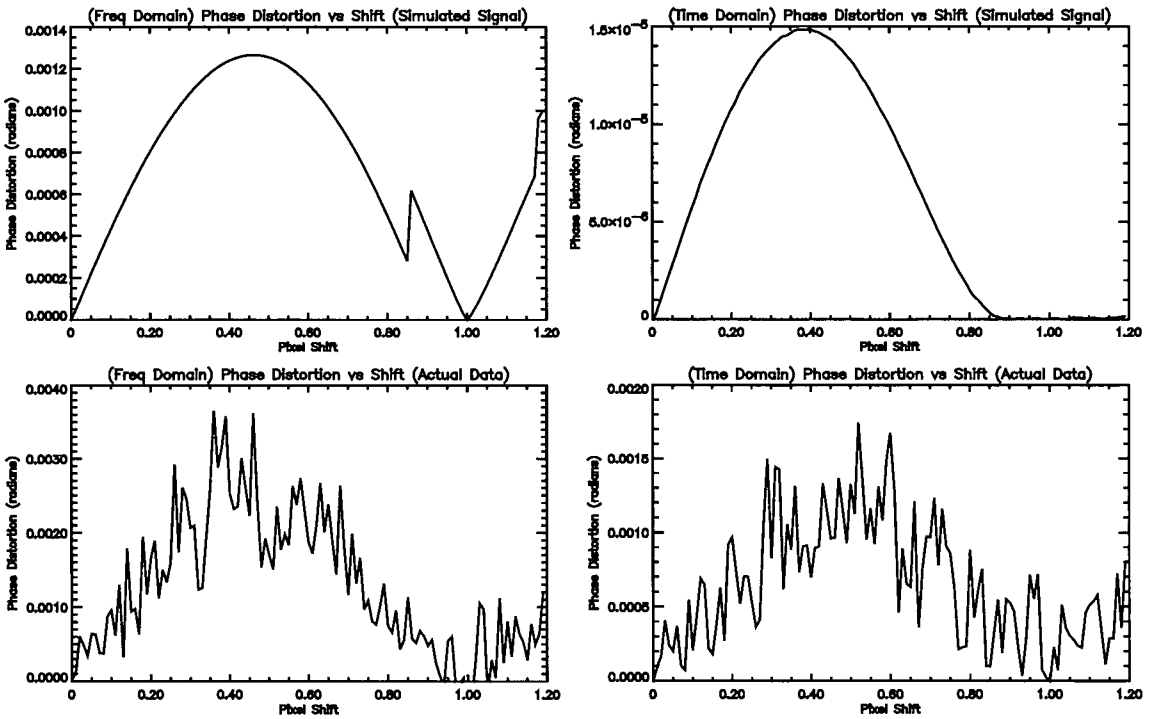

Figure 3.6 Phase distortion of Cubic Spline Interpolator

We can see from this plot that the Cubic Spline interpolator is essentially non-phase distorting, with a maximum phase distortion of less than 0.004 radians over the range of all fractional pixel shifts.

3.5 Phase Calibration

After Coregistration, the two registered SLC images are mixed (i.e. conjugate multiplication). The

resulting complex interferogram, contains both velocity information, represented as a phase, and Backscatter information, represented as a magnitude (which is actually the intensity of the Backscatter of the two SLC images). In practice the phase in the interferogram also contains a DC phase offset. This DC phase is unknown a priori, but can be removed by calibration. This can be accomplished by estimating the phase of some feature in the scene which has a known velocity of zero (i.e. such as piece of land) and multiplying the phase image with a compensating linear function. In scenes where there is no such zero velocity feature, the absolute velocity cannot be determined from the phase information in the image. This is the case in many of the representative ATI images, taken by the experimental CCRS C-band sensor, used in our study.

3.6 Multi-Looking

After mixing, images often need to be multi-looked before the image is usable or any targets may be detected. This is because the proportion of speckle noise to target pixels is quite large at the output resolution of the SAR and ATI processors. Multi-looking reduces speckle noise and the resolution of the image. One further benefit of multilooking is that it reduces the resolution of the longer azimuth dimension to match that of the range dimension (i.e. a square aspect ratio) to produce a correctly proportioned (1:1 aspect ratio) image. For real images, this is often accomplished by simple averaging of range lines over a window of the length of the number of looks, where the window is usually Gaussian shaped; essentially a Gaussian weighted decimation filter. In the case of the complex interferograms used in this study, multilooking was accomplished by a more precise azimuth subsampling of the real and imaginary channels using Hanning weighted FIR decimation filters. Each interferogram was averaged 19 times in azimuth to give a final resolution of 4m/pixel to match the 4m/pixel range resolution.

Multi-looking is considered to be well understood technique in general SAR and SAR interferometry and will not be treated in any further detail in this report.

3.7 Azimuth Defocusing Correction

Decorrelation can arise from random scatter motion in the scene [15]. This can be exhibited in two effects on conventional SAR and SAR ATI images. Firstly, any azimuth motion in the scene will cause defocusing during SAR processing, because the SAR processor assumes a single focusing velocity figure [16]. And secondly, if the rate of scatterer motion, called *scene decorrelation time* (or *ocean coherence time* in the case of an ocean scene), is sufficiently great with respect to the speed of the sensor and the

displacement between antennas, the two images of the same scene will not be phase coherent over the time interval and the interferogram will be meaningless.

In general, azimuth defocusing is more of a problem in Backscatter images than in phase (velocity) images. We will examine this in greater detail below.

Scene decorrelation between acquisition times of the spatially displace antennas, however, is potentially a more serious problem for ATI. In the following analysis of azimuth defocusing, we will assume, for the moment, that scene decorrelation is not a problem for the CCRS C-band ATI; which has a relatively short baseline separation of 0.5 m and a relatively high platform velocity of 126 m/s, viewing typical ocean scenes with decorrelation times on the order of 0.05 to 0.1 seconds. This will examine and verify this assumption in further detail in Chapter 5.

3.7.1 Azimuth Refocusing

For optimal focusing of stationary targets, the matched filter employed in the SAR processor is set to the sensor platform's along-track velocity, termed the focus setting of the SAR. When the SAR processor attempts to focus a random or rapidly moving scene (i.e. containing high spatial frequencies with respect to the averaging window) using a single (global) fixed non-optimal focus setting, the resulting image will be defocused. The effects of azimuth defocusing can be seen as a shift in the position and a spread of the energy distribution of pixels containing moving scatterers. Blurring due to shifts in target position is from Line of Sight (LOS) or slant range motion and blurring due to pure defocusing is from azimuthal motion only. Both effects result in a general smearing or blurring of pixels in azimuth.

Azimuth defocusing can be corrected by refocusing the image using a matched filter with a new focus setting that takes into account the relative azimuthal motion of the scatters [17]. By passing defocused targets through the corrective matched filter, the target's energy distribution, which was smeared over several azimuth pixels, is recompressed into the narrow spatial profile that is characteristic of a properly focussed still target. For ATI, this is an extremely computationally intensive process as it involves refocusing both forward and aft SLC images priori to ATI processing. Additionally, if the synthetic aperture time is long, the targets' motion may not be linear and the refocusing may not work well. The success of refocusing is improved if the scene or target motion is constant.

3.7.2 Azimuth Re-alignment

A promising alternative to computationally intensive azimuth refocusing is *Azimuth Re-alignment*, a technique currently employed by CCRS to enhance their C-band airborne ATI images. Azimuth re-alignment reduces the azimuth smearing in defocused interferograms by correcting for the azimuthal shift of pixels elements due to their radial motion. This is accomplished by calculating the corrective shift from the interferogram, which is of the form:

$$\Delta_{Az} = \frac{u \cdot r}{V} = \Phi\left(\frac{r\lambda}{2\pi B}\right) \tag{3.4}$$

where u is the scatterer's radial velocity estimate, r is slant range to target, and V is the sensor platform's velocity, and applying a corrective resampling. In the case of the CCRS azimuth re-alignment technique, corrective resampling is accomplished with a Gaussian windowed interpolation filter. The sum of all the re-aligned (Gaussian fitted) pixels results in what is effectively a redistribution of shifted scatterers back into a narrower azimuth space.

We note that azimuth re-alignment only corrects for the positional shift of scatterers due to radial motion and does not explicitly address the smearing effect from pure azimuth motion. However, its effectiveness in visually enhancing defocused interferograms appears to be quite useful.

3.7.3 Visual, Spectral and Detection Effects of Azimuth Defocusing

We can examine the effect of azimuth defocusing by comparing the visual presentation, spectral qualities and detectability of features in *original* (i.e. images which show evidence of defocusing, prior to any correction) ATI images and the same image after a corrective azimuth re-alignment operation. For this analysis we used Chip #1 of Scene A, which contains a frigate sized ship and three prominent wake features: a DTW and two Kelvin Arms.

Visual Effects: The visual presentation of the original image and azimuth re-aligned phase image is shown below as Figure 3.7.

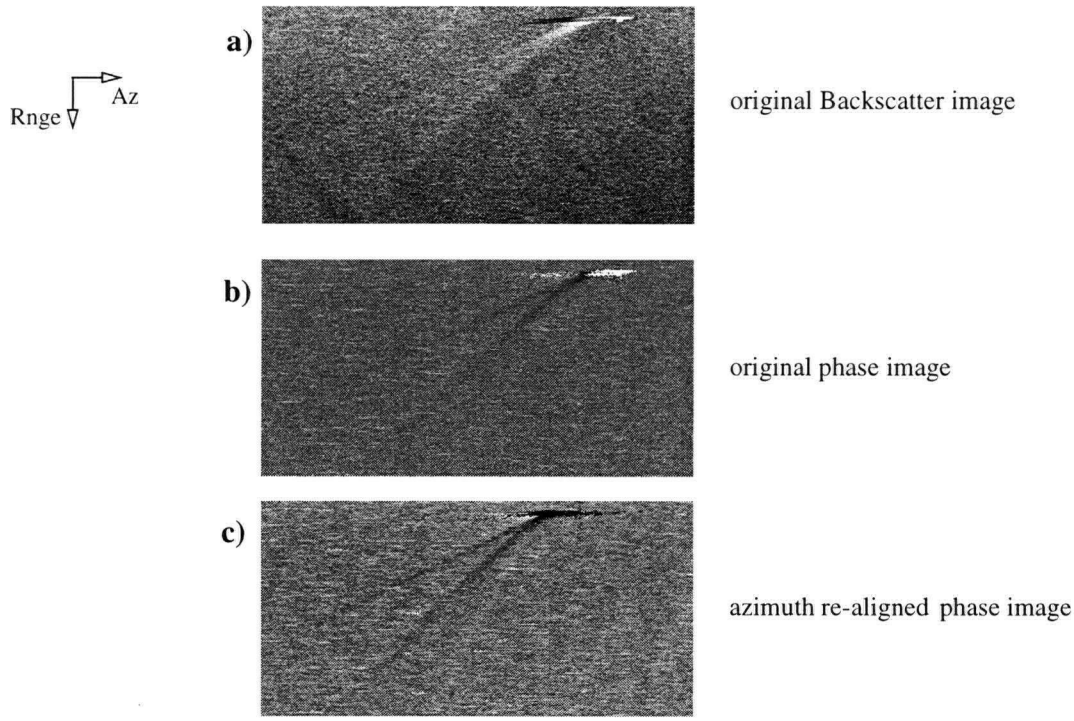

Figure 3.7 Original (defocused, unre-aligned) and azimuth re-aligned images of Chip #1 of Scene A

Visually comparing the images, the effect of azimuth defocusing on the presentation of ship wake features in ATI interferograms can be observed as an elongation in the azimuth direction of resolution cells, a general smearing or blurring of features in the azimuth direction, which appears to be worse in the Backscatter image where the distinction between different wake features is blurred out, and lower contrast, which appears to be worse in the Backscatter image.

The corrective re-alignment operation appears to improve the presentation of ship wake features in ATI interferograms by narrowing smeared features, particularly the DTW and Kelvin arms of the wake, and improve the visual contrast. This can be seen in the bright Kelvin arm (the lower arm) which was difficult to distinguish in the original image, but is quite visible in the re-aligned image. Residual defocusing effects, in the form of pixel elongation, are still quite evident in the phase image of Figure 3.7b) even after azimuth re-alignment.

Spectral Effects: The computed azimuth and range spectra (magnitude) of the original, azimuth re-aligned, and forward SLC image of Chip #1 are shown below as Figure 3.8:

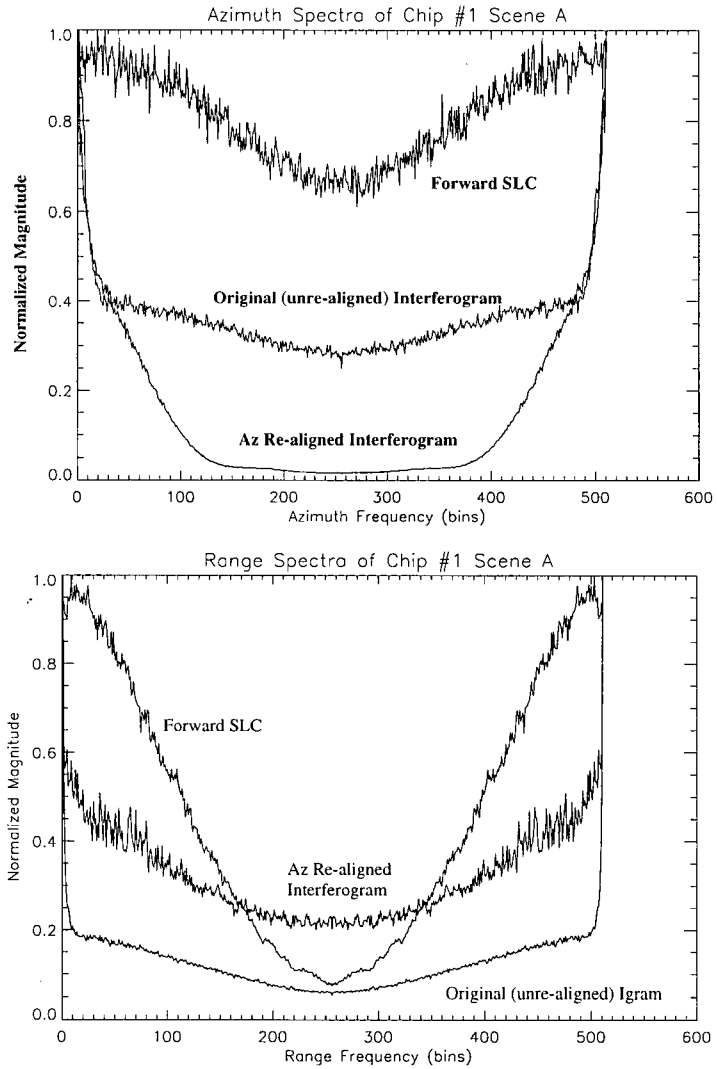

Figure 3.8 Azimuth and range spectra of forward SLC, original (unre-aligned) interferogram, azimuth re-aligned interferogram of Chip #1 of Scene A

We note that, as expected, the azimuth and range spectrum of the forward SLC image has a smooth bell shape that is indicative of the amplitude and phase pattern of the radar antenna. And that the azimuth spectrum of the original unre-aligned interferogram also has a smooth bell shape suggestive of the antenna pattern. However, the azimuth spectrum of the original interferogram contains relatively more lower frequency components than the forward SLC image. This is because the forward SLC image only contains target information in magnitude, while its phase is uniformly distributed and contains effectively no target information [18]. The phase of the original interferogram, on the other hand, is Gaussian distributed and does contain target information; as does the magnitude of the original interferogram.

Comparing the azimuth spectrum of the original interferogram with that of the azimuth re-aligned interferogram, we note that the original interferogram contains a significant amount of signal energy spread across all frequencies, whereas the signal energy of the re-aligned interferogram appears to be confined to within the first half of the spectrum, $0.5f_N$ where f_N is the Nyquist rate. Those components of the original interferogram which are in the higher frequencies would contribute to what may be perceived by a detector as noise. We observe then that the corrective re-alignment operation appears to have redistributed higher frequency components back into the information bearing lower frequencies. This would appear to have a similar effect to that of simple low pass filtering, which attenuates higher frequency components.

In range, the re-alignment operation appears to have added or increased the level of some higher frequency components. The cause of this effect is unexplained.

Detectability Effects: The computed detection metrics of the four features (the ship, DTW and 2 Kelvin arms) in the original image and the azimuth re-aligned phase image of Chip #1 of Scene A are listed in Table 3.6 below for comparison:

Table 3.6 Comparison of detection metrics of features in original (defocused, unre-aligned) and azimuth re-aligned phase images

	Original (defocused)			Azimuth Re-aligned		
feature	Contrast Index	TBR	Size ($1000m^2$)	Contrast Index	TBR	Size ($1000m^2$)
Ship	0.46	0.53	86	0.43	0.22	46
DTW	0.04	0.29	138	0.30	0.50	144
Brt Kelvin Arm	0.04	0.32	129	0.32	0.52	96
Dark Kelvin Arm	0.004	0.14	86	0.03	0.20	86

We see, in Table 3.6, that the azimuth re-alignment operation appears to have increased the contrast of wake features by a factor of between 7.5 and 10 and improved TBR by about 1.5dB to 2.5dB. Additionally, the apparent size of some features, such as the ship and the bright Kelvin wake, which have more extent in azimuth than in range, have been reduced. This would appear to agree with our visual observation, which was that wake features were more distinct after re-alignment. And our spectral observations, that higher frequency components, which may be confused with clutter, are redistributed into lower frequencies, where they were easier to distinguish from clutter. The exception to this general

improvement effect was the bright ship target, whose contrast and TBR appeared to have been reduced somewhat by the re-alignment operation.

3.8 Pre-Detection Filtering

The visual presentation and detectability of target features prior to feature detection can be improved by filtering the interferogram. Various types of filters can be employed, including adaptive filters, band-pass filters, non-linear spatial filters, spin filters, etc.... The most general and useful filtering, however, is simple Low Pass (LP) filtering to remove the higher frequency components in the interferogram that would otherwise be mistaken by a detector (or the human eye) as noise and clutter. We can see this by examining the range and azimuth spectra of a representative image chip, a sub-chip region within it containing no features, and a sub-chip region containing prominent targets, such as wake features. The spectra of Chip #3 of Scene C, which contains 3 passenger ferries and trailing DTW and Kelvin wake

features, is shown below as Figure 3.9.

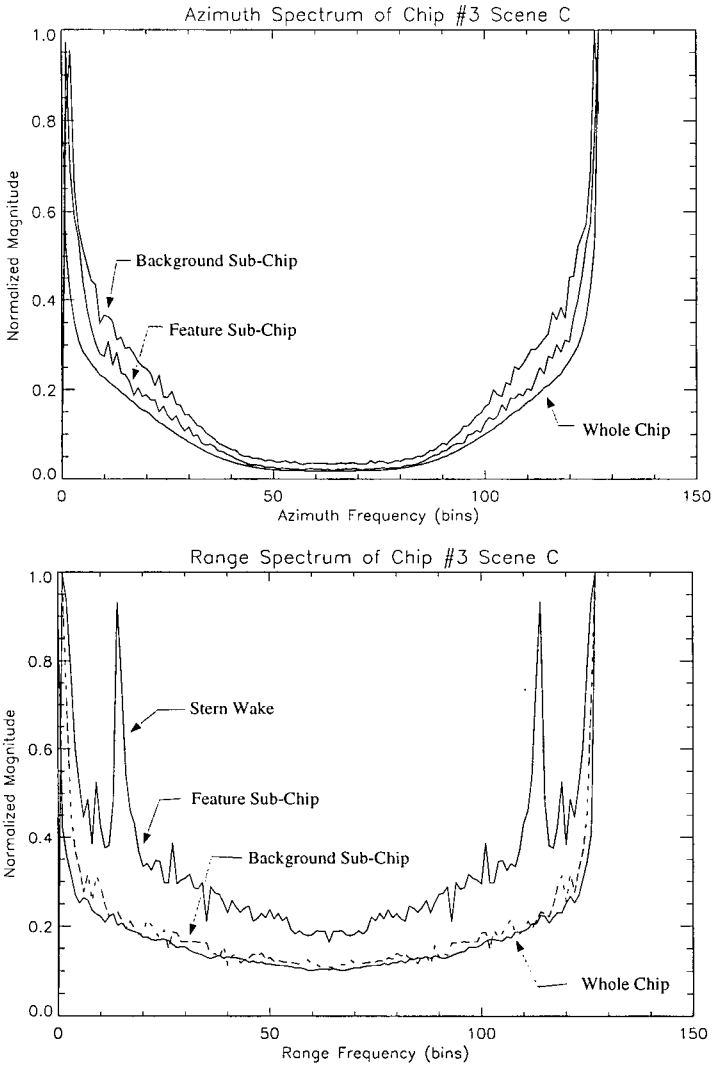

Figure 3.9 Azimuth and range spectra of Chip #3 and background and feature sub-chips

The azimuth spectrum of the larger chip image was computed by taking 1028 point FFTs of range lines of the complex interferogram chip and averaging the magnitude results of 1028 lines. The range spectrum was similarly computed by taking 1028 point FFTs of azimuth lines and averaging the magnitude results over 1028 lines. The smaller feature region and background region sub-chips were calculated using 512 point FFTs. The larger chip spectra were averaged to 512 points and overlaid on the plots of the spectra of the smaller sub-chips for comparison. We are comparing the spectrum of the feature region and background regions in an attempt to isolate the frequencies of the features from the background.

From the azimuth spectra we can see that the azimuth spectrum of the larger chip, the background sub-region and feature sub-region all appear to be similarly distributed over frequency, with 99% of the signal energy in all three regions contained within a band below $0.62f_N$, making the extraction of target components from just azimuth spectrum quite difficult. However, we note that the signal level in the feature region drops to 25% (the -6dB point) at about $0.25f_N$, which we choose as the cut-off frequency of an azimuth LP filter.

From the range spectra, we note that the spectrum of the larger chip region and the background region sub-chip are nearly identical. However, the range spectra of the feature region is quite different. The most prominent difference is the presence of a very large component centred around $0.25f_N$. This probably corresponds to periodic stern wakes in the feature region sub-chip. We also note that the signal level of the feature region spectrum drops to 50% (the -3dB point) and that of the background region drops to 25% (the -6dB point) at about $0.08f_N$, which we choose as the cut-off frequency of a range LP filter. We chose to ignore the stern ripple wake at $0.25f_N$ because we did not consider it to be as significant a wake signature as either the DTW or Kelvin arms. We note that stern wakes are rarely seen and these are likely only visible because they are range travelling and unaffected by azimuth defocusing. We also note that there is significant noise between $0.25f_N$ and $0.08f_N$ which would contribute to degrading detection.

3.8.1 Filter Implementation

The azimuth low pass filter was implemented as a 64 point Hanning weighted FIR filter with a cutoff frequency of $0.25f_N$ and ripple suppression of better than 50dB. The filter coefficients were

generated by IDL and the time and frequency response of the azimuth is shown below as Figure 3.10:

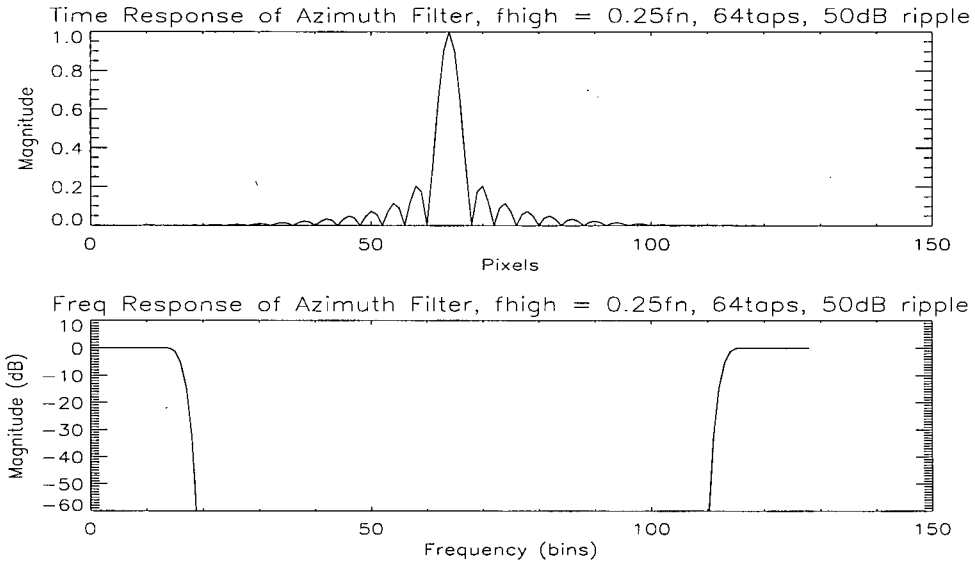

Figure 3.10 Azimuth filter response

The range low pass filter was implemented as a 16 point Hanning weighted FIR filter with a cutoff frequency of $0.08f_N$ and ripple suppression of better than 50dB. The filter coefficients were generated by IDL and the time and frequency response of the range filter is shown below as Figure 3.11:

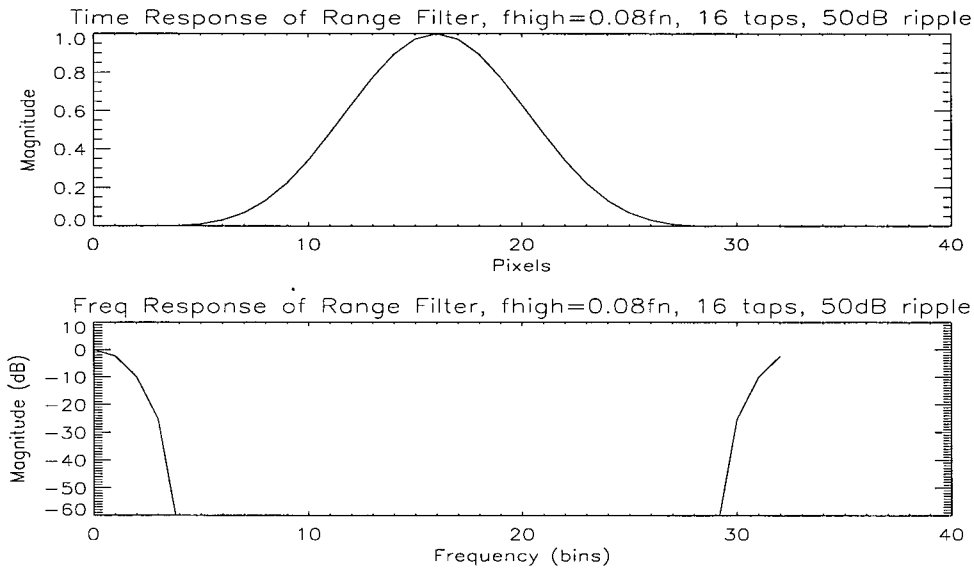

Figure 3.11 Range filter response

Filtering is applied to the complex data and 2-D low pass filtering is accomplished by applying the azimuth filter first, followed by the range filter. The size of each filter was chosen to be as large as possible, to achieve the best smoothing, but was limited to less than twice the size of the aspect of the desired feature in that dimension, in order to preserve as much fine detail as possible. I n range, we selected a 16 point filter and in azimuth we selected a 64 point filter. The azimuth filter is much longer than the range filter because features in azimuth are much more 'stretched' in azimuth because of defocusing than in range. With proper azimuth refocusing, the size of the azimuth filter can be reduced. We also note that our filter parameters were selected to enhance the detection of wake features and as a result may not be optimal for bright ship and bright land targets, whose Backscatter and phase signature may contain sidelobe artifacts, high signal levels and sharp transitions; all of which degrade the performance of low pass filters over these regions.

3.8.2 Filter Performance

We first examine the performance of the filters on a simple test signal. The complex test signal contained high and low signal level features and sharp and smooth transition in magnitude, with a constantly varying phase, which are typical of actual ocean scenes. The magnitude and phase of the test signal and magnitude and phase response of the azimuth and range filters is shown below as Figure 3.12

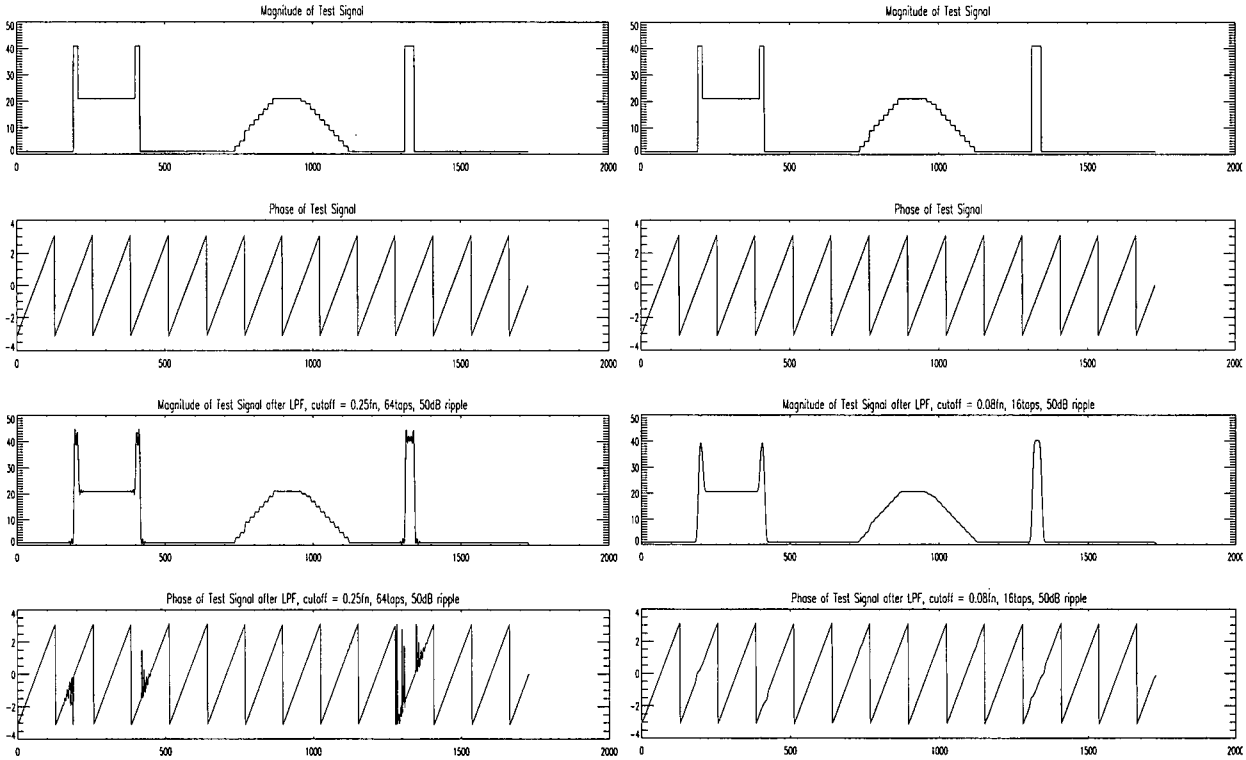

Figure 3.12 Azimuth and range filter performance on signals with sharp transitions and phase wraparound

We can see that the azimuth filter (and to a small extent, the range filter) contains a phase artifact at sharp transitions from and to very low signal levels. This is due to phase ambiguity at low signal levels and results in 'zebra' like patterns at the edge of transitions between bright land features (or ships) and very dark ocean in phase images. This is considered only a minor nuisance and no attempt was made to correct this in this study.

Visual Performance: We can evaluate the visual performance of the filters by visually comparing the unfiltered, azimuth filtered, range filtered, and 2-D azimuth/range filtered phase image of Chip #1 of Scene A, shown below as Figure 3.13.

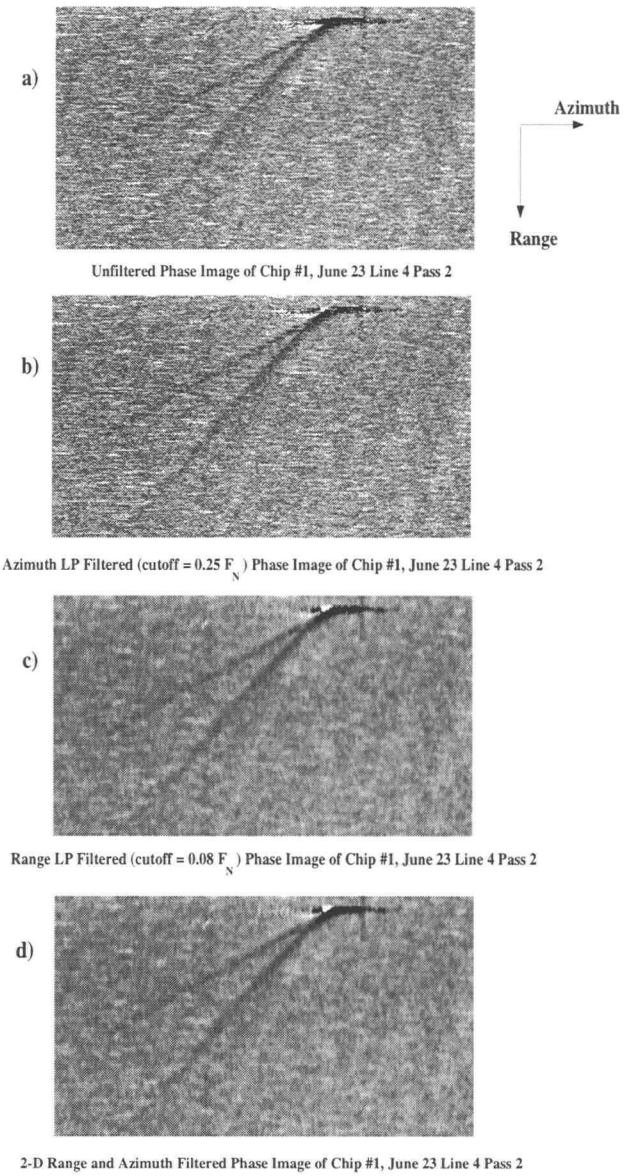

Figure 3.13 Unfiltered, azimuth LP filtered, range LP filtered and 2-D LP filtered phase images of Chip #1 Scene A

We can see that unfiltered image, Figure 3.13a), and azimuth filtered image, Figure 3.13b), are quite similar, indicating that the effect of the $0.25f_N$ azimuth filter is quite negligible. And in the range filtered image, Figure 3.13a), we can see that the background is quite a bit smoother and the ship and wake features are more distinct; indicating that range filtering is more effective than azimuth filtering in improving visual presentation. Comparing the range filtered image with the 2-D filtered image, Figure 3.13d), we observe that, although there is more smoothing in the 2-D filtered image, the visual presentation and the

distinction of features in the two images are quite similar; indicating that the incremental benefit of 2-D filtering over simple 1-D range filtering is small.

The unfiltered and 2-D filtered images of all other Chips of Scenes A, B, and C are shown in catalogue form at Appendix D for additional visual comparisons.

Detection Performance: We can evaluate the detection performance of the 1-D filters by comparing the detection metrics of the unfiltered, azimuth 1-D filtered, and range 1-D filtered phase images of Chip #1, which were measured and are listed below as Table 3.7 for comparison:

Table 3.7 Comparison of detection metrics of features in unfiltered, range filtered and azimuth phase image of Chip #1

	Unfiltered		Azimuth Filtered		Range Filtered	
feature	Contrast Index	TBR	Contrast Index	TBR	Contrast Index	TBR
Ship	0.43	0.22	1.51	0.93	0.90	1.18
DTW	0.30	0.50	0.33	0.58	0.27	0.88
Dark Kelvin Arm	0.32	0.52	0.32	0.58	0.29	0.89
Bright Kelvin Arm	0.13	0.09	0.02	0.21	0.02	0.45

From Table 3.7 we can see that filtering has negligible effect on contrast (the bright ship and bright Kelvin arm features being the exception) but dramatic effect on TBR; with TBR gains of between 0.5dB and 6dB from azimuth filtering and between 2dB and 7dB for range filtering.

And we can verify our visual observations that range filtering has greater incremental benefit on TBR than azimuth filtering.

We can evaluate the performance of 2-D low pass filtering by comparing the detection metrics of the unfiltered and 2-D filtered phase images of both Chip #1 of Scene A, and Chip #3 of Scene C, which

were measured and are listed below as Table 3.8:

Table 3.8 Comparison of detection metrics of features in unfiltered and filtered phase images

	Unfiltered			2-D Filtered		
feature	Contrast Index	TBR	Size ($1000m^2$)	Contrast Index	TBR	Size ($1000m^2$)
Chip #1 Ship	0.43	0.22	46	0.90	1.21	84
Chip #1 DTW	0.30	0.50	144	0.29	0.90	308
Chip #1 Dark Kelvin Arm	0.32	0.52	96	0.29	0.90	240
Chip #1 Bright Kelvin Arm	0.13	0.09	86	0.02	0.46	203
Chip #3 Ship	2.72	0.62	60	7.72	14.15	58
Chip #3 DTW	0.17	0.32	241	0.17	0.55	396
Chip #3 Kelvin Arm	0.11	0.35	36	0.06	0.60	211
Chip #3 Stern Wake	0.03	0.07	n/a	not visible	not visible	n/a

From Table 3.8 we can see that, as expected, there is negligible effect on contrast due to low pass filtering; the exception being very bright point target features, whose contrast are actually reduced by low pass filtering in some cases. The improvement in TBR due to low pass filtering, however, is quite evident in all features; with TBR gains of between 2.3dB and 13dB and the best TBR gains being observed in bright features such as ships and bright Kelvin arms.

Comparing these figures with those of Table 3.7, we can see that there is only a 0.05dB to 0.1dB (or less than less than 2.5%) difference between the TBR of the 2-D filtered images and 1-D range filtered image, indicating that range low pass filtering alone is responsible for over 97.5% of the total TBR gain due to filtering.

The apparent larger improvement in TBR due to range filtering over azimuth filtering may be explained by noting that the subject chip images had been multilooked / subsampled by 19 in azimuth in order to remove speckle noise and achieve a 1:1 aspect ratio (i.e. square pixels); multilooking being essentially an azimuth averaging or filtering operation. Additionally, we note that the azimuth re-alignment process, which we noted in 3.7 effectively behaves as a low pass filtering operation. In contrast,

the image was not subsampled in range and the range cells were essentially unaffected by azimuth defocusing or the azimuth re-alignment operation. This is quite significant in real-time ATI applications, where range line (azimuth) filtering could be eliminated to reduce overall computation. In the analysis of the remainder of this report, however, all images were 2-D LP filtered prior to detection for consistency.

Chapter 4 Signal Information Analysis

In Chapter 3 we examined the effect of the interferometric processing stages (other than mixing) on the visual, spectral and detection characteristic of features in the interferogram. This essentially examined how these processes modified and/or improved the coherence, frequency distribution, signal to noise ratio, and contrast and, thereby, the ultimate usability of the information content already present in the interferogram. In this chapter we examine the mixing operation, which forms the interferogram; essentially forming or creating the unique motion information from the raw coherent radar data. By examining the effect of this operation on the signal information content of the radar prior to and after interferometric processing, we can describe the form of the information presented by ATI (both motion and Backscatter) and determine the improvement to detection of ships and wakes from a signal information aspect.

In Section 2.2 of Chapter 2, we showed that the baseline separation between forward and aft antennas of the ATI configuration creates a time difference between images acquired by the two antennas, resulting in a time domain phase difference that bears the motion information in the scene, and that a conjugate multiplication, or mixing of the two SLC images after coregistration extracts this phase component. We can represent the mixing operation as an autocorrelation of the complex Backscatter field from each antenna as [19]:

$$R(\tau) = E[B(t)B^*(t-\tau)] \tag{4.1}$$

where B(t) is the complex Backscatter field (i.e. the radar return signal) received by one of the antennas and B(t-τ) is the complex Backscatter field received by the other antenna; with τ being the time lag resulting from the spatial separation between them and the resulting complex interferogram, $R(\tau)$, having a magnitude component, representing the correlated Backscatter of scatterers in the scene, and a phase component, representing the motion of scatterers in the scene.

4.1 Interferogram Magnitude

We can examine the effect of mixing on the Backscatter of the radar by representing corresponding pixels in an SLC image pair as closely correlated Gaussian random variables expressed as:

$$B(t) = I(t)e^{j(wt)} \quad \text{and} \quad \text{B(t-}\tau\text{)} = I(t-\tau)e^{j(w(t-\tau))} \tag{4.2}$$

where I(t) and I(t-τ) are the magnitude components and ωt and ω(t-τ) are the phase. Substituting these expressions into the autocorrelation relation as:

$$R(\tau) = E[I(t)I(t-\tau)e^{j\omega\tau}] \tag{4.3}$$

and taking the magnitude of the autocorrelation,

$$\begin{aligned} |R(\tau)| &= \left|E[(I(t)e^{jwt})(I(t-\tau)e^{-jwt}e^{jw\tau})]\right| \\ &= E[I(t)I(t-\tau)] \\ &\approx E[I(t)^2] \end{aligned} \tag{4.4}$$

we have an expression for the magnitude of the interferogram, which shows that the magnitude of the interferogram can be considered to be equivalent to the square of the Backscatter magnitude or intensity of a single antenna image, $\{I(t)\}^2$. This is true so long as the spatial correlation between the Backscatter fields from the two antennas is high; which is a reasonable assumption for an ocean scene; so long as τ is smaller than the coherence time of the scene. If τ is greater than the coherence time of the scene, the two signals received by the antenna have a reduced correlation and less information is obtained by interferometry [21].

Thus it can be seen that the magnitude image of an ATI interferogram is actually Backscatter intensity, which is essentially equivalent to the square of a conventional SAR image. However, we can show that Backscatter intensity from interferometric magnitude actually gives us an improvement in signal information quality over that which would be expected from the Backscatter magnitude of a conventional SAR image. This we can do by examining the noise rejecting property of the dual antenna configuration and mixing operation.

4.2 Backscatter Noise Rejection

Using equation (4.3), we can examine the Backscatter noise or magnitude error of the autocorrelation equation. Given multiplicative, N_i, and additive noise, n_i, components due to speckle and receiver noise in the two returned signals expressed as:

$$|x_1| = N_1 \cdot I(t) + n_1 \tag{4.5}$$

and

$$|x_2| = N_2 \cdot I(t-\tau) + n_2 \tag{4.6}$$

where N_1 and N_2 are correlated with a Rayleigh distribution and n_1 and n_2 are uncorrelated, zero mean and Gaussian, we can derive an expression for the mean and variance of the autocorrelation, x_1x_2, as:

$$|\overline{R(t)}| = E(|x_1x_2|) = E(N_1N_2I(t)I(t-\tau)) \tag{4.7}$$

and

$$var(|R(\tau)|) = E((N_1N_2I(t)I(t-\tau))^2) - E(N_1N_2I(t)I(t-\tau))^2 \tag{4.8}$$

We note that the variance of the magnitude of the autocorrelation can be approximated to:

$$var(|R(\tau)|) \approx var(|NI(t)|^2) = E(|NI(t)|^4) - E(|NI(t)|^2)^2 \tag{4.9}$$

which is essentially the variance of the faded with the uncorrelated additive noise rejected by the autocorrelation.

In contrast, the mean and variance of the square of a single image (ie. intensity) are:

$$|\overline{x_1^2}| = E(N_1^2I^2(t)) + E(n_1^2) \tag{4.10}$$

and

$$var(|x_1^2|) = E(N_1^4I^4(t)) + E(n_1^4) - E(N_1^2I^2(t))^2 - 2 \cdot E(n_1^2)E(N_1^2I^2(t)) - E(n_1^2)^2 \tag{4.11}$$

We note that in this case both the multiplicative (speckle) and additive (receiver) noise terms are completely correlated and the expression cannot be reduced. The resulting variance expression:

$$var(|x_1^2|) = var(|NI(t)|^2) + var(n_1^2) - 2 \cdot E(n_1^2)E(N_1^2 I^2(t)) - E(n_1^2)^2 \quad (4.12)$$

can be seen as the sum of the variance of the faded image and additive noise minus the product of the mean of the two. We note that the term $var(n_1^2) - 2 \cdot E(n_1^2)E(N_1^2 I^2(t)) - E(n_1^2)^2$ is non-zero and suspect that it is quite small.

Comparing equations (4.9) and (4.12), we can see that the ATI configuration and the mixing operation results in essentially a filtering or rejection of uncorrelated noise (i.e. speckle) and that the representation of the Backscatter of a scene by SAR ATI should be somewhat improved over the representation of the Backscatter of a scene by conventional single antenna SAR. We can also verify this by visual observation, analysis of the distribution of the Backscatter signal, and analysis of the detection statistics.

4.2.1 Visual Comparison

The single antenna (fwd) magnitude and intensity and ATI magnitude images of a chip of Scene A is shown below as Figure 4.1a) and c):

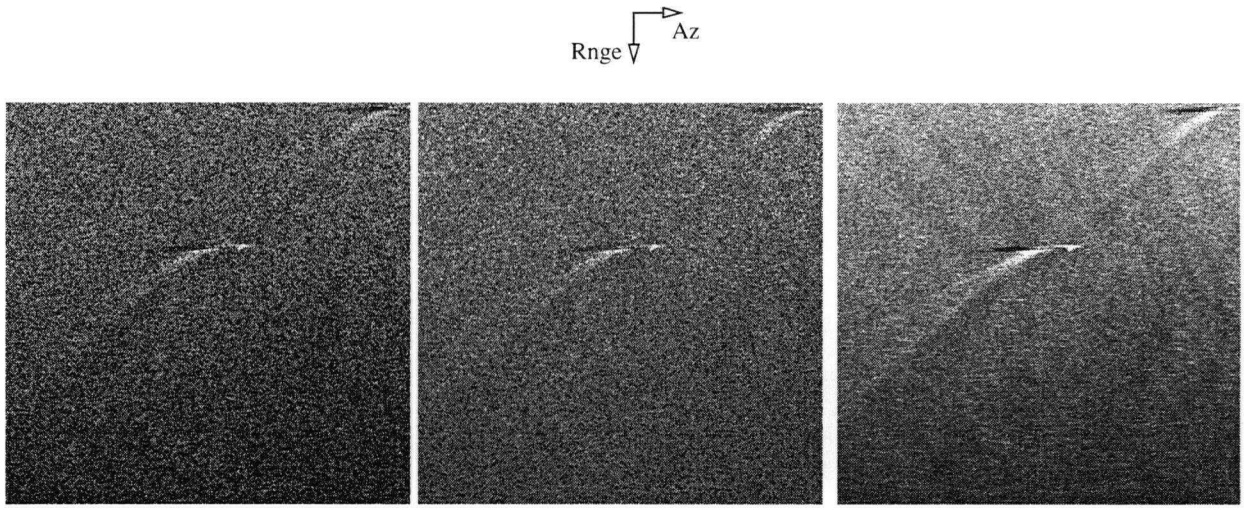

a) Backscatter Magnitude Forward Antenna

b) (Backscatter Magnitude)^2 Forward Antenna

c) Backscatter Intensity Dual antennas

Figure 4.1 Backscatter images acquired by single and dual antennas - Chip A of Scene A

The chip scene here has dimensions of 1024 pixels x 1024 pixels in range and azimuth with a

nominal resolution of 4m x 4m per pixel. The main features in the scene are two frigate-sized ship (travelling towards the upper right corner of the image) and their wakes (actually a DTW and 2 Kelvin arms each). Range is oriented in the vertical direction and azimuth is in the horizontal direction; with near range towards the top and azimuth increasing towards the right. Each image has been mapped into a 256 level grey scale for display. Figure 4.1a) is the Backscatter magnitude image acquired by a single (forward) antenna, Figure 4.1b) is the square of the single antenna image and Figure 4.1 c) is the interferogram magnitude image.

From visual inspection, the dual antenna Backscatter intensity (interferogram magnitude) image, Figure 4.1c), appears to have better detail definition and less speckle than the single antenna Backscatter image, Figure 4.1a) and b).

4.2.2 Backscatter Distribution

The distribution of the Backscatter information in the single antenna image and dual antenna interferogram are plotted together in Figure 4.2 below (the two graphs have the same units):

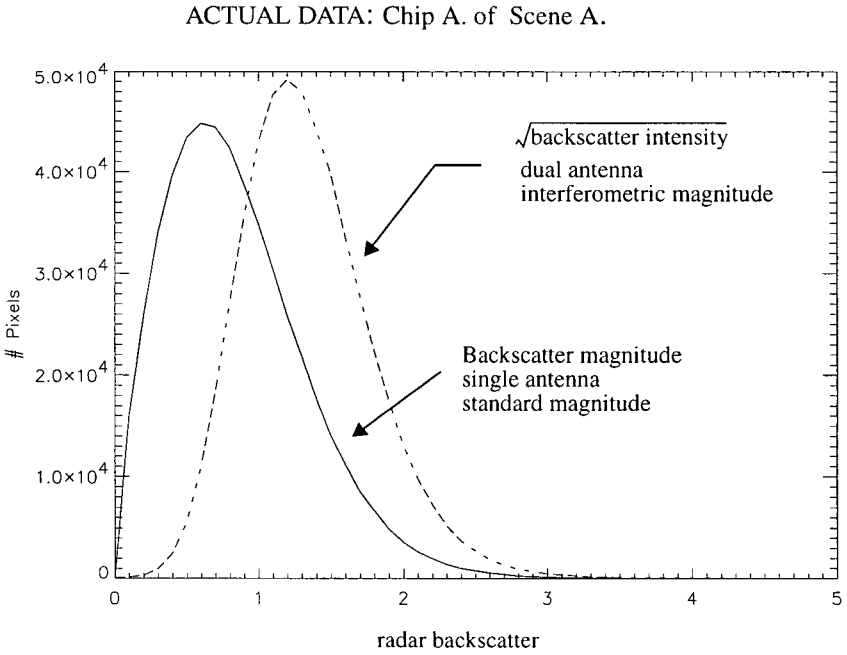

Figure 4.2 Comparison of distribution of radar Backscatter signals from single antenna standard and dual antenna interferometric magnitude images of Chip A of Scene A

From this figure, we can see that the standard magnitude and interferometric magnitude distribu-

tions are K-distributed, as we would expect[1]. However, the distribution of the single antenna standard magnitude appears to be more Rayleigh[2], because its distribution is highly non-symmetric and its peak is shifted towards lower values, while the distribution of the dual antenna interferometric magnitude appears more Ricean, because its distribution is more symmetric and its peak value is shifted towards higher values of radar Backscatter (i.e. it becomes more Gaussian).

Models of the signal information behaviour of complex radar signals show that the pdf of complex product magnitudes (i.e. interferometric magnitude or Backscatter intensity) are K-distributed, with the pdf of uncorrelated product magnitudes having a Rayleigh distribution as expected, and the pdf of correlated product magnitudes having more Ricean distributions with their peaks shifting towards the right with increasing correlation and becoming more Gaussian [25]. This would appear to indicate that feature information in the interferometric magnitude image dominates over speckle[3] and that the signal information in the interferogram is more correlated than that of the single antenna image.

4.2.3 Backscatter Signal Statistics

The Backscatter signal statistics of the central wake feature in the interferogram magnitude and

---

[1] It is a well known property of standard SAR images that the magnitude of the radar Backscatter from land scenes is Rayleigh distributed [20]. The Rayleigh Probability Distribution Function (pdf) models the specular scattering of distributed scatterers on a homogeneous surface and is often used to describe the Gaussian distributed reflected signal plus speckle property of single look Backscatter images of land scenes including speckle [18]. The Backscatter from an ocean scene, however, is often modeled as a K-distribution; which is better able describes the temporal and spatial correlation properties of a turbulent surface than a simple Rayleigh model.

[2] Analysis of real ocean data show that the best description of high resolution, high incidence angle ocean radar data is a compound model of the K-distribution, composed of a Rayleigh speckle model and a Gamma clutter model [22]. The Gamma clutter model arises from an assumption of the variable nature of the underlying cross section due to fluctuating number of (Bragg) scatterers per resolution cell [23]. In this model, the K-distribution tends to a Rayleigh density as the Backscatter becomes dominated by speckle noise [24].

[3] The Rice distribution is often used to represent narrowband stochastic signals, such as ocean clutter [26] and can be used to describe signal estimates in which a group of constant dominant scatterer dominates the Backscatter which contains a collection of Rayleigh scatterers [27]; in other words, indicative of a relatively clear and distinct (narrow-band) representation of features as opposed to a noisy and indistinct (wide-band) image.

single antenna Backscatter intensity image were measured and are tabulated below as Table 4.1:.

Table 4.1 Backscatter Signal Statistics of single and dual antenna images, Actual Data: Chip A of Scene A

	(Backscatter magnitude)2 - single antenna	**Backscatter intensity- dual antenna**
μ_{wake}	0.93	3.14
$\sigma_{feature}$	0.98	1.52
μ_{scene}	0.74	2.45
σ_{scene}	0.78	1.18
TBR	0.10 (-10dB)	0.26 (-6dB)

From this table, we can see that the wake feature in the interferometric magnitude (the second column) image has higher TBR over the same wake feature in the single antenna image (the first column),, the gain in detectability or noise rejection being about 4dB.

Thus we can see from error analysis, visual observation, analysis of the Backscatter signal distribution and signal statistics that the Backscatter intensity signal extracted from the interferometric magnitude of dual antenna configured ATI, is a somewhat better estimate of dominant scatterers or features in an ocean scene than the simple Backscatter magnitude signal from a single antenna standard SAR image. We can show that improved information signal quality is also the case for the phase of the interferogram.

4.3 Interferogram Phase

In Section 2.2 of Chapter 2 we showed that the phase of the interferogram was an estimate of the radial velocity of scatterers in the scene via the ATI equation:

$$u = \Delta\Phi\left(\frac{\lambda v}{2\pi B}\right) \tag{4.13}$$

where λ is the wavelength of the radar, v, the velocity of the sensor platform (aircraft), and B, the baseline separation between forward and aft antennas. We can also show that this is also an estimate of the Doppler signature of features in the scene.

4.3.1 Interferogram phase and Doppler frequency

The ATI equation is useful for discrete estimation of the radial velocity of individual surface scatterers in ATI phase images. However, individual resolution cells contain a number of scatterers which may have stochastically varying velocities, making the estimation of large and complex ocean structures, such as waves and ship wakes, from a distance difficult. An accurate and direct measure of motion is Doppler frequency; which describes the average motion of targets to the scale of the radar's resolution and the precision of it's wavelength. The following development by Thompson and Jensen [19] illustrate that the measured interferometric phase is directly related to the mean radial velocity of scatterers within a resolution cell; its Doppler frequency.

Given a power spectral density expression of the autocorrelation relation as:

$$R(\tau) = \frac{1}{(2\pi)^2}\int_{-\infty}^{\infty} e^{jw\tau}S(\omega) \tag{4.14}$$

$$\approx \frac{1}{(2\pi)^2}\int_{-\infty} (1 + j\omega\tau)S(\omega)d\omega$$

where $S(\omega)$ is Doppler spectrum. Noting that the (horizontal) surface velocity of ocean scatterers can be estimated from interferometric phase using the Bragg model relation [7]:

$$u = \frac{\Phi}{\tau K_B} = \frac{\arg\{R(\tau)\}}{\tau K_B} \tag{4.15}$$

where

$$K_B = 2k_0\sin(\theta_t) = \frac{2\pi}{\lambda}\sin(\theta_t) \tag{4.16}$$

is the Bragg wavenumber, k_0 is the radar wavenumber, λ is the radar wavelength, and θ_t is the radar incidence angle, and substituting the power spectral density into the argument of the autocorrelation:

$$\arg\{R(\tau)\} \approx \tau \cdot \frac{\int_{-\infty}^{\infty} \omega S(\omega) d\omega}{\int_{-\infty}^{\infty} S(\omega) d\omega} \approx \tau \cdot \bar{\omega} \tag{4.17}$$

and using equation (4.15), we can see that the surface velocity estimate from the power spectral density of the autocorrelation is:

$$u \approx \bar{\omega} \cdot \frac{\lambda}{2\pi \sin(\theta_t)} \tag{4.18}$$

which is a direct measure of $\bar{\omega}$ the mean Doppler frequency of the scatterer field. Given that all moving objects have a unique Doppler frequency, it can be seen that the ATI configuration is effectively a discrete Doppler frequency estimator or detector.

4.4 Phase Noise

In addition to making it possible to directly estimate the velocity of targets from the phase of the interferogram and the target's Doppler signature, the ATI configuration and mixing operation, also act as a simple time averaging filter which rejects phase noise. As in the case of Backscatter, we can do this by examining the phase of the autocorrelation expression, equation (4.3), with additive phase noise, n_a and n_b, expressed as:

$$\arg(R(\tau)) = w\tau + (n_a - n_b) \tag{4.19}$$

The phase signal (i.e. the information part) is:

$$\arg(R(\tau)) = \bar{\omega} t \tag{4.20}$$

which is a function of the mean of the Doppler frequency, ω. , and the phase error is:

$$\varepsilon_{\Phi 12} = [n_a - n_b] \tag{4.21}$$

n_a, n_b are uncorrelated zero mean Gaussian and are due to phase noise in the receivers. The mean and variance of the phase are then:

$$\overline{\arg(R(\tau))} = E(\omega\tau) \tag{4.22}$$

and

$$var(\arg(R(\tau))) = E((\omega\tau)^2) + E(\omega\tau)^2 + E(n_a^2) + E(n_b^2) \tag{4.23}$$

which is the sum of the variation in the phase information and the variance of the additive phase noise of the receivers. We note that the receivers contribute additive phase noise to the final interferometric phase; however, the phase is unaffected by the speckle fading.

We can see then that noise in the magnitude of the interferogram is dominated by speckle whereas the noise in the phase of the interferogram is dominated by receiver noise. If the system is working well and phase noise is reduced to as low as possible, we can see then that phase is inherently a less noisy parameter than magnitude.

We can verify this observation by further visual observations, analysis of Backscatter signal distribution, and analysis of the detection statistics.

4.4.1 Visual Observations

The Backscatter and motion images of Chip #3 of Scene C are shown below as Figure 4.3:

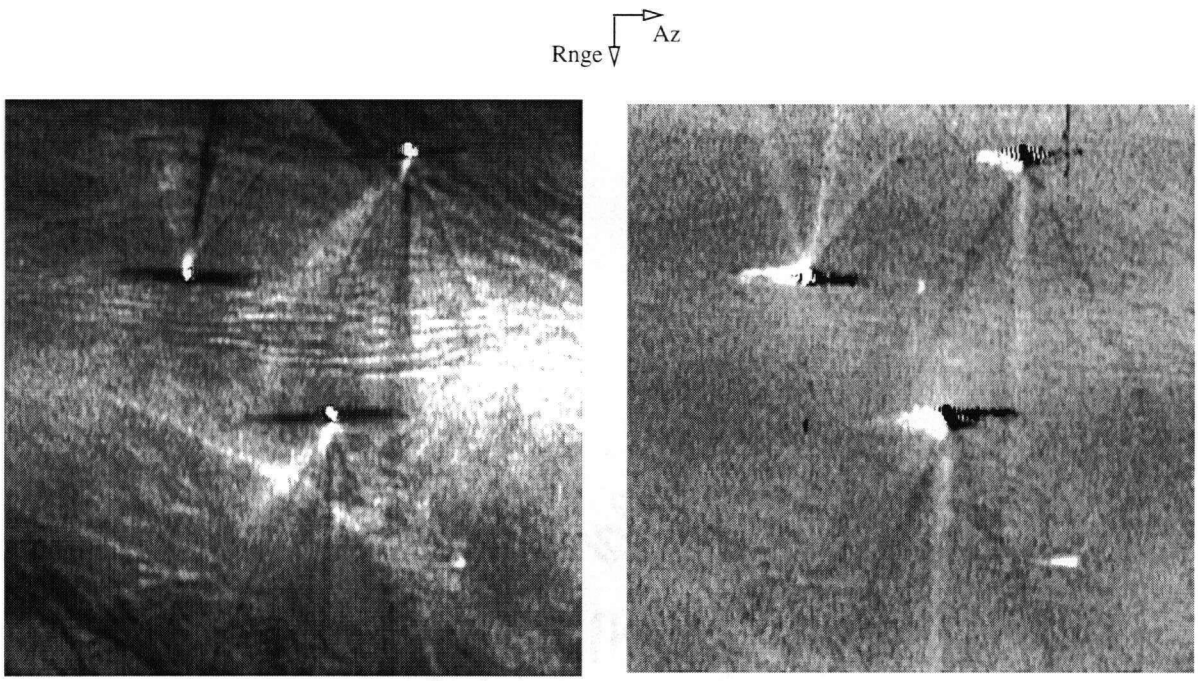

a) Magnitude (Backscatter Intensity) b) Phase (Motion)

Figure 4.3 Backscatter and phase images of Chip #3 of Scene C

The images are the magnitude and phase images of the complex interferogram after azimuth re-alignment, 2-D filtering, and multilooking in azimuth to yield a 1:1 aspect ratio with resolution of 4m x 4m per pixel. The main features of the scene are three passenger ferries (two travelling towards the top of the image, one travelling towards the bottom) and their wakes (A DTW, 2 Kelvin arms and some stern wakes each). Comparing the magnitude and phase images, we can observe that there is significant clutter in the form of non-motion features in the magnitude image. This is because the ships are travelling through a narrow passage (Active Pass between Mayne & Galiano Islands) and the interaction of the wakes of the ships in the narrow channel creates a great deal of surface rippling which show up clearly in Backscatter. We can also see that the centre of the chip is quite bright in magnitude. This is likely because the narrow channel, which also funnels strong surface winds, contains a large number of wind generated Bragg scatterers which result in a bright surface in Backscatter. Such clutter and the brightness due to wind action can mask or hide features in certain instances; though specifically in this case, the wakes are

sufficiently strong to still be distinguishable from background. However, we can see that the wakes, if they were not referenced by their relative position to the bright ship, would be quite indistinguishable from the other features in the scene. In contrast, the only visible features in the phase image are the ships and wakes. The ambient ocean is relatively free of clutter. The phase and magnitude images of other chips of Scenes A, B and C were also generated and are shown at Appendix D for further comparisons.

4.4.2 Phase (Motion Signal) Distribution

The interferogram phase signal distribution of the same scene is shown as Figure 4.4 below:

ACTUAL DATA: Chip 3 of Scene C

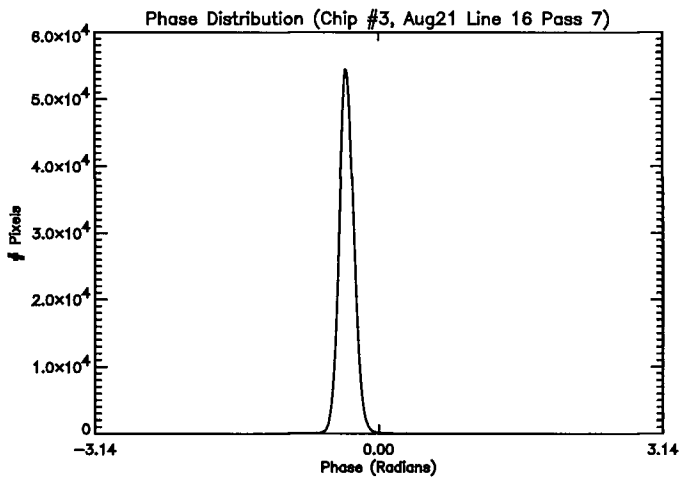

Figure 4.4 Distribution of differential phase in along-track interferograms

We can see from this figure that the phase signal distribution has a very narrow Gaussian profile, which would indicate that:

1. there is motion information present in the phase of the interferogram and that it is estimated from highly correlated data[4];
2. the standard deviation of the represented motion information (velocity and Doppler) is

[4] It is a well known property of single antenna standard SAR images that phase is uniformly distributed and flat [20]. Because the range to the scattering centre of each pixel is random at the wavelength level, the phase of each resolution cell in a standard SAR image is uncorrelated. In contrast, the distribution of differential phase in interferograms (XTI mainly) has been shown, by modeling, to be Gaussian; with the pdf limit of uncorrelated phase being uniform and that of a completely correlated scene being a Dirac delta function [25]. In the case of Along-Track interferometry over the ocean, this Gaussian relationship is even stronger since the Backscatter Doppler power spectrum of the sea is itself modeled as Gaussian [9] and, as we have noted above interferometric phase is a direct estimate of Doppler frequency.

very low or that its precision is high; and

3. that the image has been effectively multilooked [18].

And because it is not Rayleigh distributed, like Backscatter, it would appear that phase is free from fading noise or speckle.

4.5 Comparison of Backscatter and Motion Signal Statistics

The signal statistics of the features in the magnitude and phase image of Chip #3 of Scene A, examined above, were measured and are shown below as Table 4.2 for comparison:

Table 4.2 Signals Statistics of features in Chip #3 of Scene C

	Magnitude (Backscatter Intensity)			**Phase (Motion)**		
feature	**Contrast**	**TBR**	**Size ($1K m^2$)**	**Contrast**	**TBR**	**Size ($1K m^2$)**
Chip #3 Ship	4.23	1.26 (1dB)	6	7.84	14.15 (12dB)	58
Chip #3 DTW	0.08	0.25 (-6dB)	289	0.15	0.55 (-2.6dB)	396
Chip #3 Kelvin Arm	0.46	0.24 (-6dB)	45	0.10	0.75 (-1.2dB)	211

From this table we can see that both contrast and TBR are improved in phase over magnitude, with TBR gains of between 3 to 4dB for the wake features. However, the most notable difference is the greater size of the visible features in the phase image. This could be explained by noting that some features, such as the Kelvin arms of wakes, are imaged by their local tilt angle and depending on its orientation with the radar, as much as half the feature could be invisible (i.e. too low a contrast to be distinguished from background) in Backscatter. However, as phase is not affected by tilt angle, the motion of the entire feature would be visible in phase; effectively making the motion signature of the same feature larger than the Backscatter signature.

The signal and statistics of features in magnitude and phase images of Chip #4, #5, #6, and #7 are listed at Appendix E. From these figures, we further observe the following:

1. the (radial) velocity signature of turbulent wakes were measured to have lower phase value than their local background with phase differences of between 0.04 to 0.16 rad.

This would correspond to waters which are from 0.09 m/s and 0.36 m/s[5] (0.17 knots and 0.71 knots)[6] slower than ambient. The figures appear to be reasonable and the observation, that turbulent wakes damp ambient wave action resulting in a lower velocity compared to ambient;

2. the (radial) velocity signature of the current feature in Chip #3 was measured with phase values that were on average 0.14 rad lower than the local background. This would correspond to waters which are 0.32 m/s (0.32 knots) slower than ambient, verifying our suspicion that this is a current shadow behind a rocky island in a current or tidal flow; and
3. the (radial) velocity signature of the current feature in Chip #8 was measured with phase values that were on average 0.52 rad higher than the local background. This would correspond to waters which are 1.17 m/s (2.3 knots) faster than ambient, verifying our expectation that this is a moderately strong tidal current.

4.6 Modeling

We can support the observations by modeling the speckle and additive noise in the ATI interferometric process and comparing the resulting simulated magnitude and phase signals with the expectation of our error analysis and our observation of the magnitude and phase signal distribution of actual data.

We model the ATI interferometric formation process as a time series of Speckle faded, time decorrelating, complex Backscatter fields, with time intervals matched to the velocity of the aircraft platform (assuming a constant velocity) and the baseline separation between forward and aft antennas. The decorrelation of the background ocean due to the oceans internal random motion was modeled as a series of partially correlated Gaussian distributed random velocity fields. Each complex Backscatter field of the time series was modeled as the sum of a magnitude field, representing the reflectivity of a field of targets in background, and a phase field, transformed from a corresponding velocity field of targets in background, according to the equation:

---

[5] Using equation (4.13) and a nominal platform velocity figure of 126 m/s derived from the mission parameter files, the conversion from interferometric phase to velocity is 1 rad = 2.259 m/s

[6] 1 nautical mile (knot) is 1852 meters. 1 nautical mile per hour (knot) = 0.51 m/s

$$\Phi(t) = u \cdot \left(\frac{2\pi B \Delta t_{\text{interval}}}{\lambda v t} \right) \tag{4.24}$$

where u is the radial velocity of the target and background field, B is the baseline separation of the antennas, v is the velocity of the aircraft, λ, is the wavelength of the radar, Δt, is the selected time interval, and t is the index of the field in the time series. The velocity and Backscatter signal level and variance of the Backscatter and velocity field are adjusted to match as closely as possible the measured Backscatter and velocity level and variance of actual data.

Speckle noise is modeled as a complex Rayleigh distributed fading signal created by summing inphase and quadrature Gaussian random signals to create a multiplicative speckle field. The product of the speckle field and the complex target field is considered the basic radar return signal and contains the Backscatter magnitude and phase information for both forward and aft SLC images. We note here that the phase due to speckle is uniformly distributed, while the phase due to velocity is Gaussian. In the present model, speckle is considered to be completely correlated between images of forward and aft antennas; although it would be a simple task to modify it to include a partially correlated case.

Receiver magnitude noise is modeled as uncorrelated zero mean random Gaussian signals. The amount of correlation is controlled by varying the relative strengths of the correlated and uncorrelated components in the sum, with the uncorrelated component modeled as a time sequence of zero mean random Gaussian with time sequences matched to the separation of the antenna.

A range dependent phase ramp is also included to simulate the uniform phase variation from near to far range present in real SLC images. We note here that because the phase ramp is completely correlated between forward and aft antenna images, it is essentially removed in the interferogram formation process.

The complete ATI signal simulation model is illustrated in block diagram form below as Figure 3.1:

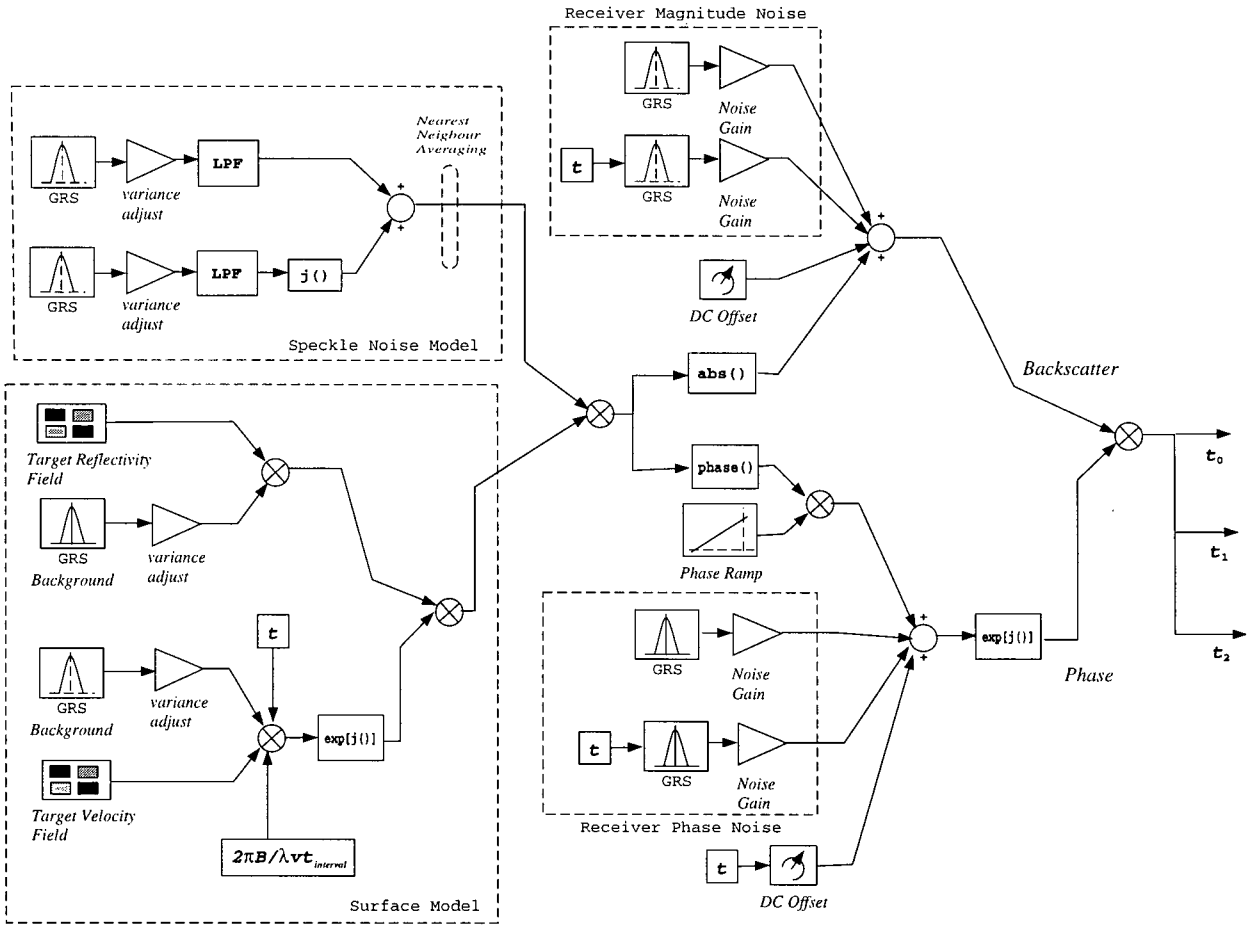

Figure 4.5 ATI Simulation Model

A simulated scene, containing targets in a Gaussian clutter background, was generated and passed through the simulation model. The simulated targets represent the signature of ships with uniformly distributed velocities of average 2.8 m/s and uniformly distributed Backscatter (in non-dimensional units) of average 8, and wakes with average velocity of 1.2 m/s and average Backscatter of 6 (all ship and wake target distribution have a spread of 0.5%). The Gaussian clutter background was given an average velocity of 1.0 m/s and average Backscatter of 4 (background variance of 40% to simulate moderate clutter). The speckle field (fading noise) was set to unity gain, and additive noise was set to -3dB (to simulate heavy receiver & environmental noise) and 50% correlation over the time spread of 2ms between simulated acquisitions of the forward and aft image. The simulated forward and aft images were coregistered and mixed to form the simulated interferogram and the forward image was selected as the simulated single antenna image used for comparison. Both images were 4x multilooked in the azimuth direction.

The results of the modeling are shown below. Figure 4.6 shows the Backscatter images of the simulated forward antenna, and the Backscatter and phase of the simulated dual antenna interferogram.

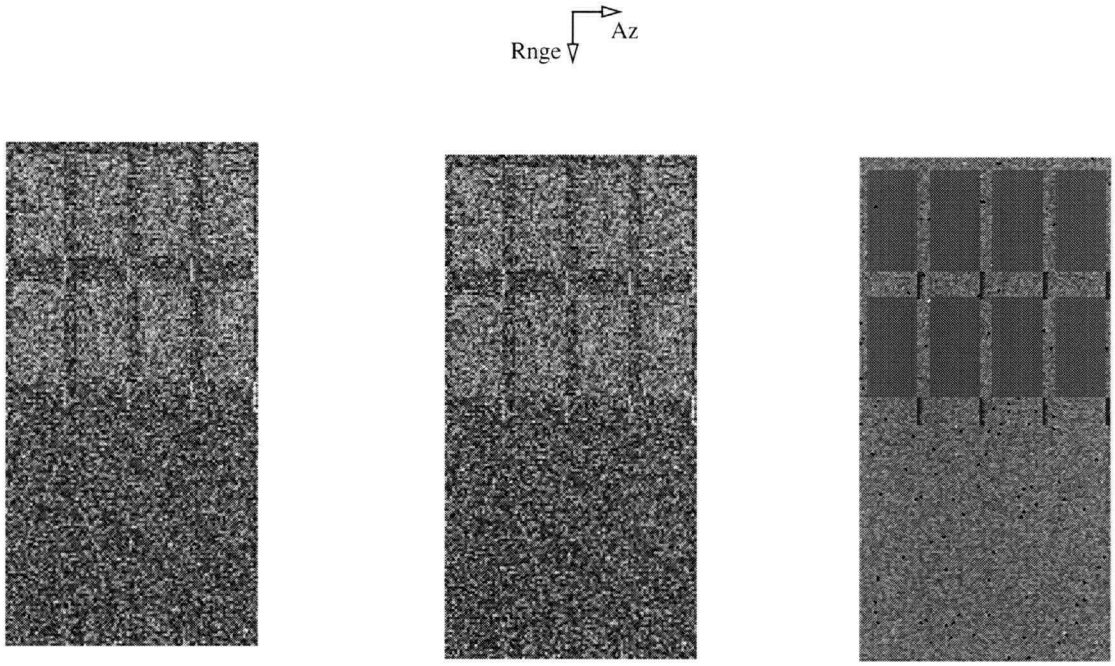

a) Backscatter Magnitude Forward Antenna

b) Backscatter Intensity Dual Antennas

c) Interferometric Phase Dual antennas

Figure 4.6 Simulated Backscatter and Phase Imges

From this figure, we can see the targets in the Backscatter images are difficult to distinguish from the background, being heavily faded by speckle noise and strongly affected by heavy additive noise. In contrast, we can see that the targets, both simulated ship and wake, are readily distinguishable in the phase image, indicating that the motion signature of the targets are little affected by speckle fading and additive noise.

Figure 4.7 below, shows the distribution of the Backscatter intensity signal of the simulated interferogram and the Backscatter magnitude signal of the simulated single antenna image.

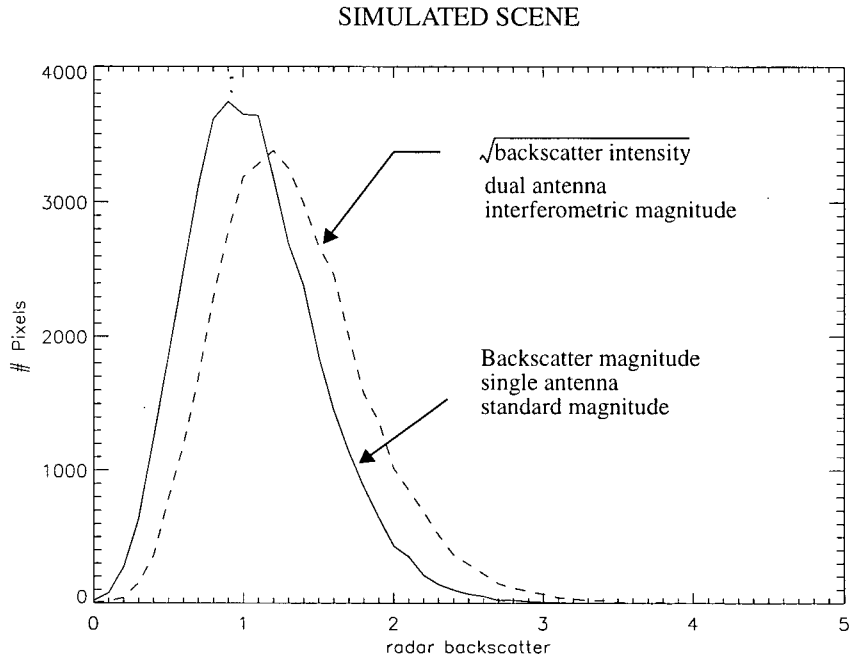

Figure 4.7 Comparison of distribution of simulated radar Backscatter signals from single antenna and dual antenna interferometric magnitude Simulated Image

We can see from this plot that, like plot of the Backscatter signals of the actual data, Figure 4.2, the Backscatter magnitude of the single antenna is Rayleigh, indicating the effects of the speckle fading, and the Backscatter intensity of the interferogram is more Rician, being centred more towards the right of the distribution.

Figure 4.8 shows the distribution of the phase of the simulated interferogram. We can see from this plot that, like the plot of the interferometric phase of the actual data, Figure 4.4, the distribution of the motion signature in the simulated image is very narrow and Gaussian, indicating that it is dominated by clutter and unaffected by the speckle fading.

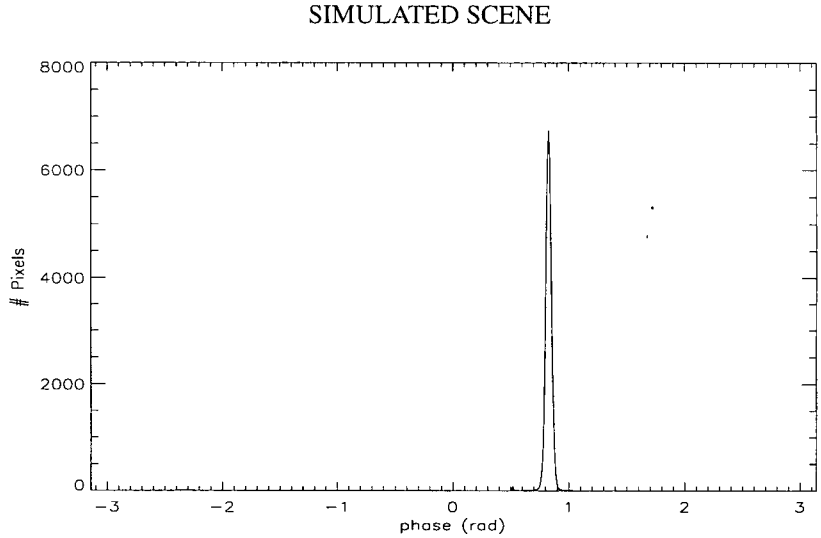

Figure 4.8 Distribution of differential phase in Simulated along-track interferogram

The simulation model would, thus appear to support the conclusions of our error analysis of noise in the mixing operation and analysis of (Backscatter and motion) signal distributions, that the interferogram formation process is inherently noise rejecting and that the phase of interferograms, which is the estimate of motion, is free from the effects of speckle fading.

Chapter 5 Theoretical Performance

The theoretical performance (i.e. velocity precision) of C-band SAR Along-Track Interferometers can be determined by examining the relationship between the standard deviation of the velocity estimations in the along-track interferometer configuration and system and scene parameters, such as coherence, Clutter to Noise Ratio (CNR) and baseline. This can be done by parametric analysis of the Cramer Rao lower bound of the autocorrelation of two complex SAR signals; which contains a description of the relationship between velocity standard deviation and the geometry of the interferometer and coherence in the scene. In this analysis, velocity standard deviation is considered to be sufficient means to describe the theoretical precision of the velocity estimate. The method employed here is similar to that employed by Rodriguez [28] for general SAR interferometers and Carande [21] for L-band dual (physically separated) antennas SAR ATIs. The results were compared with the published performance specifications of an experimental C-band SAR, the CCRS CV580 C-band SAR ATI. The effect of azimuth defocusing is not considered in this analysis.

5.1 Velocity Standard Deviation

The Cramer Rao lower bound for the phase standard deviation, σ_Φ, of SAR interferometers was shown by Rodriguez [28] to be:

$$\sigma_\Phi = \frac{1}{\sqrt{2N}} \frac{\sqrt{1-\rho^2}}{\rho} \tag{5.1}$$

where ρ is a correlation parameter and N is the number of looks averaged. In ATI, the correlation parameter can be considered equivalent to coherence magnitude, $|\gamma|$, which was examined in Chapter 3 and was defined as:

$$\rho = |\gamma| = \left| \frac{E\{xy^*\}}{\sqrt{E\{|x|^2\}E\{|y|^2\}}} \right| \tag{5.2}$$

Coherence magnitude has a valid range of from 0 to 1 with 0 representing no correlation between the fore and aft images. In this report, we will use the terms coherence and correlation interchangeably.

Equation (5.1) is converted to a velocity standard deviation, σ_u, using the geometric phase to velocity model:

$$u = \left(\frac{\lambda v}{2\pi B}\right)\Phi \tag{5.3}$$

where λ is the wavelength of the radar, v is the velocity of the aircraft, Φ is interferometric phase, u is the radial velocity of the imaged surface, and B is the baseline separation between the ATI antenna pair. From (5.1) and (5.3) we obtain the following expression[1]:

$$\sigma_u = \left(\frac{\lambda v}{2\pi B}\right)\frac{1}{\sqrt{2N}}\frac{\sqrt{1-\rho^2}}{\rho} \tag{5.4}$$

We note that the geometric phase to velocity expression of (5.3) is for a *Bistatic* interferometer, in which the radar pulse is transmitted from only one antenna and the return pulse is received by both forward and aft antennas simultaneously. The effective baseline of the antenna pair in a bistatic interferometer is actually B/2, which is accounted for in the bistatic case of ATI expressions by a factor of 1/2. Throughout this analysis, the bistatic case of all radar expressions is used and B refers to the physical baseline separation between antennas. For a static or dual transmit mode of operation, where both antennas alternately transmit and receive, the term $2\pi B$ can be replaced with $4\pi B$.

5.2 Velocity Standard Deviation and Correlation

The relationship between velocity precision and the operating parameters of the ATI can be examined by separating the correlation parameter in equation (5.1) into components which are functions of clutter to noise ratio, baseline separation and scene coherence.

We can see from (5.4) above that the velocity precision is directly related to a correlation variable and the operating parameters of the ATI, which we define to be its:

1. platform velocity;
2. baseline separation between antenna phase centres;

---

[1] $\sigma(u) = \sigma(k\Phi) = k\sigma(\Phi)$ for k constant with respect to Φ

3. radar wavelength of the transmitted pulse;
4. the beam incidence angle; and
5. CNR

We note that the last two parameters, beam incidence angle and CNR, are not explicitly included in (5.4), but are part of the correlation variable. The correlation variable, ρ, which describes the degree of similarity between the two SLC images which are taken at slight distances and times apart, is a function of the sensor system and the *Coherence* in the scene, or the degree to which the scene remains similar or unchanged over time.

This can be seen by examining the system correlation, ρ_{total}, which is a function of the sensor system and the scene and is expressed as:

$$\rho_{total} = \rho_{receiver} \cdot \rho_{temporal} \tag{5.5}$$

where $\rho_{receiver}$ is 1 minus the decorrelation due to receiver noise, $\rho_{temporal}$ is 1 minus the decorrelation due to changes in the scene (which in the case of an ocean scene, is a function of ocean coherence time and the baseline separation length).

Receiver Decorrelation: The decorrelation due to receiver noise, which includes both noise in the scene and noise in the receiver itself, is:

$$1 - \rho_{receiver} = 1 - \frac{1}{1 + CNR^{-1}} \tag{5.6}$$

The factor, CNR, is the ocean clutter to noise ratio and is defined as the ratio of the normalized radar cross section, σ^0 which represents the clutter or signal in the scene, to the noise-equivalent normalized radar cross section, σ_{NE} which represents the noise in the receiver itself [29]:

$$CNR = \frac{\sigma^0}{\sigma_{NE}} \tag{5.7}$$

The normalized radar cross section, σ^0 , is a function of the wind speed and wind direction over

the scene and local incidence angle of the radar. In this analysis we use values of normalized radar cross section, σ^0, derived by CCRS from the CMOD5 empirical model [30].

Temporal Decorrelation: Temporal correlation can be modeled by an exponential correlation model [21], expressed as:

$$\rho_{temporal} = \exp\left(-\frac{t}{T}\right) \tag{5.8}$$

where t is time and T is a Coherence Time constant related to the coherence time, t_c, of the ocean via the expression:

$$T = -\left(\frac{t_c}{\ln(0.5)}\right) \tag{5.9}$$

We note that the *Coherence Time* of the ocean, t_c, is defined as the time at which the normalized magnitude of the autocorrelation of a wave image degrades to 1/2 [21]. A plot of the temporal correlation of an ocean scene (equation (5.8)) at various coherence times from 10 ms, 20ms, 50ms, 100ms, 150ms, and 200ms is below as Figure 5.1.

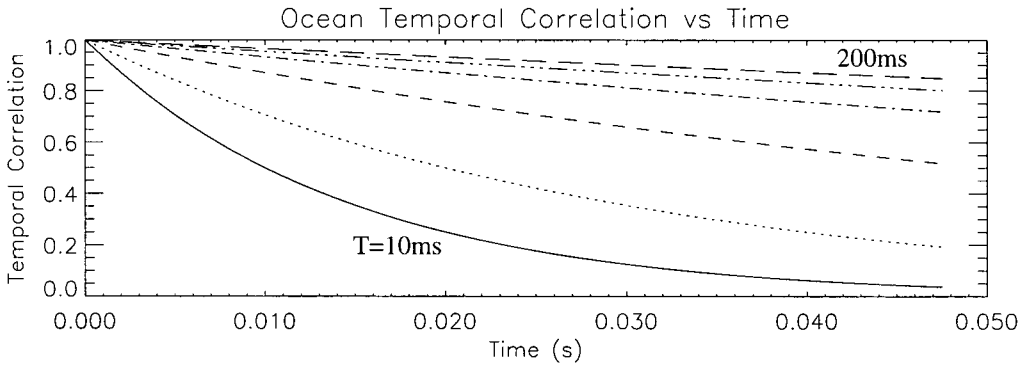

Figure 5.1 Temporal correlation of an ocean scene at various coherence times

We note that interferometric processing requires phase coherence somewhat different from conventional (non-interferometric) SAR processing. We suspect that the phase of the autocorrelation of complex images degrades faster than the magnitude image over coherence time. This was considered to be

beyond the scope of the current research and could be a topic for future study.

5.3 Operational Parameters

From equation (5.4) and (5.5) we can see how operating parameters affect velocity estimation precision.

Sensor platform velocity: Higher platform velocities contributes to diminishing velocity precision via the geometry term (5.3), but contributes to improving velocity precision via the correlation term (5.5). The effect of platform velocity on the geometric term is linear and it is nonlinear on the correlation term. The effect of this is less sensitivity of velocity precision to improvement with larger baseline in the short baseline range and less sensitivity of velocity precision to degradation with larger baseline in the long baseline ranges.

Baseline separation: The effect of varying baseline separation on velocity precision is the inverse of that of platform velocity. Longer baselines contribute to velocity precision improvement via the geometric term, but contributes to diminishing velocity precision via the correlation term. Because the correlation term is nonlinear while the geometric term is linear, the velocity precision curve will exhibit a rapid improvement in precision in the short baseline range and slower diminishing precision in the long baseline ranges.

Scene Clutter to Noise Ratio (CNR): The CNR parameter, which incorporates scene clutter, receiver noise, and transmitted power, sets the maximum correlation and minimum velocity precision of the interferometer via the correlation term (5.6).

Beam incidence angle: High incidence angles result in lower surface clutter reflectivity (i.e. σ^0 the radar cross section) whereas lower incidence angles result in higher surface clutter reflectivity from (5.7). Higher surface clutter reflectivity improves the CNR of the interferometer and thereby improves the velocity estimate precision via the correlation term (5.6). We note, however, that in conventional SAR ship detection, high surface clutter reflectivity results in high brightness levels which tends to mask targets.

Radar wavelength: Shorter radar wavelengths contribute to improved velocity estimate precision via the geometric term (5.3). This effect is linear. A useful performance figure of merit incorporating wavelength is $\frac{\lambda}{B}$, the wavelength/baseline ratio from (5.3).

5.4 Analysis

We examine the theoretical performance of a C-band SAR ATI modeled on the CCRS CV580 C-band ATI. The CCRS CV580 C-band ATI uses an HH polarization, operates at a frequency of 5.3 GHz (λ= 0.0566m) and uses a single split feed antenna with dual phase centres displaced by a distance of 0.5m. The incidence angle of the main beam of the antenna is 55 degrees from Nadir. The Convair CV580 platform flies at a nominal ground speed of 126 m/s.

Using the expression of (5.4), we calculate and plot the velocity standard deviation of a 0.5m baseline C-band along-track interferometer, like the CCRS C-band ATI, over the range of possible coherence magnitude values from 0.00 to 1.00 and the more practical range of 0.85 to 0.99 for several choices of number of looks, N = 10 to 50, in increments of 10. The CV580 nominal ground speed figure of 126 m/s was used in this calculation. We show this plot below as Figure 5.2:

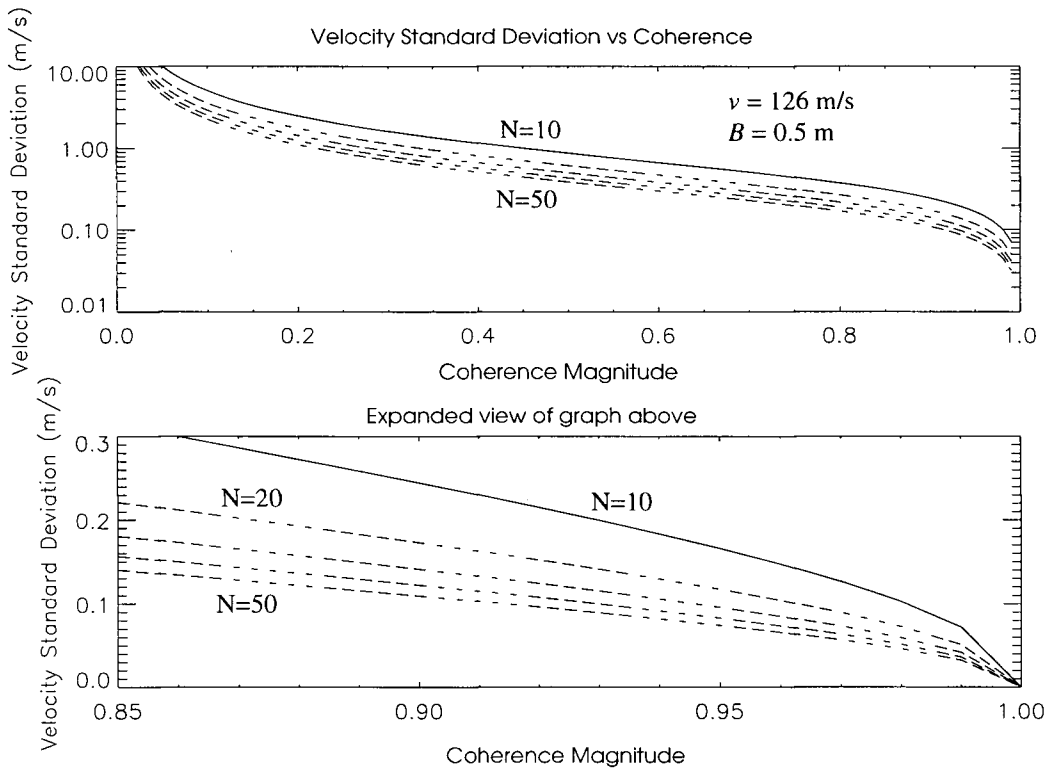

Figure 5.2 Velocity standard deviation vs. coherence of an airborne 0.5m separation C-band ATI for 10 to 50 looks in increments of 10 looks

We can see from Figure 5.2, that at a coherence value of 0.96 and 20 looks the velocity standard

deviation is 0.13 m/s (0.24 knots). This can be considered the theoretical velocity precision of the CCRS C-band SAR ATI at the average coherence level of 0.96. We note that 0.96 was the average coherence measured in the C-band ATI SLC image pair we were provided and 19 looks is the averaging required to square the aspect of the CCRS ATI interferograms (and the averaging we employed in all of our analysis of Chapter 3 and 4).

Using the temporal decorrelation model of equation (5.8) in equations (5.5) and (5.1), we can now calculate the variation in velocity standard deviation over varying baseline separation. We calculate and plot this for typical coherence times, from 10ms to 200ms, and at 19 looks. For this calculation, we use a nominal value of -41dB for the noise equivalent normalized radar cross section figure, σ_{NE}, calculated from [12] and nominal values of -6dB and -12dB for the ocean radar cross section, σ^0 for windspeeds of 10m/s and 4m/s respectively, calculated at 27.5 degrees[2] incidence angle from [29]. This plot is shown

[2] 27.5^o is the mid swath incidence angle of the Nadir mode incidence angle range of 0^o to 55^o of the CCRS C-band SAR [12].

below as Figure 5.3:

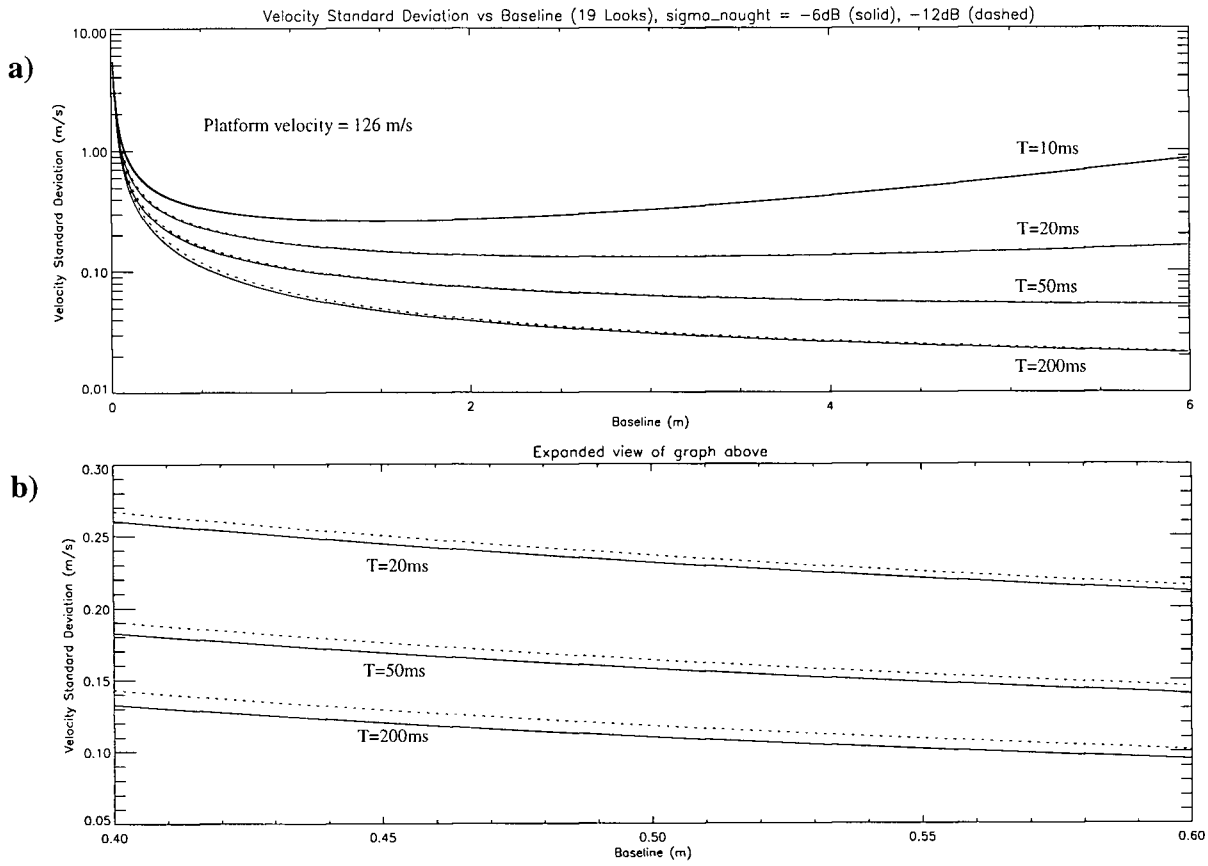

Figure 5.3 Velocity standard deviation versus baseline separation of an airborne C-band ATI at various coherence times [10ms, 20ms, 50ms, and 200ms] and 19 multilooks. Solid lines = -6dB sigma_naught, dashed lines = -12dB sigma_naught

From Figure 5.3a, we can see that as we first increase the baseline separation between antennas, velocity standard deviation drops. The first part of the curve, over which the velocity estimation improves rapidly with increasing baseline, is dominated by the geometric velocity to phase term (the geometric term or baseline sensitivity):

$$\frac{\lambda v}{2\pi B} \tag{5.10}$$

The middle part of the curve, over which the velocity estimation improves more slowly with

increasing baseline, is dominated by the system correlation term, ρ, and more specifically by the ocean coherence time. The estimation improves slowly with increasing baseline until the baseline is such that the time lapse between forward and aft antennas begins to exceed the coherence time of the ocean, at which point the velocity estimation begins to degrade.

At a baseline separation of 0.5 m, the velocity standard deviation varies between 0.11m/s (0.21 knots) for a scene with coherence time of 200ms and 0.16m/s (0.30 knots) for scene with coherence times of 50ms in conditions of higher surface windspeed, i.e. σ^0= -6dB. The standard deviation at lower windspeeds, σ^0= -12dB, are approximately 0.01m/s (0.02 knots) larger at 0.5 m baseline separation. Noting that the unambiguous velocity range of the CCRS airborne C-band ATI, calculated from equation (5.3), is +/- 7.1 m/s, this would represent a precision of better than 1%.

Comparing this with the results of section 2.1, we can deduce that the average coherence time of the ocean scene of the CCRS CV580 C-band ATI image examined in Chapter 3 was likely in the region of 100ms to 150ms. This is because the velocity standard deviation at a coherence level of 0.96 and 20 looks from Figure 5.2 is 0.12 m/s, which corresponds to a coherence time of between 100ms and 150ms in Figure 5.3.

As the baseline separation, considered with respect to the velocity of the sensor platform, approaches the coherence time of the scene, $\frac{B}{v} = t_c$, the velocity standard deviation increases and velocity estimation precision degrades. We note that for each coherence time and platform velocity, there exists a range of optimal baseline separations where velocity standard deviation is minimized. In the case of an airborne C-band ATI travelling at 126 m/s, this optimal baseline is in the range of 2m to 4m for slow ocean scenes with coherence times greater than 100ms. We can see that, although the relatively short baseline of 0.5 m at the nominal flying velocity of 126m/s of the CCRS CV580, is not in the optimal range for C-band imaging of slow ocean scenes with coherence times of around 100ms, for more dynamic ocean scenes which have coherence times of less than 20ms, the 0.5 m baseline is near the optimal range.

It would appear then that the 0.5m baseline of the CCRS C-band ATI configuration is generally well suited for imaging fast and/or low amplitude velocity features, such as ship wakes. However, the relatively short baseline of the CCRS ATI, necessitated by the practical size of the antenna and limitations of the system, does not appear to be as well suited for imaging more slowly varying patterns of very long wave structures, as would a much longer baseline or shorter wavelength SAR ATI.

5.5 Factors for Optimal Ship Detection

From the above analysis, we can conclude that the key parameters in achieving optimal velocity precision are platform velocity and baseline separation. In the case of ship wake detection, an airborne system with platform velocity on the order of 126m/s and baseline separation between 0.5m and 4m would have adequate velocity precision to detect most ship wakes. However, apart from baseline separation, velocity precision can be improved by adjusting other operational parameters. These include:

1. Increasing transmitted power, which would increase CNR and improve velocity precision via the correlation term of (5.4);
2. Imaging at a lower incidence angle, which would increase surface reflectivity and clutter and improve velocity precision via the CNR and the correlation term of (5.4); and
3. Switching to a smaller beam wavelength, such as X-band or Ku-band. This would decrease the beam wavelength to baseline ratio and improve velocity precision via the correlation term. (It is interesting to note that some operational displaced phase centre antenna interferometers, such as the USAF E-8C JSTARS, uses Ku-band).

Chapter 6 Detection Performance Analysis

In the previous chapters, we indirectly examined the detectability of ships, wakes and ocean feature in ATI interferograms by examining the signal information in interferograms and the effect of the ATI formation process on the coherence, frequency distribution, signal statistical, and visual presentation of the component Backscatter (magnitude) and motion (phase) images.

In this chapter we directly examine the detectability of ships, wakes and ocean feature targets in Backscatter and motion images. We first qualitatively examine the visual detectability of targets and features in Backscatter and motion images, then quantitatively examine their detection statistics. To do this we define a figure of merit to quantify detectability and apply it to ship and wake targets in Backscatter and motion images derived from ATI interferograms. We also measure and compare the spatial signal profiles of significant features to further support observations. And finally, we apply a 'litmus test' to our observations and conclusions by passing the data through a model target detector; a simple CA-CFAR (Cell Averaging - Constant False Alarm Rate) detector in this case, and comparing its results to our observations.

6.1 Visual Detection of Targets in Motion and Backscatter

The motion (phase) and Backscatter (magnitude) images, derived from ATI interferograms, of Chip #2 of Scene A, Chips #4 and #5 of Scene B, and Chip #3, #6, #7, and #8 of Scene C are shown as Figure 4.1 thru Figure 4.14 of Appendix D. These images are shown in filtered and unfiltered state for visual comparison.

From these images, we observe that, in general, there would appear to be less background detail and clutter in the visual presentation of unfiltered phase images than in unfiltered magnitude images. And after filtering, the background would appear to be more homogeneous in phase than in magnitude. This can be seen quite clearly by comparing the unfiltered and filtered phase and magnitude images of Chip #2, Figure 4.1 and Figure 4.2, and Chip #3, Figure 4.3 and Figure 4.4.

And we observe that some large scale wave disturbances are visible in phase, whereas they are not visible and not detectable in magnitude. These include:

1. a plume-like feature in Chip #4 of Scene B, that is likely a current shadow (a region of slower moving water) in the lea of an island caused by a strong tidal or oceanic current stream, shown in Figure 4.5 and Figure 4.6; and

stream, shown in Figure 4.5 and Figure 4.6; and

2. a large wave feature in Chip #8 of Scene C, that is likely the strong tidal current that flows through Active Pass, a narrow channel, between Galiano and Mayne Islands off Vancouver Island's east coast near Victoria, shown as Figure 4.13 and Figure 4.14.

The presence of these features in phase but not in Backscatter could be explained by noting that some imaging mechanisms, such as differential motion of Bragg scatterers, could result in highly differentiated velocity, but no Backscatter contrast. In these two examples, the Backscatter of the wave disturbance features and that of the surrounding waters are the same because the wave disturbances have very little surface manifestation (even optically, the wave disturbances are not very distinct from their background), they probably have the same density of Bragg scatterers and are at the same tilt angle. However, the velocities of the waters are quite different and thus they are quite well differentiated and distinctly visible in interferometric phase. In the case of Chip #4, the channel, Active Pass, is a busy ferry route and is well known to have a moderately strong subsurface current. And in the case of Chip #8, the surface in the parent scene appears in Backscatter to be a relatively flat and featureless and was probably taken when there was little surface wind to generate much Bragg or specular scattering.

Similarly, some features may be clearly visible in magnitude but not in interferometric phase. This is particularly true for relatively stationary features whose lack of differential velocity would result in very little phase contrast. These features, however, may contain corner reflector-like surfaces (such as the superstructure of a ship) or have significantly different tilt angles and/or contain more or less Bragg scatters than their background, making them highly visible in Backscatter. An example of this is the scene in Chip #5, Figure 4.7 and Figure 4.8, where three small slow moving ships are represented with higher contrast in Backscatter than in motion. In general, bright and/or stationary targets, such as ship and land features, have higher contrast and are more distinct in magnitude images than in phase images.

6.2 Detectability of Targets in Motion and Backscatter

6.2.1 Detection Figures of Merit

In order to rate the detectability of targets in ATI images, we define two simple Detection Figures of Merit, the *Probability of Detection* and the *Detection energy*. These are related to TBR as follows:

$$P_d = \frac{1}{2}\left[1 + \mathrm{erf}\left(\frac{\mathrm{TBR}}{2\sqrt{2}}\right)\right] \tag{6.1}$$

where P_d is the probability of a generalized ML detector (from equation (2.6) of Appendix B) detecting a single pixel of a feature in a Gaussian noise/clutter background and erf() is the Gaussian error function. This is a lower bound of detectability, where the performance of specific target detectors, such as a CA-CFAR detector, will be equal to or greater than this value [26]. If we assume that every pixel in an ATI interferogram is independent and spatially uncorrelated from its neighbouring pixels, then we can define the cumulative detection probability of a feature as the expectation of the total number of pixels, in a 2-D field, detected and associated with it. We will call this its *detection energy* and express it as:

$$\text{Detection Energy} = P_d \cdot (\text{area of feature}) \tag{6.2}$$

6.2.2 Detection Figures

From the filtered Backscatter and motion images Chips #1 and #2 of Scene A, Chips #3, #6, #7 and #8 of Scene C and Chips #4 and #5 of Scene B, we calculated detection figures of merit from the measured signal statistics of the representative targets and background, which were measured in Chapter 4 and are listed in Appendix E.. These calculated detection figures of merit are compared below with each other and visual observations and analysis spatial profiles are used to support observations. The basic signal statistics and the calculated detection figures of merit of several ship, wake and ocean feature targets are listed below as Table 6.1 for comparison;

Table 6.1 Comparison of detection metrics of features in interferometric magnitude and phase

	Magnitude (Backscatter Intensity)					Phase (Radial Velocity)				
feature	**CI**	**TBR**	**Size (1K m^2)**	**Diff P_d%**	**Det energy**	**CI**	**TBR**	**Size (1K m^2)**	**Diff P_d%**	**Det energy**
Chip #3 Ship	4.23	1.26	6	24	4	7.84	14.15	58	50	58
Chip #3 DTW	0.08	0.25	289	5	159	0.15	0.55	396	11	241
Chip #3 Kelvin Arm	0.46	0.24	45	5	25	0.10	0.75	211	15	136
Chip #3 Stern Wake	n/v	n/v	n/v	n/v	n/v	n/v	n/v	n/v	n/v	n/v
Chip #4 Land	22.9	1.53	179	28	139	0.95	6.68	270	50	270
Chip #4 Current Shadow	0.32	0.07	n/v	1	n/v	0.31	1.77	3360	31	2729
Chip #5 Small Ships	16.5	1.05	8	20	6	0.28	1.07	16	20	11
Chip #6 Linear Wake	0.13	0.51	110	10	66	0.16	0.75	130	15	84
Chip #7 Ship	1.52	1.86	2.4	32	2	1.93	4.27	5.8	48	6
Chip #7 Linear Wake	0.43	0.15	12	3	6	0.49	1.17	48	22	35
Chip #8 Land	19.8	1.91	n/a	33	n/a	0.98	4.65	n/a	49	n/a
Chip #8 Tidal Current	0.61	0.18	n/v	n/v	n/v	1.61	3.15	n/v	44	n/a

From these figures, we can observe the following:

1. that both TBR and Probability of Detection are greater in phase than in magnitude, with improvements in detectability of between 50% - 80% for typical wake features (200% - 600% for exceptional cases, such as a fast moving wake features) and improvement in TBR of motion signatures being between 0.3dB and 13dB. The greatest TBR difference was observed in fast moving features such as the ship in Chip#3

and the two current features in Chip #4 and Chip #8. The difference in TBR of slower moving ship wake features was consistently around 2dB. The TBR of nearly stationary and small bright features, such as the small ships in Chip #5 were roughly equal (relatively stationary ships do have significant pitch and roll motion components which, although not contributing to wake generation, may nevertheless make the ships themselves visible in phase);

2. that, in general, the visible size of features in phase tends to be larger than in magnitude. In some cases, this is because the region of differentiated velocity of some features is larger than the region of differentiated Backscatter. However, we suspect that this may also be because the smearing effect of azimuth defocusing is more severe in interferometric phase than in Backscatter. We will examine this further in Section 6.2.3;
3. that although the TBR and differential detection probability of ships were much greater than subtle wake features, because of their very small (point target like) size, they had much smaller detection energy than wakes;
4. that the detection energy of all features was greater in phase than in magnitude;
5. that although ships are, in general, quite bright, the small ships in Chip #5 are unusually bright in magnitude. We note that many small sailing vessels are equipped with radar corner reflectors to make them more visible to marine traffic radar, and that this could be a possible reason for the unusually high Backscatter in some small ships.

Thus it would appear that, in most cases, the probability of detecting faint or subtle targets, such as wave features and ship wakes, from their motion signature is slightly greater than detecting the same target from its Backscatter signature. This observation and the visual observation, above, that there tends to be less clutter in the phase presentation of ATI interferograms than in magnitude presentation, would appear to validate our observations in Chapter 4, that the formation of interferometric phase inherently rejects more clutter noise than the formation of interferometric magnitude or Backscatter intensity; and that both rejected more clutter noise than simple Backscatter magnitude from standard SAR. We also observe, however, that clutter does help to give the appearance of texture and imparts a photograph-like quality to magnitude images, which is more visually representative of reality than the presentation in phase images.

6.2.3 Spatial Profiles

We can further support some of these observations by examining the spatial profiles of some significant features. We obtained spatial profiles of significant features and their background by measuring the signal level (magnitude and phase) along slices taken along and across the major axis of the features or prominent regions and surrounding background. For the most part, the spatial profiles of features were similar in Backscatter and motion with the following significant exceptions:

1. A bright point target was identified in the Backscatter spatial profile of the small linear wake feature of Chip #2 of Scene A. This bright point target is likely a fast small craft that generated the small turbulent wake visible in both motion and Backscatter. The position of the small craft can be clearly seen in the Backscatter profile, shown below as Figure 6.1a), but is difficult to distinguish from the wake feature in the motion profile, shown below as Figure 6.1b). Because of smearing, the point target identified as 160 m long in Backscatter, cannot be separated spatially from the smeared linear wake which is three times as long, at roughly 400 m, in the motion profile.

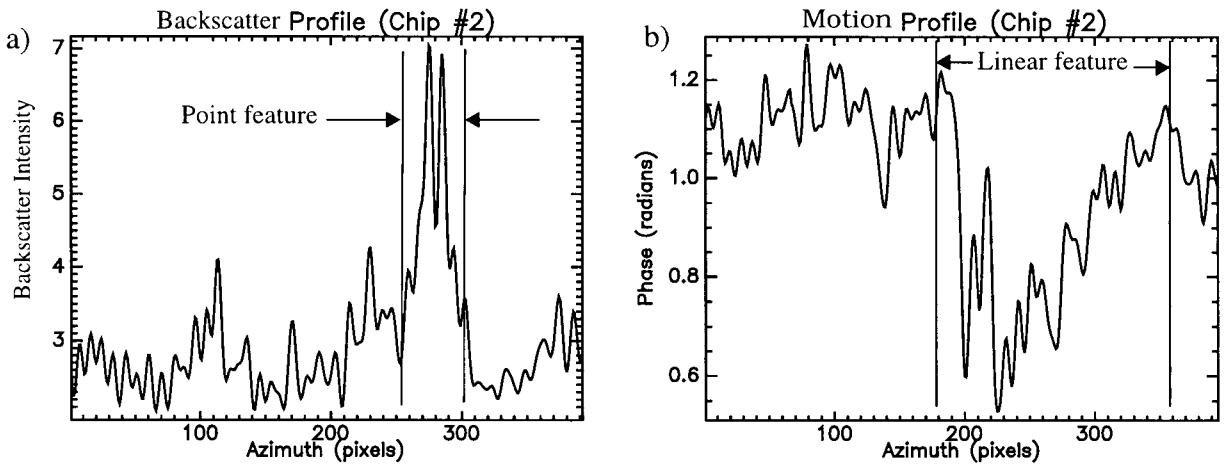

Figure 6.1 Motion and Backscatter profiles of linear wake feature in Chip #2 of Scene A

2. The bright passenger ferries in Chip #3 of Scene C was found to have a similarly narrow profile in Backscatter, shown below as Figure 6.2a). In phase, its profile shown below as Figure 6.2b) is so smeared it is not readily identifiable as a discrete feature such as a ship. Additionally, in Backscatter, the ship's position is readily distinguishable to within 30 azimuth pixels (120m), but is difficult to determine in phase, being

smeared across nearly 200 azimuth pixels (800m). We also note that a 2π phase jump is apparent in the centre of the smeared phase profile.

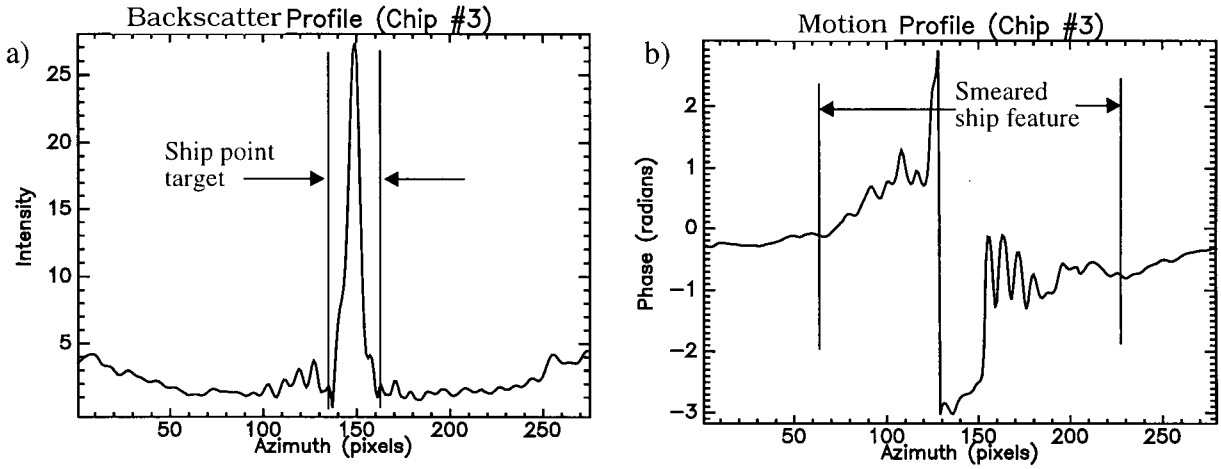

Figure 6.2 Motion and Backscatter intensity profiles of bright ship feature in Chip #3 of Scene C

3. The stern wake details corresponding to the three ferry size ship features of Chip #3 of Scene C are not visible in either Backscatter or motion images after LP filtering. This is not surprising, since the range travelling stern wakes are of such fine detail, with widths (in range) of less than 25 pixels (100m). It is likely that the averaging effect of the range filtering operation smeared the fine lines of the stern wakes. It should be noted that these stern wake features are only visible at all, because they are range travelling and therefore unaffected by the azimuth multilooking (subsampling) and azimuth defocusing. Had these stern wakes been other than range travelling, they would have in all likelihood been invisible in both magnitude and phase after azimuth downsampling / multilooking;
4. The large scale current shadow in Chip #4 of Scene B, which was clearly visible in motion but not in Backscatter, is similarly evident in the motion profile, shown as Figure 6.3d), and similarly indistinguishable in Backscatter profile, shown as Figure 6.3b). The differential phase of 0.20 rad between the peak of the current feature and the background would correspond to a differential velocity of roughly 45 cm/s or 0.89 knots. The spatial profiles of Chip #8 of Scene C show similar differences between the motion and Backscatter with a peak differential phase between land and current of 1.0 rad corresponding to differential velocity of 2.25 m/s or 4.4 knots.

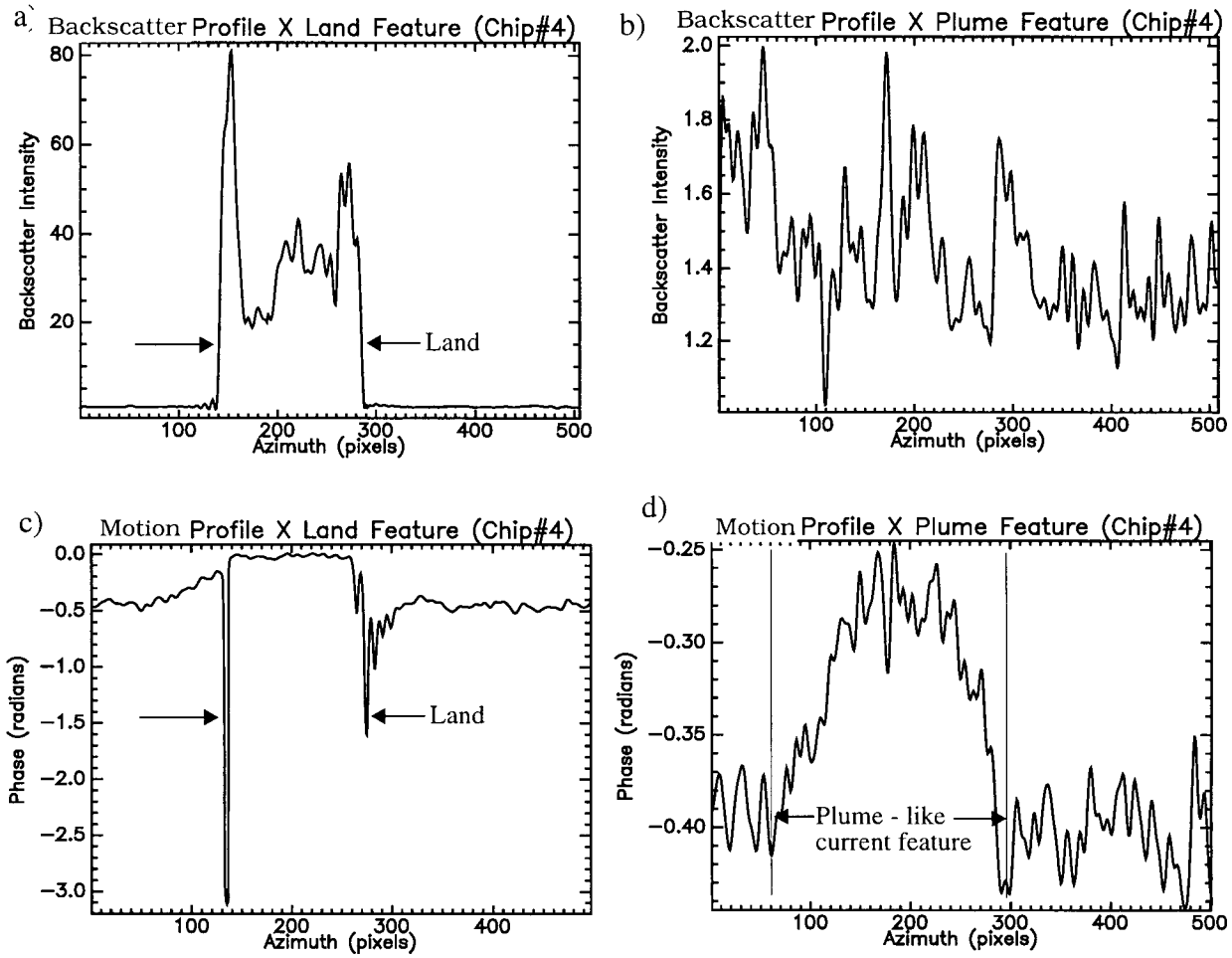

Figure 6.3 Backscatter and motion profiles of land and current shadow feature in Chip #4 of Scene B

The spatial profile of Backscatter and motion images would appear to indicate that smearing due to azimuth defocusing affects features in phase more than in magnitude (although, the more spread out, less distinct spatial profile of ship features in phase may be due to the combined effects of defocusing and simply a larger spread of the velocity fields) and that features, such as large scale currents or subsurface wakes, which have differential velocities of as little as 0.89 knots are distinguishable from their motions signature even though they are completely indistinguishable by their Backscatter signature.

6.3 Performance of a Target Detector on Backscatter & Motion Images

As a final test of our observations, we apply a simple target detector to sample phase and magnitude images and observe and compare the performance of the detector on Backscatter and motion

signatures of targets. We also apply simple fusion algorithms on the detector products in an attempt to improve the overall detection of the often very faint signature of ship wakes. The adaptive Cell Averaging - Constant False Alarm Rate (CA-CFAR) detector used here was implemented in the IDL environment.

6.3.1 CA-CFAR Detectors

A CA-CFAR detector can discriminate a pixel of an image associated with a target (called a cell) from background clutter if the signal level of that cell is above a certain threshold; the threshold level being determined 'on the fly', by sampling, using a moving window, the background statistics in the cell's nearest neighbours. The Pearson-Neyman criteria, or another similar criteria, and a predetermined uniform false alarm rate (equation (2.9) of Appendix B) are used to adaptively calculate this threshold 'on the fly'.

In our implementation of a CA-CFAR detector, a moving window of 31 pixels x 31 pixels samples the neighbouring cells around each Cell Under Test (CUT), to determine an estimate of the local noise, σ. The central cell and its immediate neighbours are excluded from the estimate by a 5 pixel by 5 pixel exclusion mask around the CUT. This prevents any spillover of the CUT from affecting the estimate. The threshold was determined by multiplying this by a factor, k. For the subject images, we found that a factor, k=1. (i.e. 1 sigma) yielded reasonably good results. Using this factor results in a nominal constant false alarm rate of less than 16%. The output of the detector can then be displayed in an image that represents the results of the detector's efforts to discriminate targets in the dimensions of the original Image Under Test (IUT); which we will call the target map. The values of target map are binary numbers with 1, denoting a pixel considered by the detector to be a target, and 0, denoting a pixel not considered by the

detector to be a target. A functional block diagram of the detector is shown below as Figure 6.4.

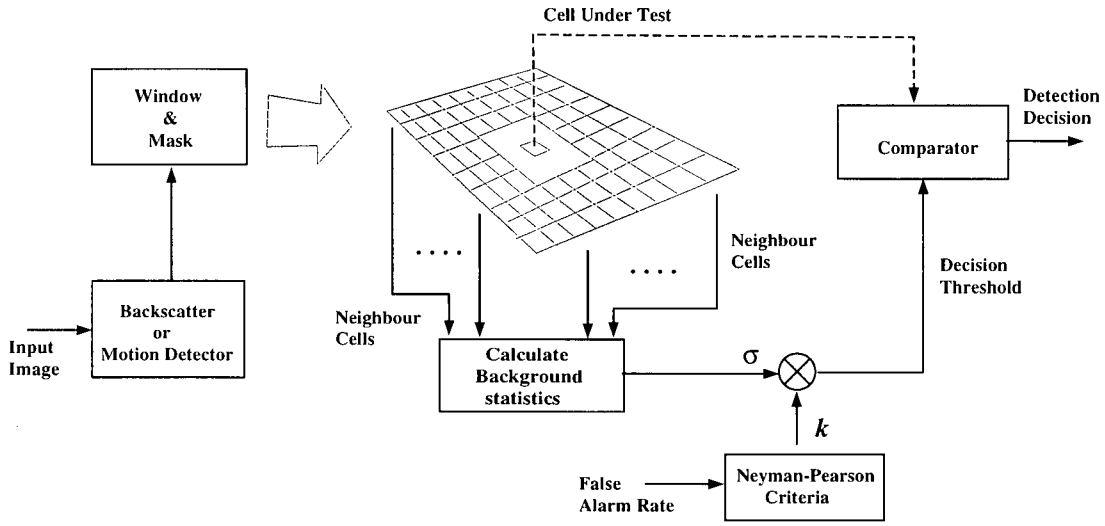

Figure 6.4 CA-CFAR Detector Functional Block Diagram

The detector outputs of the Backscatter and motion images can also be combined or fused to produce a third detector product, which, if we assume that clutter in Backscatter and clutter in motion have low correlation, could be considered as a clutter rejected target map.

The output of the detector applied to Chip #4 of Scene B, Chips #6 and #7 of Scene C, are shown at Appendix F. Figure A.1. shows the results of the detector's efforts to find the rocky island and shadow current in Chip #4. The data applied to the detector is cropped to exclude the feature-less background downstream of the current plume to reduce unnecessary computation. We can see that the detector was able to find only the rocky island from Backscatter, whereas it was able to find both island and current shadow from motion. The 'salt and pepper' like noise in the Backscatter detector output is the result of the detector mis-identifying clutter noise as feature. We suspect that the reason for the low clutter noise in the phase image is 1) there is very little differential surface current action in the scene, evidenced by the generally homogeneous appearance of the surrounding water in the phase image, and 2) the TBR of the highly differentiated current shadow feature is quite high with respect the relatively stationary background. A fusion of the detectors efforts to find targets in Backscatter and motion, was generated by applying a logical AND of the Backscatter and motion outputs to remove the 'salt and pepper' noise and isolate the

rocky island feature, then subtracting this from the motion output to isolate the current feature. This allows us to remove the effect of the strong return of the rocky island to isolate the current feature only.

Figure A.2. shows the results of the detector's efforts to find the wake of a small ship in a high clutter environment of Chip #6. We can see that the detector was able find the DTW in both Backscatter and motion, but that one Kelvin arm was only detected in motion. We can also see that a good deal of clutter was mis-identified as feature even though the false alarm rate was set quite low. Fusing the two outputs by applying a logical AND removed the clutter noise and resulted in a very clean, high probability detection of the ship's wake. In cases where the two outputs both show the target feature, fusing them by a logical AND essentially removes all residual clutter noise that remains after interferogram formation and the detection process, and which is uncorrelated between motion and Backscatter. However it should be noted that a logical AND is not a good practical fusion method in that it also removes the parts of the wake are effected by speckle in Backscatter which do not overlap in the phase image. This can be seen in the loss of the right Kelvin arm (in the lower edge of the motion images) in the fused detector output.

Figure A.3. shows the results of the detector's efforts to find the wake of 3 small ships, sailing in formation, in Chip 7. Chip 7 represents a near Nadir case, where radial direction of radar approaches vertical, with respect to the imaging platform (the aircraft). At near Nadir, the vertical component of scene motion dominates over horizontal motion and our estimate of horizontal surface velocity begins to deterio-rate. Specifically, the up and down motion (orbital and swell components of wave action) dominates the clutter in the scene and the up and down heaving motion of the target ship and wake dominates the target's motion signature. We can see that, in this case, the detector has great difficulty finding the wakes and mis-identifies a good deal of the dominating clutter. The Backscatter output is only marginally better, and although the wakes are quite distinct, a good deal of the background clutter is also (incorrectly) detected. However, fusing the two outputs using a logical AND removes much of the uncorrelated clutter and results in a relatively good indication of the wakes.

The performance of the simple CA-CFAR detector on the sample ATI interferograms would appear to indicate:

1. that the detectability of ship, wake and other ocean features by their motion signature is somewhat better than their detection by their Backscatter signature;
2. that in certain situations, such as in relatively flat featureless scenes or where surface manifestations of strong subsurface features is weak, features are detectable only in phase; and

3. that in certain situations where there is little or no motion, features with strong corner-reflector like surfaces are detectable better or only in magnitude;
4. that the fusing of motion and Backscatter detected outputs is highly effective in removing uncorrelated clutter noise.

Chapter 7 Conclusions

7.1 Summary

The objective of this thesis has been the investigation of the Along-Track Interferometry technique applied to Synthetic Aperture Radar for the purpose of enhancing ship wake detection. Specifically we determined that a) airborne C-band SAR ATI is capable of estimating differential (radial) velocity with sufficient accuracy to detect appreciable disturbances of the velocity field of the ocean, and b) that ship wakes, under the conditions of the data collected, were able to sufficiently disturb the velocity field of the ocean surface to be detected efficiently. Additionally, we assigned quantitative measures to the potential of the technique to enhance ship wake detection. The following is a summary of the work contained in the thesis:

The theory of SAR image formation, the Along-Track Interferometry technique, and theories of radar imaging of ocean features and ship wakes were reviewed. The magnitude of ATI interferograms was shown to be essentially the intensity of the radar Backscatter, but with improved noise rejection properties, and the phase of the interferogram was shown to be a precise estimator of radial velocity (in addition to it being a precise estimator of Doppler frequency as shown by Thompson & Jensen) and with superior phase noise and clutter rejection properties. Using the CCRS C-band SAR ATI as an example, the theoretical precision of velocity estimation was determined to be on the order of 0.11 m/s (0.21knots) or better than 1% of the unambiguous velocity range of the sensor; which was found to be within the necessary precision to image and detect ship wakes of moderate sized ships and other generally slowly varying wave structures.

Data from the experimental CCRS C-band SAR ATI was examined in detail, and as data representative of ATI sensors in general, it was found to have a high degree of inherent correlation (i.e. the lower bound of coherence for the data), with an average Coherence Magnitude of 0.87 and a probable value of 0.90. The misregistration between forward and aft images in the data set was verified as being limited to linear translation in the azimuth direction and the a priori estimated misregistration was verified to within 1/100 pixel accuracy as a 1.11 pixel or a 0.23m shift. Corrective shifting by a Cubic Spline interpolator to a precision of 1/10 pixel was determined to be sufficient to properly coregister this data type with minimal phase distortion.

Azimuth re-alignment was examined briefly as a means of correcting azimuth defocusing in SAR

images of dynamic ocean scenes and was found to be an effective alternative to computationally intensive Azimuth Refocusing in improving the frequency distribution and visual presentation quality of interferograms that show evidence of azimuth defocusing.

The signal and detection statistics of ships and wake targets and significant wave features in representative Backscatter (magnitude) and motion (phase) images of ATI interferograms was examined and compared with their spatial profiles and visual presentation (i.e. visual detectability). The interferometric phase or motion representation of ship wakes and wave features was observed to be better than that of their Backscatter, with TBR improvement in phase over magnitude of between 2dB to 13dB (with greater TBR values for fast moving features and large scale features with distinct velocity differences from their background) and typical detectability improvements of between 50% to 80% (and between 200% and 600% in exceptional cases of very distinct features). Additionally, we observed in circumstances where features are not visible in interferometric magnitude because of lack of Backscatter contrast, that the feature can be visible by interferometric phase so long as it has a velocity differential of as little as 0.89 knots. We also observed that the width and length of the motion signature of features tend to be greater than their Backscatter signature, as expected. These observations together appear to indicate that the interferometric phase representation of ocean scenes is somewhat better than the magnitude representation for detection of ship wakes and subtle wave features.

However, the contrast of most features was observed to be better in magnitude than in phase; with contrast values 20 times brighter for land features and as much as 60 times brighter for stationary corner reflector-like features such as ship's superstructures and hulls. And Backscatter signatures of features appeared to be less affected by azimuth defocusing than motion signatures. This, in addition to the generally higher contrast and the observed broader (Rayleigh) distribution of pixels, would appear to indicate that the magnitude representation of ocean scenes is better than the phase representation for visual presentation of fine grained background details and bright relatively stationary objects.

The detection performance of a representative adaptive target detector, a simple CA-CFAR detector, on the motion and Backscatter signatures of ships, wakes and wave features in the scene was examined. The detection by motion of ship wakes and subtle wave features in typical ocean clutter and the detection by Backscatter were found to be quite similar, even though the mechanisms (Backscatter versus motion) of detection are quite dissimilar; with the detector having only slightly better success with motion in flat (low surface activity) scenes and faster varying features and slightly better success with Backscatter in high Nadir. But because the detection methods are dissimilar, a fusion of the detector's motion target

map and Backscatter target map was found to be quite effective in eliminating the (motion/Backscatter) uncorrelated clutter and improving the overall performance of the SAR sensor in detecting ship wakes.

Thus it can be concluded, by analysis and demonstration, that Along-Track Interferometry is capable of enhancing the detection of ship wake by Synthetic Aperture Radars.

7.2 Further Work

SAR imagery of the dynamic ocean surface is often degraded by azimuth defocusing. The exact effect of this defocusing on the accuracy of velocity estimates is not well known and deserves some further study. Additionally, it may be possible that azimuth refocusing and azimuth coregistration of SLC images, and possibly other operations such as motion compensation and azimuth filtering, could be combined and accomplished in an optimized single operation.

This thesis has been concerned with airborne SAR ATI sensors. However, the ATI technique could be applied to spaceborne SAR, albeit the dual antenna configuration would be much more difficult to implement at spaceborne altitudes and velocities on a satellites limited structure. However, the enormous value to a maritime nation like Canada of such a spaceborne platform for wide area monitoring of shipping is such that it deserves some further study. As a start, the required operational parameters and theoretical precision of a notional spaceborne C-band SAR ATI were briefly examined n the course of the work of this thesis and the results reported to DREO.

And finally, although the application of a CA-CFAR target detector to the ATI data set and subsequent fusion of the data demonstrated the potential of ATI in enhancing SAR ship wake detection, the detector used represented only a simple example of numerous more capable and advanced detector schemes. And the simple Boolean data fusion techniques, though demonstrative of the value of fusing Backscatter and motion, are severely limited and other fusion techniques would yield much improved results. The utility and effect of the improved Backscatter information and the additional unique motion information provided by ATI in more advanced detectors and better fusion schemes should be further investigated.

Appendix A. SAR Imaging Mechanisms of Ship Wakes

Synthetic Aperture Radars image targets or scatterers and scenes by their modulation of the transmitted microwave energy. The reflected signal, called its Backscatter, is modulated by the dielectric properties, the shape and texture, and size of scatterers and the scene. The incidence angle of the radar and the local tilt angle of the scene also affects the amount of Backscatter energy received by the radar.

Over land scenes, the dielectric property of objects varies over a wide range due to the different chemical composition and moisture content of targets. Thus the dielectric property of targets and scenes, in addition to shape and size are important characteristics of the target or scene which the SAR is able to sense. And to a lesser degree, the local tilt angle and incidence angle of the radar also affect the Backscatter received by the antenna.

Sea water has a very low and relatively constant dielectric value. Over the ocean, radar does not penetrate the surface and is little modulated by dielectric properties. As a result, the Backscatter observed by a SAR of an ocean scene is primarily limited to the texture of the surface and the local tilt angle, and to a lesser degree, the incidence angle of the radar.

A.1 SAR Imaging of Ocean Waves

The four mechanisms by which radar, including SAR and SAR ATI, image waves on the ocean are:

1. Bragg scattering
2. Hydrodynamic modulation;
3. Tilt modulation; and
4. Velocity Bunching.

Bragg scattering is the predominant mechanism by which ocean waves are imaged. Bragg resonance is the interference of Backscattered microwave energy from short scale capillary and capillary-gravity waves that are on the order of a few millimeters to a few centimeters. These Capillary and capillary-gravity waves, which are primarily generated by wind action, effectively comprise the texture or surface roughness of the scene. The primary restoring force for these waves is surface tension; meaning that they are relatively short lived ocean structures. Between incidence angles of 20^0 and 60^0, Bragg waves dominate radar return, resulting in brightness in radar images. The greater the number of Bragg waves in a

region or scene, the brighter will be the region or scene in an image. Thus we can see that the brightness of an ocean scene is a function of the wind speed over the surface.

Hydrodynamic, tilt modulation and velocity bunching are essentially modulation mechanisms of Bragg resonant scattering. The physical processes of larger wave structures modulate the visible, but shorter Bragg waves by hydrodynamic and tilt modulation, which modulate amplitude, and by phase modulation due to orbital motion, which results in the velocity bunching effect [32].

Hydrodynamic Modulation: Longer waves on the surface of the ocean and internal waves travelling beneath the surface are visible to radar by their modulation of the shorter Bragg waves on the surface. This action is termed hydrodynamic modulation. An example of hydrodynamic modulation are turbulent wakes and internal waves, which damp surface capillary action resulting in dark regions on a light background.

Tilt Modulation: The incidence angle of the radar also determines the brightness of the scene. A high incidence angle results in nearly complete signal return from the surface, making the scene very bright. A low incidence angle results in mostly specular returns and a darker scene. The local tilt angle of the surface affects the amount of Backscatter similarly. However, unlike incidence angle which determines the constant brightness of the scene, the local tilt angle affects the local brightness, effectively modulating the general brightness of the scene, resulting in light and dark areas which are suggestive of the structure of the scene.

Velocity Bunching: Hydrodynamic and tilt modulation tend to be linear imaging mechanisms. Meaning that resolution scale and larger long waves modulate Bragg scatterers by hydrodynamic and tilt modulation consistent with a linear transfer function. Velocity bunching, on the other hand, is a nonlinear imaging mechanism because it results directly from the amplitude distortion due to the phase modulation of sub-resolution scattering elements, called facets. An example of this is the orbital motion of long waves which alternately concentrate and spread facets creating bands of light and dark regions.

SAR ATI images have been found to be sensitive to both linear Bragg scattering (i.e. hydrodynamic and tilt modulation) and velocity bunching. The velocity bunching mechanism is more dominant in azimuth travelling waves than in range travelling waves and increases with R/V (where R is nominal slant range and V is platform velocity) [32]. It is also believed that velocity bunching is a primary contributor to azimuth defocusing [25].

A.2 SAR Imaging of Ship and Wake Features

The wakes generated by Ships moving across the surface of the ocean propagate and are imaged in SAR the same way that natural ocean structures are imaged.

The presence of ships can be determined in standard and interferometric (ATI) SAR images by detecting the signature of the ship itself and/or by detecting its associated wake. In standard (non-interferometric) SAR ship detection schemes, the bright narrow return of the ship is usually easier to detect than the wake pattern. In general, the wake pattern is used to subsequently confirm or reject, as being a ship, an objected initially detected by its bright narrow feature. This is because detection in standard SAR images is by differential Backscatter or RCS contrast of the bright target against a background; which may itself be bright or noisy. Ships, which generally have corner reflector-like surfaces, give very strong radar returns. Wakes and wave structures, on the other hand, return much less radar energy in comparison to the ambient ocean and are therefore much less differentiated, by Backscatter, from their background. In standard SAR images, wake features are therefore difficult to detect and are rarely seen in comparison to bright ship features.

Ship wake features, although not very bright, are however generally much longer and wider than the narrow point-like signature of the ships and they are often quite differentiated from the ambient ocean by velocity. In theory, the larger detection mass of the wake as compared to the point target-like ship should make it easier to detect; so long as the wake is detectable. From satellites, the wake of ships are seen rarely in RCS and even from airborne, ship wakes are detected, in RCS, with less frequency than the ships themselves. Because ATI is both clutter rejecting and is able to detect the velocity of inherently temporal features (such as wakes), it would appear then to hold promise as a means of enhanced detection of ships using radar by means of their wake.

Ship wake features imaged in standard and interferometric SAR images include:

1. Turbulent wakes; and
2. Kelvin Wakes, which include Single or dual Kelvin arms and Stern wakes.

The relative location and orientation of these wake features with respect to a moving ship are illustrated below as Figure A.1.

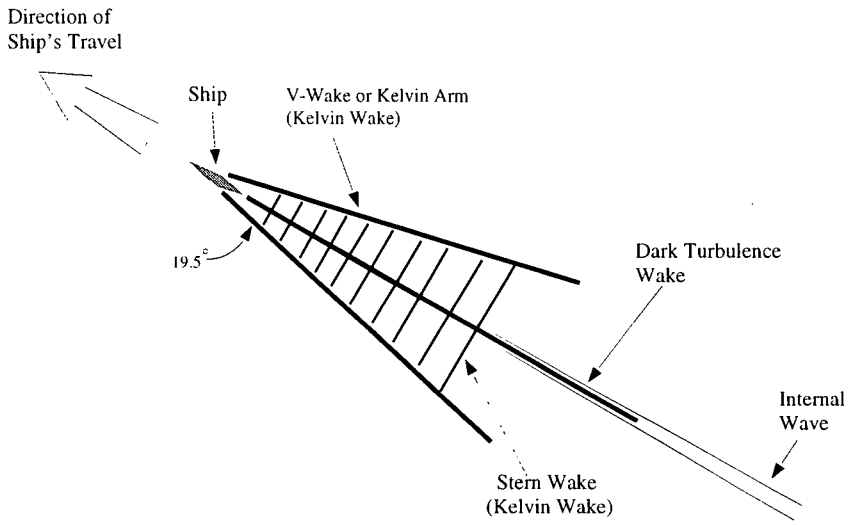

Figure A.1 Ship wake Features

Turbulent Wakes: Turbulent wakes are generated by the turbulent action of a ship's propulsion system and the displacement of water by the stern and keel of the vessel. Turbulent wakes consist of both a surface turbulence component and a subsurface travelling internal wave component.

The surface turbulence component is energetic, but short lived and does not propagate far. In calm seas, the surface disturbance component generates local surface roughness and may be visible to radar as a region of increased Backscatter or brighter intensity very close to the stern of a ship. In moderate to rough seas, the bright or surface disturbance component of a turbulent wake is difficult to differentiate from wind generated surface roughness. Surface turbulence is generally difficult to see in large scale standard SAR images.

The bulk of a turbulent wake's momentum, however, travels just beneath the surface of the water as an internal wave. It is for this reason that turbulent wakes are sometimes referred to as ship generated internal waves. The subsurface travelling turbulent wake also has a surface modulation component. In seas with moderate (wind generated) surface roughness and within the Kelvin wedge wake (see below) of a ship, where the sea surface roughness is generated by the ship, the modulated surface component damps surface capillary waves creating regions of dark intensity against the brighter background of the visible capillary waves. For this reason, the visible signature of a turbulent wake is often called a Dark Turbulent Wake (DTW). DTW are mostly visible within the Kelvin wake (i.e. the wedge of turbulence containing two Kelvin arms bounding stern wakes) where the ship generated surface roughness creates strong

background contrast for the DTW. Outside of the effect of the Kelvin wake, the non-damping internal wave component of the turbulent wake is imaged mostly via hydrodynamic interaction and is not as readily visible.

Because the internal wave portion of a turbulent wake mostly propagates beneath the surface of the water, it's persistence is little affected by the damping influence of surface tension. For this reason, turbulent wakes have the longest persistence and extent (or travel) of any wake features. The length or extent of the trailing DTW is largely a factor of the power generated by the ship's turning screws, the wind state, and sea state of the surrounding ocean. In SEASAT and ERS-1 images, DTW typically extend up to 3km behind the moving vessel. The visibility of DTW is largely determined by the relative orientation of the imaging radar. DTW are most visible when they are azimuth travelling with respect to the imaging radar. DTW can sometimes have bright edges on the wind side of the wake.

Turbulent wakes and specifically DTW are the most commonly viewed wake feature in standard spaceborne (non-interferometric) SAR images, accounting for roughly 80% of all ship wake features seen in non-interferometric (SEASAT and ERS-1) spaceborne SAR images.

Kelvin Wakes; Kelvin wakes are produced by the passage of the ship through the surface of the water. They are a surface wave pattern consisting of a V-shaped wake portion, sometimes called its Kelvin arms, and a series of ripple wakes, called stern wakes. The stern wakes are bounded by the Kelvin arms and travel rearwards from the ship.

The V-wake or arms of a Kelvin wake are produced by the slipstream or displacement of water as the bow of the moving vessel pushes its way through it. As the bow of the ship cuts into the water in front of it, it forces this water to travel around it in a slipstream. When the slipstream eventually breaks away from the hull of the ship, it creates the classic V pattern to either side of this ship. The V of the two Kelvin arms is a consistent half-angle of about 19.5 degrees for most vessels, regardless of its speed, size or displacement.

The presence of both arms of the Kelvin wake in a SAR image is a function of the surface wind direction and the viewing angle of the radar. Kelvin arms are most visible when aligned in the range direction with the wind blowing roughly perpendicular to it. In radar images, one or both Kelvin arms may be seen. Dual arm Kelvin wakes are seen only rarely. They account for less than 1% of all ship wake features seen in standard (SEASAT and ERS-1) spaceborne SAR images, while single arm Kelvin wakes are seen more frequently, accounting for roughly 10% of all ship wake features seen in standard (SEASAT

and ERS-1) spaceborne SAR images.

While the V-wake or Kelvin arms are the result of the water being displaced by the bow of the vessel, the stern or ripple wakes are the result of shock waves that form when the bow of the vessel collides with the viscous and resistant water. The shock waves interact with each other creating nulls and peaks which form the characteristic ripples of a stern wake. The period between ripples is a function of the ship's speed and displacement. Stern wakes travel rearwards from the stern of the moving vessel and are seen in standard SAR images as a series of dark and bright lines running perpendicular to the direction of the ship, bounded within the arms of the Kelvin wake. It is believed that the SAR imaging mechanism for ripple wakes is the rotation or modulation of Bragg acceptance angle by the curvatures of the corrugating ripples [33]. For this reason, stern wakes are more prominent when viewed propagating directly along the radial direction of the imaging radar.

Stern wakes are seen very rarely in standard SAR images and account for less than 1/2 of 1% of all ship wake features seen in non-interferometric (SEASAT and ERS-1) spaceborne SAR images.

Appendix B Feature Detection

In this report, we defined 'detection' as the determination of the presence of an expected target. The pure detection problem, as it usually applies to classical radar and communication system engineering, refers simply to the determination of the presence of a single signal or target. However, in the case of our work, to detect ship wake features, we will consider the detection problem to include the determination of the presence and location of a sufficiently large group of pixels to identify it as being a ship wake.

Detection can either be visual, normally by the eye of a trained human operator/interpreter, or automatic, normally by computer numeric analysis. The potential of a signal to portray successful detection of a feature is a function of a detector's ability to detect each pixel in an expected feature and a classifier's ability to identify a group of detected pixels as belonging to a specific feature. The performance of classifiers is beyond the scope of this present work, but we can consider that their probability of successfully identifying a feature is proportional to the number of detected pixels associated with it.

B.1 Visual Detection

The advantage of the human eye is that it is inherently averaging, flexible and adaptive. The eye of a trained human operator/interpreter is generally better suited to detecting fine detailed and faint features in heavy noise than a numerical computer system. Human based/assisted visual detection is also not bound by simple rule based detection, enabling a human operator to quickly detect subtle and complex patterns which may be cues to the presence of both expected and unexpected features. And unlike most current computer systems, a human operator is able to learn from experience. However, because, the human eye is non-linear and because it has a relatively narrow visible range, the human eye is generally only able to detect features that have considerable contrast from adjacent features. For this reason, most images have to be mapped and stretched into a visible colour scale, with sufficient delineation between adjacent signal levels, before they can be viewed visually for human based/assisted detection. Contrast stretching can, however both hide as well as enhance features, while false colour maps can be deceptive making visual detection inconsistent. Visual detection is best suited to final stage detection and classification of small image sets that have been initially extracted by automated detectors from larger image sets.

B.2 Automated Detection

Automated detection using computer numeric methods, on the other hand, does not normally

require any scaling or stretches. Because it is rule based, numeric detections, though limited by the scope and complexity of the rule, are nevertheless more consistent than visual detections. Depending on the rule base, numeric detection schemes are able to exploit the statistics of the expected feature and distinguish very small differences between signals to identify a feature.

However, in order to do so, the background noise must be made small in comparison to the feature's signal strength. Automated detection systems therefore need effective pre-filtering in order to perform optimally. Additionally, because automated detectors are generally rule specific, they are non-adaptive and will only be able to detect expected features based on a narrow, rigid, predefined criteria set. We note that the dynamic range of the radar (and its processed numerical representations) must be adequate to cover the brightness range of targets and background clutter for automated detection to work properly.

The strength of automated detection, however, is in their inherent speed and ability to exhaustively search a large image space or a large number of images quickly and consistently. Automated detection is best suited to preliminary stage detection and extraction of features in large image sets for subsequent classification by human visual means.

B.2.1 Numeric Detection Theory

Both visual and automatic detection are employed in ship wake detection using standard SAR images. In this work, we have considered computer numerical analysis to be the more interesting case because it is the easiest to quantify and have confined the bulk of our analysis to numeric methods.

The problem of numerical detection of features in radar imaged ocean scenes is fundamentally statistical because of the stochastic nature of the thermal noise process that affects active sensors, the fading effect of averaging multiple scatters in finite resolution cells, and the randomness of wind / wave motions that dominate the ocean surface.

The two principle metrics by which detection decisions are made are effective Target to Background Ratio (TBR) and effective signal distance (contrast) [26]. In a simple one dimensional signal system with Gaussian noise statistics, signal distance, S, and TBR can be defined as follows:

$$S = \mu_0 - \mu_1 \tag{2.1}$$

$$TBR = \frac{\mu_0 - \mu_1}{\sigma_0 + \sigma_1} \tag{2.2}$$

where μ_0 is the mean signal strength of a nil detection and μ_1 is the mean signal strength of a positive detection and σ_0 is the standard deviation of background noise and σ_1 is the standard deviation of a positive detection. This can be illustrated graphically in Figure 2.1 below:

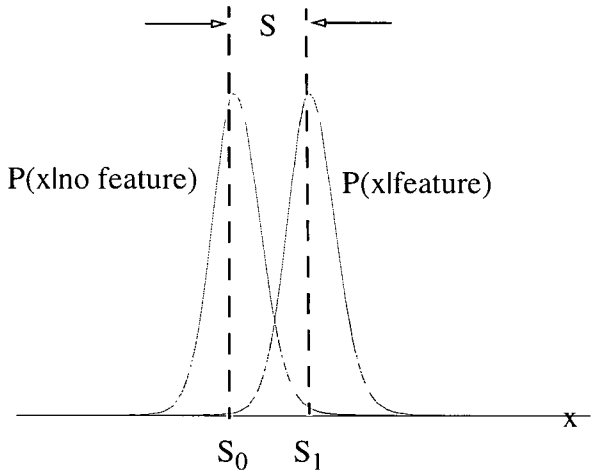

Figure 2.1 Simple Gaussian signal system

In theory, thermal noise is both zero mean and Gaussian, in which case μ_0 is 0 and the effective signal distance, S, is simply effective signal strength. However, in practical detection cases, the signal under test is often affected by a DC bias which has its source in the front end receiver and pre-detection stages. In the illustration above, a nonzero value of μ_0, can be assumed to be a DC bias, which is compensated in the detector.

In conventional radar, detection is usually real-time and the signal under test, which contains targets embedded in noise, is assumed to be in stream form; the independent quantity being time. The distribution of both noise and signal is a distribution over time and the detection process is considered to be based on both a time averaging and an ensemble averaging over the sweep coordinate of the radar. Detection is usually done 'on the fly' as the signal is being received.

In SAR images, which are inherently 2-D, the signal under test is in two dimensional form with independent quantities being azimuth and range coordinates. The distribution of noise and signal is a

spatial distribution and the detection process, is therefore, considered to be based on a spatial averaging over azimuth and (slant) range. Detection in SAR images is usually done 'off-line' after the image has been processed. The same statistical detection theories which are effective in conventional radar detection also lend themselves to effective detection in SAR images.

B.2.2 Detectors

For the purpose of our analysis and future work, we will divide detectors into two common classes:

1. Non-adaptive; and
2. Adaptive.

Non-adaptive detectors assume invariant system parameters and the detection threshold is set *a priori* to a constant value based on the assumed stable noise statistics. Common non-adaptive detectors include simple Bayesian, Maximum Likelihood (ML), and Maximum-a-Priori (MAP) detectors. The most commonly used non-adaptive detector in radar applications is the Maximum Likelihood (ML) detector.

Adaptive detectors, on the other hand, have the capability of varying detection threshold levels in response to changing system parameters, such as receiver or background noise or previously detected values. Adaptive detectors are capable of continuing to operate in varying noise conditions, such as such as electronic jamming, that would completely degrade non-adaptive detectors. Common adaptive detectors include Constant False Alarm Rate (CFAR) detectors. In conditions with known and stable noise levels, the probability of detection using adaptive detectors is, however, reduced in comparison to the probability of detection using non-adaptive techniques.

B.2.3 Detection Threshold

Both adaptive and non-adaptive detectors require a statistical rule base by which to determine a detection threshold. In some literature, this rule base is called a likelihood ratio test. Rule bases are usually determined from measured or assumed statistical distributions of the background noise in the signal or image under test. The detection threshold is the minimum signal strength (i.e. the minimum signal level above the ambient background) required for successful detection of a feature.

Two common statistical rule bases used to determine detection threshold are the:

1. Maximum Likelihood criteria; and
2. Neyman-Pearson criteria.

The Maximum Likelihood (ML) detector is one of the simplest and most common detection schemes in communications and radar processing. The ML detector assumes a known and stable noise level and is designed to:

1. minimize the probability that a detection is declared when no target exists (called the probability of false alarm P_{fa}); and
2. minimize the probability that no detection is declared when a target does exist (called the 'false dismissal' probability $1-P_d$);

A threshold is determined which equalizes the false alarm rate and probability of detection $P_{fa}=P_d$.

In many cases, however, the cost of false alarms is unknown; particularly in the case of signals in an environment of severe and varying noise. In this case, an acceptable cost level must be set before determining a detection threshold. The Neyman-Pearson criteria uses a predefined acceptable rate of false alarms P_{fa}, to determine a threshold which maximizes detection, P_d.

The mechanics of the ML and Neyman-Pearson detection criteria are illustrated below using a Gaussian noise channel to model the noise process in our signal or image under test. The ideal Gaussian channel, in which the dominant noise source process is modeled as Additive White Gaussian (AWG), is a common signal model used in radar processing as well as communications processing. It is also, interestingly enough, the model used for ambient ocean noise. Analysis of the key distributions of polarimetric and interferometric SAR data under Gaussian and multi-variate K distribution models has shown that although the Gaussian channel is not appropriate for analyzing magnitude information, which is multi-variate K distributed, it is appropriate for phase [23]. Additionally, we have shown by simple analysis that receiver phase noise is reduced in the interferogram formation process, reducing the product model for the noise distribution to just a single factor in phase; scene clutter, which is Gaussian. This was also verified by observation in the CCRS C-Band ATI data. For these reasons, the Gaussian noise channel is considered completely adequate for detection of targets in phase and ideally for our problem, the detection of radar imaged ship features in ambient ocean noise.

In the ideal AWG channel, the decision threshold for the Maximum Likelihood (ML) detector is [34]:

$$X > \frac{S}{2} + \frac{\sigma^2}{S}\log\eta \tag{2.3}$$

where η is a Lagrange multiplier, which we call the probability ratio, and represents the minimum limit of the probability of a feature being present and no feature being present:

$$\eta < \frac{\text{P(X | feature)}}{\text{P(X | no feature)}} \tag{2.4}$$

In AWG channels, the probability distribution of a feature and that of no feature being present are equal and the probability ratio, η, reduces to 1. The detection criteria for the AWG case thus reduces to:

$$X > \frac{S}{2} \tag{2.5}$$

The detection probability and false alarm probability of the ML detector in AWG noise are:

$$P_d = \frac{1}{2}\left[1 + \text{erf}\left(\frac{S}{2\sigma\sqrt{2}}\right)\right] \tag{2.6}$$

$$P_{fa} = \frac{1}{2}\left[1 - \text{erf}\left(\frac{S}{2\sigma\sqrt{2}}\right)\right] \tag{2.7}$$

where erf() is the Gaussian error function. Note that the ML detection threshold (2.5) is half the signal distance between an expected target and its background. Also note that the shape of the noise distribution (i.e. variance) is not explicitly incorporated in the detection threshold. ML detection uses only the contrast between target and background to determine its presence. We note that the ratio, S/σ, is the TBR.

In contrast, the Neyman-Pearson detection scheme, does not make any implicit assumptions about the noise statistics. The probability distributions of a feature being present and not present are not assumed equal and therefore the probability ratio, η, is not unitary. Additionally, in a CFAR detector where the noise statistics are considered variable over time (or spatially), the detection threshold will not be constant either and will be varied to adapt to the changing noise.

The Neyman-Pearson criteria, unlike the ML detector which attempts to minimize both false detection and false nil-detection, attempts to achieve a constant false alarm rate. The decision threshold for the Neyman-Pearson detector is [34]:

$$X > \eta \tag{2.8}$$

where η is the solution to a false alarm probability, P_{fa}, equation in which the false alarm probability P_{fa} is determined a priori. For an AWG noise channel, the false alarm equation is:

$$P_{fa} = \frac{1}{2}\left[1 - \mathrm{erf}\left(\frac{\eta}{\sigma\sqrt{2}}\right)\right] \tag{2.9}$$

The solution to the false alarm equation for η is usually a constant, k, times the standard deviation of the noise distribution:

$$\eta = k \cdot \sigma \tag{2.10}$$

It is important to note that the Neyman-Pearson detection criteria is based exclusively on the shape of the background noise distribution. The probability of detection of a Gaussian signal under the Neyman-Pearson detection scheme is:

$$P_d = \frac{1}{2}\left[1 + \mathrm{erf}\left(\frac{S}{\sigma\sqrt{s}} - \frac{\eta}{\sigma\sqrt{2}}\right)\right] \tag{2.11}$$

The Neyman-Pearson detection criteria is often used by adaptive CFAR detectors.

Appendix C. Catalogue of Data Sets (Scenes)

This appendix details a catalogue and description of the three data sets or scenes used in this report. They are:

Name	Catalog #	Description	Size
Scene A	June 23 Line 4 Pass 2	Continental Shelf off coast of Nova Scotia	5968 (Az) x 2048 (Rng) pixels 24 km (Az) x 8 km (Rng)
Scene B	June 23 Line 8 Pass 3	Continental Shelf off coast of Nova Scotia	2894 (Az) x 2048 (Rng) pixel 12 km (Az) x 8 km (Rng)
Scene C	August 21 Line 16 Pass 7	Active Pass & Strait of Georgia off coast of BC	2804 (Az) x 2048 (Rng) pixels 11 km (Az) x 8.2 km (Rng)

C.1 Visual Catalogue

Only the phase images of the interferograms, labelled Figure 3.1, Figure 3.2, and Figure 3.3 are shown as representative of the three scenes. In these figures, the azimuth and range orientations are shown as arrows in each figure, with the vertex of the two arrows designating nearest range and lowest azimuth line. The radar is starboard (right) looking and in each image the aircraft is travelling in the direction of increasing azimuth. Each image is aspect ratio correct (1:1) with the dimensions of the resolution cell in each being 4m x 4m in slant range/azimuth coordinates. Note that a linear contrast stretch was applied to each image in order to centre the mean signal level of each distribution before mapping the values of each pixel into grey scale values from 0:255. The mean signal level in the scene of each image is represented as grey level 128 in the middle of the grey scale. In calibrated phase images, this would correspond to zero velocity. This type of stretching was selected in order to give the best visual contrast of the main features in the scene. The velocity ambiguity is +/- 7.1 m/s which corresponds to +/- 2π. No pixel values exceeded these values although we suspect that the phase value of ship targets are wrapped.

C.2 Format

Scene A was initially received in Oct 95 as an unregistered SLC from CCRS and later in Mar 96 as a registered azimuth re-aligned and subsampled interferogram. In Oct 95, the unregistered SLC image pair of Scene A was used to investigate the ATI interferogram formation process; specifically coherence and the effect of coregistration techniques, described in Chapter 3. For the signal information and detection performance investigation of Chapter 4 and 6, we coregistered the SLC image pair of Scene A, using a

Cubic Spline Interpolation filter, formed the pair into an interferogram, and subsampled it to an aspect ratio of 1:1 and a 4m/pixel range x 4m/pixel azimuth resolution using an FIR decimation filter to portray a final image with an aspect ratio of 1:1. Scene B and C were received in single image interferogram form from CCRS by FTP on 18 Mar 96. These images had been focussed, coregistered, using a Cubic Spline Interpolator, formed into interferograms, subsampled to an aspect ratio of 1:1 and a 4m/pixel range x 4m/pixel azimuth resolution, and azimuth resampled (re-aligned) by CCRS before being sent to us. Azimuth realignment, using a calibration scene, was necessary to reduce the smearing effects due to random wave motions; also called azimuth defocusing.

All data sets were received in single precision complex MATLAB[1] file format which were converted into unformatted magnitude and phase floating point files before being read into the IDL/ENVI[2] environment for visualization and analysis. All analysis was done in the IDL/ENVI environment.

[1] MATLAB 4.2c is a trademark of the Mathworks, Inc.

[2] IDL and ENVI are trademarks of Research Systems, Inc.

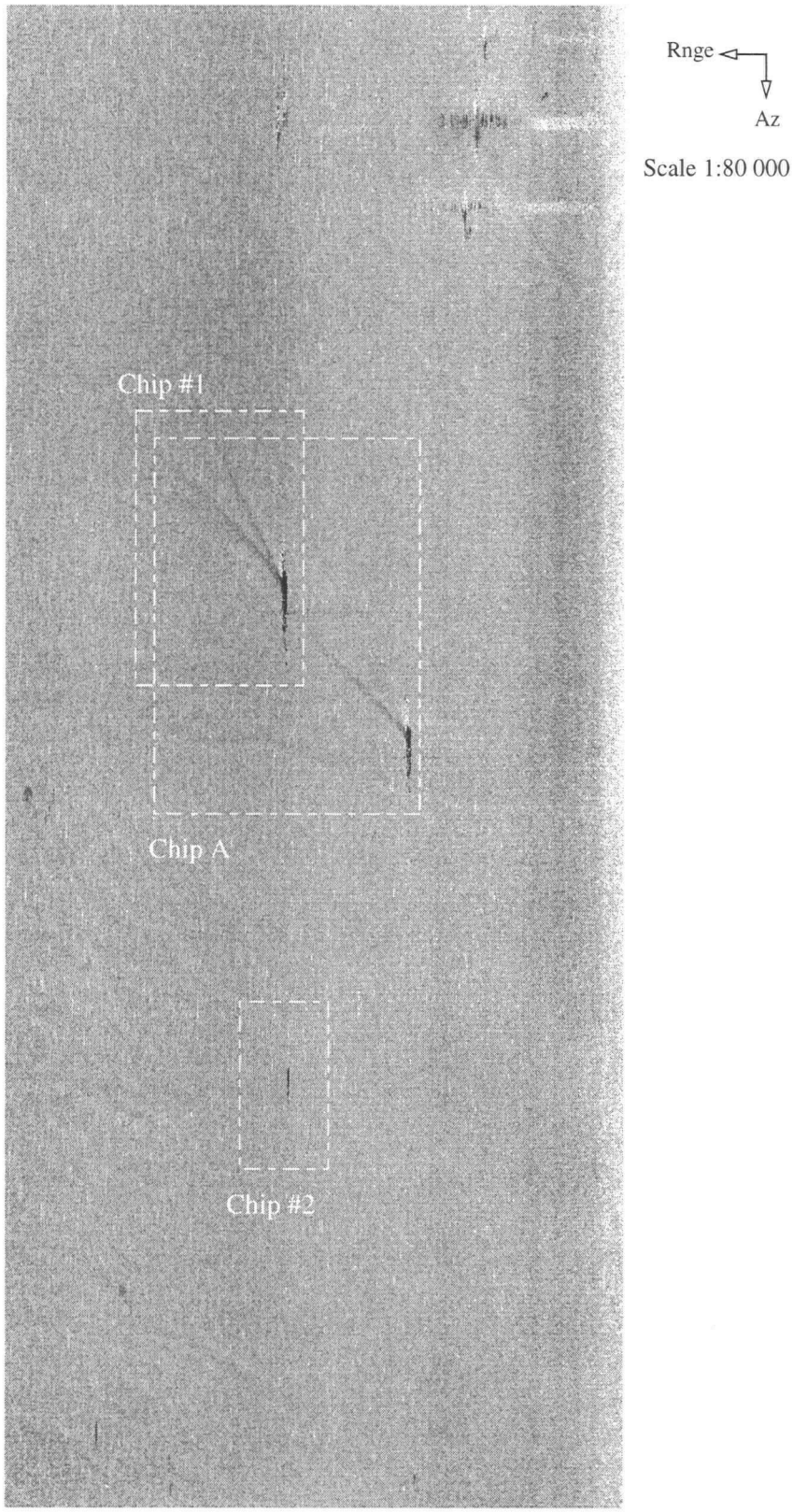

Figure 3.1 Phase image of Scene A: June 23, Line 4, Pass 2. ships off coast of Nova Scotia

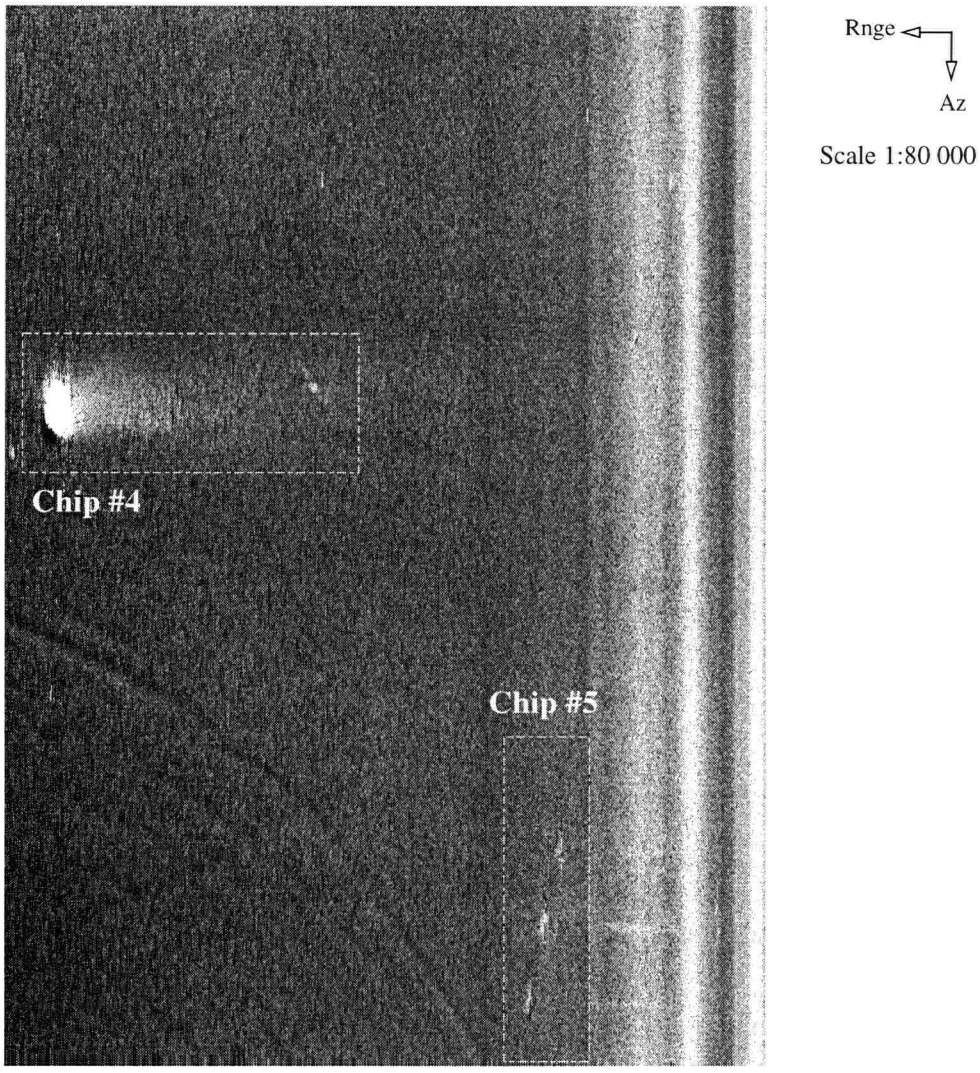

Figure 3.2 Phase Image of Scene B: June 23, Line 8, Pass 3. small ships and rocky island off the coast of Nova Scotia

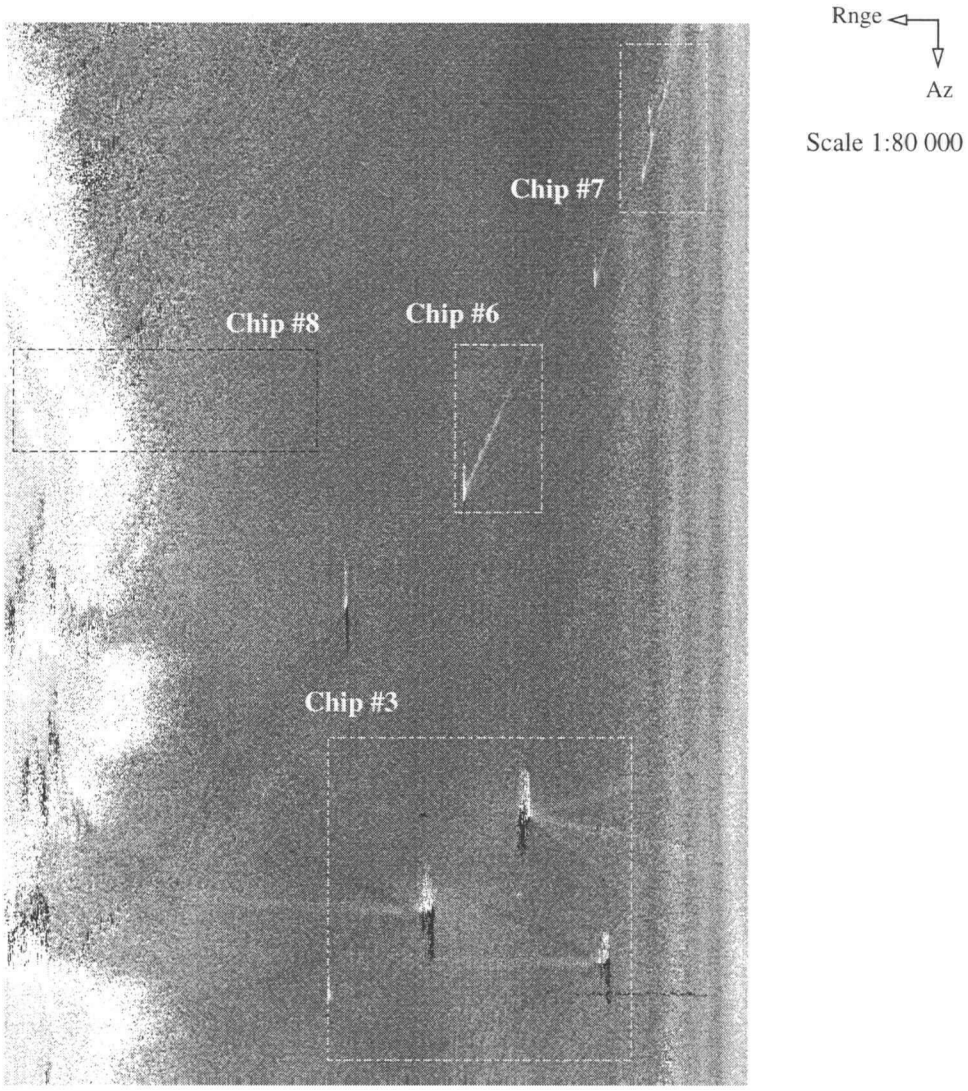

Figure 3.3 Phase Image of Scene C: August 21, Line 16, Pass 7, ships off coast of BC

Appendix D Filtered and Unfiltered Chip Images

Figure 4.1 and Figure 4.2 show the phase and Backscatter signature of a single arm wake of an unidentified fast moving craft in Chip #2.

Figure 4.3 and Figure 4.4 show the (radial) velocity and Backscatter signature of three passenger ferries traversing Active Pass on British Columbia's west coast.

Figure 4.5 and Figure 4.6 show a bright feature (possibly a small rocky island) and a current shadow feature behind it in Chip #4.

Figure 4.7 and Figure 4.8 show the velocity and Backscatter signature of three small slow moving vessels with no visible wakes in Chip #5.

In each image, range is in the vertical direction with near range towards the top. Azimuth is in the horizontal direction with azimuth line number increasing towards the right.

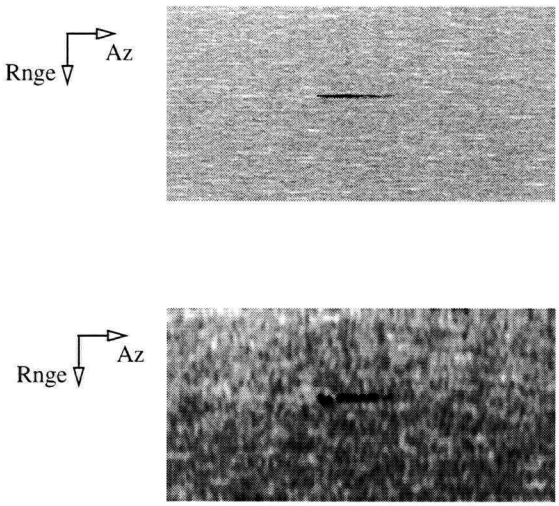

Figure 4.1 Phase Image Chip #2 Scene A. Single arm wake of unknown fast craft

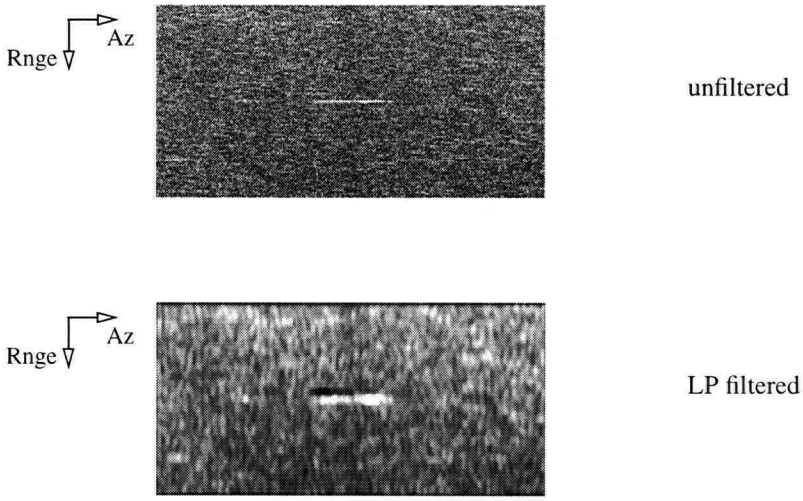

Figure 4.2 Backscatter Intensity Image Chip #2 Scene A. Single arm wake of unknown fast craft

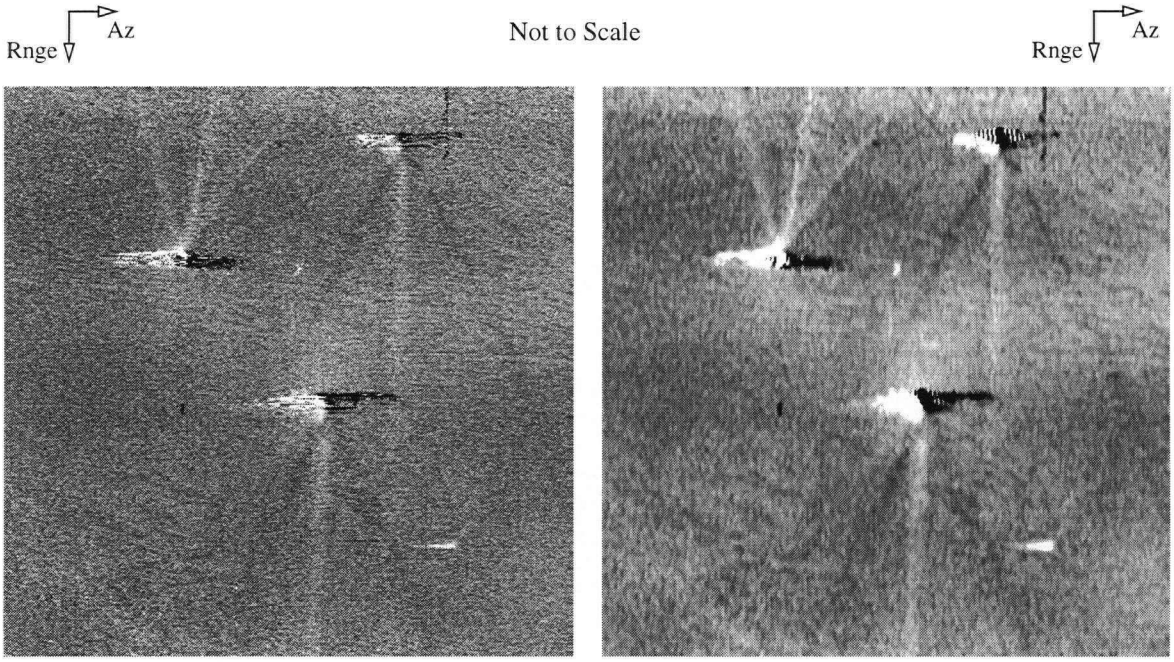

unfiltered LP filtered

Figure 4.3 Phase Image of Chip #3 Scene C, 3 coast ferries, with DTW and Kelvin wakes.

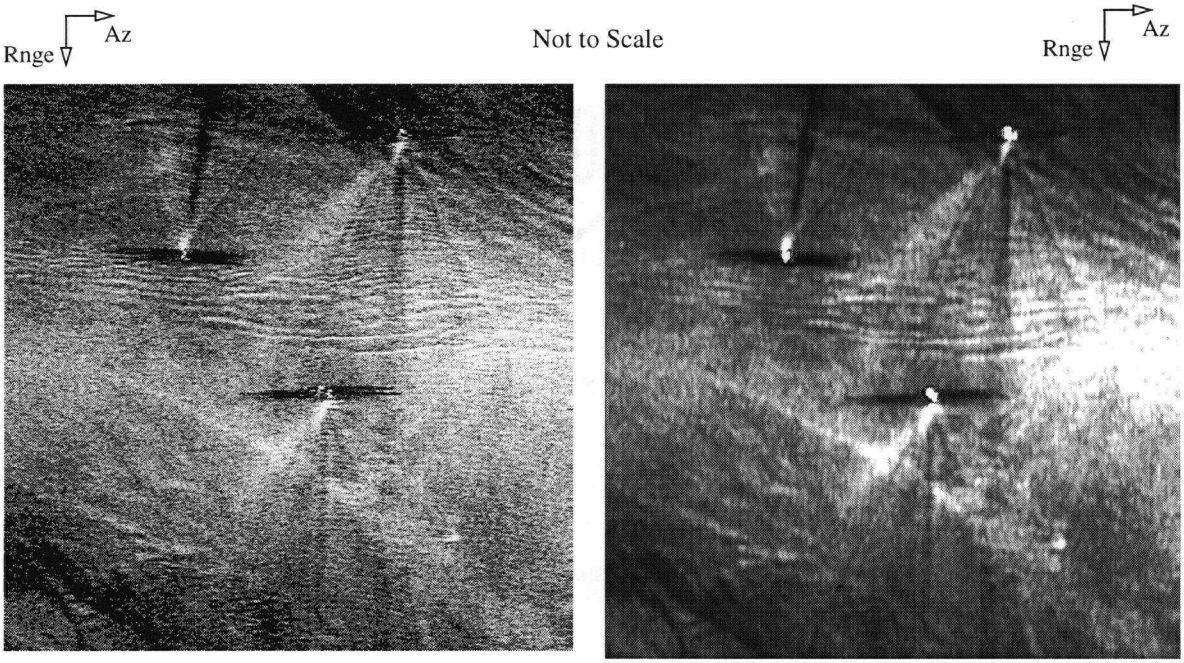

unfiltered LP filtered

Figure 4.4 Backscatter Intensity Image of Chip #3 Scene C. 3 coastal ferries, with DTW and Kelvin wakes

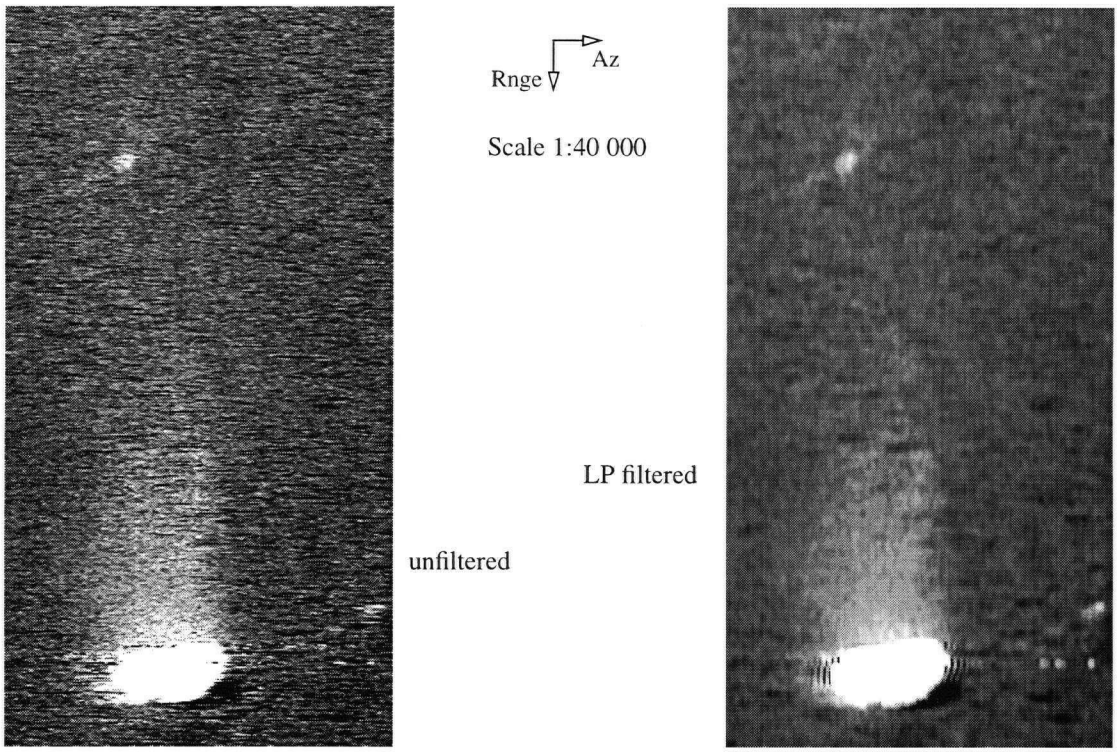

Figure 4.5 Phase Image of Chip #4 Scene B. Land feature and shadow current

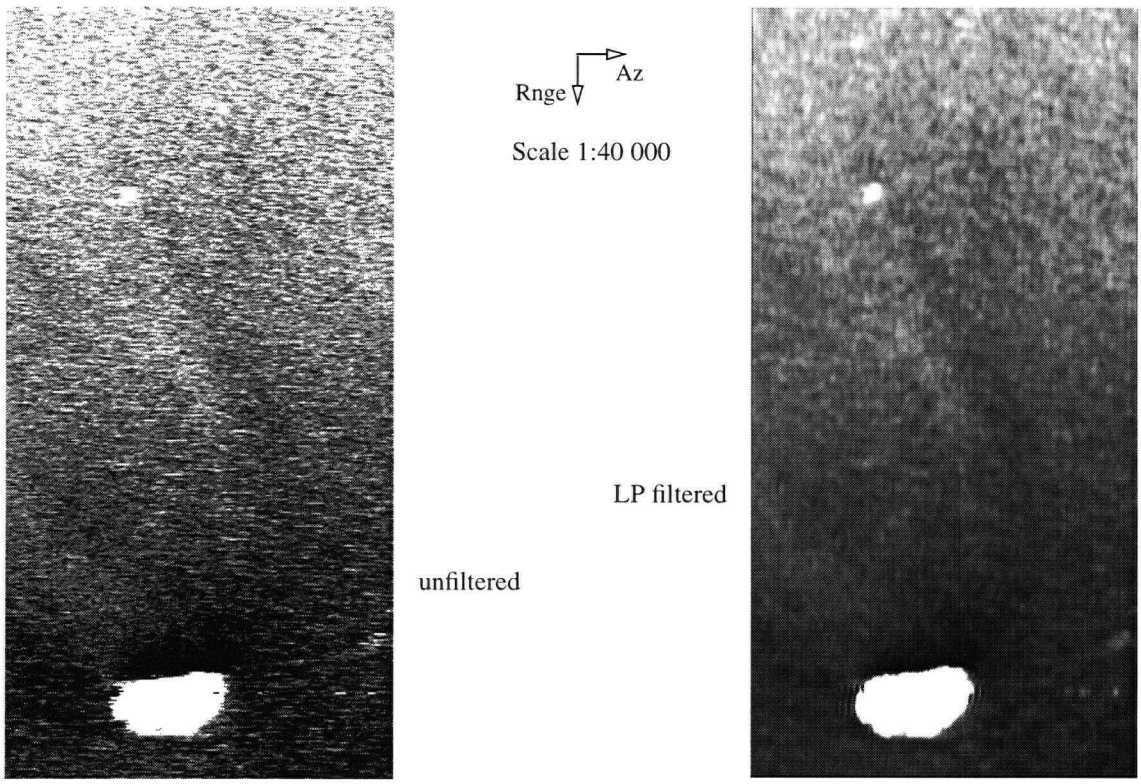

Figure 4.6 Backscatter Intensity Image of Chip #4 Scene B. Land feature and shadow current

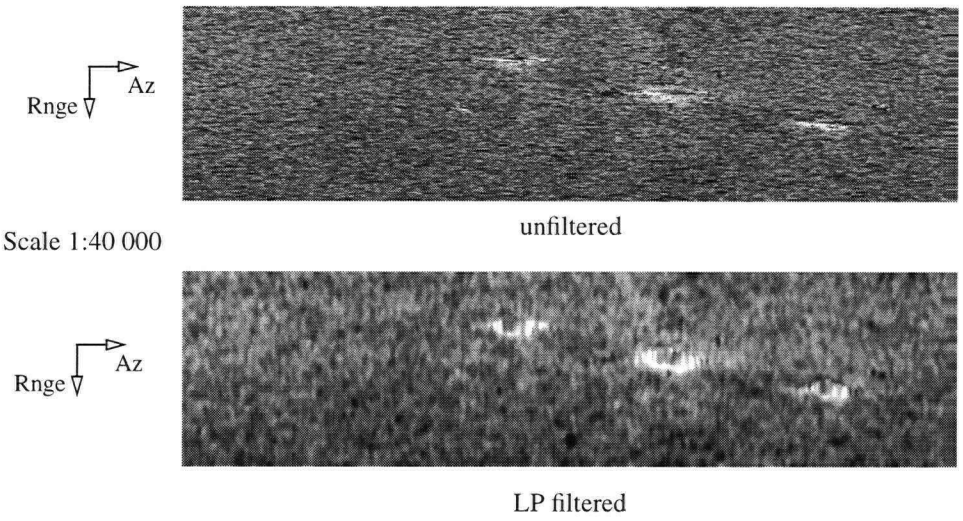

Figure 4.7 Phase image of Chip #5 Scene B, 3 small ships with little or no apparent wakes

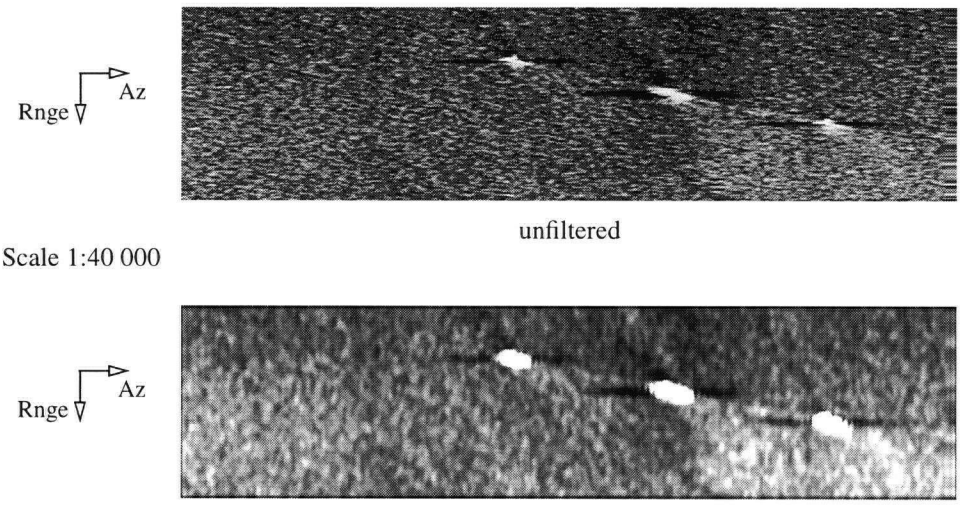

Figure 4.8 Backscatter Intensity image of Chip #5 Scene B, 3 small ships with little or no apparent wakes

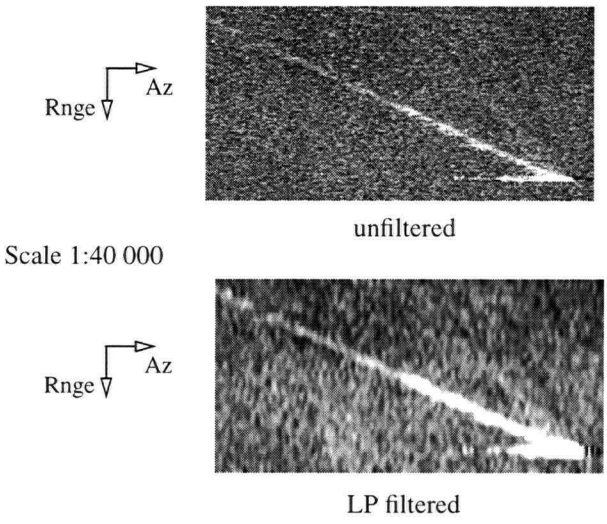

Figure 4.9 Phase image of Chip #6 Scene C, very long linear wake feature

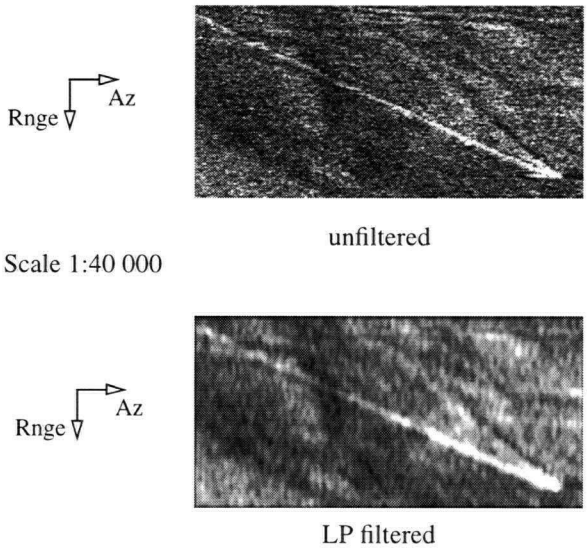

Figure 4.10 Backscatter Intensity image of Chip #6 Scene C, very long linear wake feature

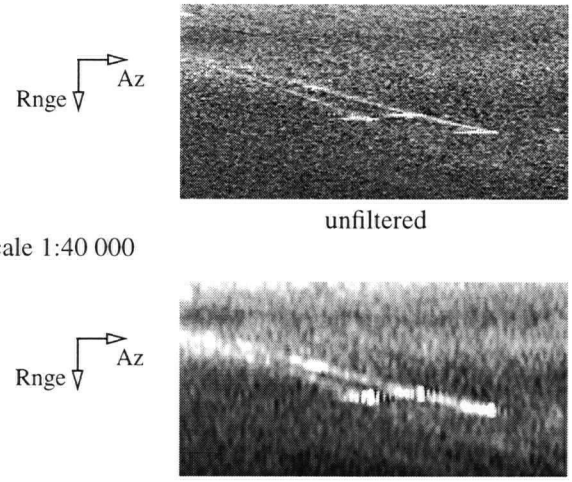

Figure 4.11 Phase image of Chip #7 Scene C, 3 small ships and associated linear wakes

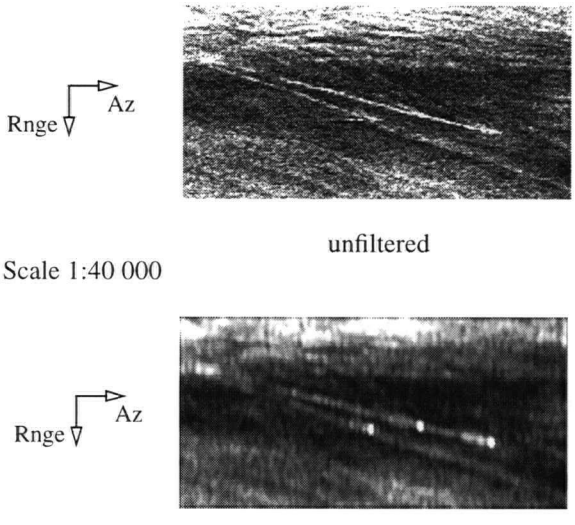

Figure 4.12 Backscatter Intensity image of Chip #7 Scene C, 3 small ships and associated linear wakes

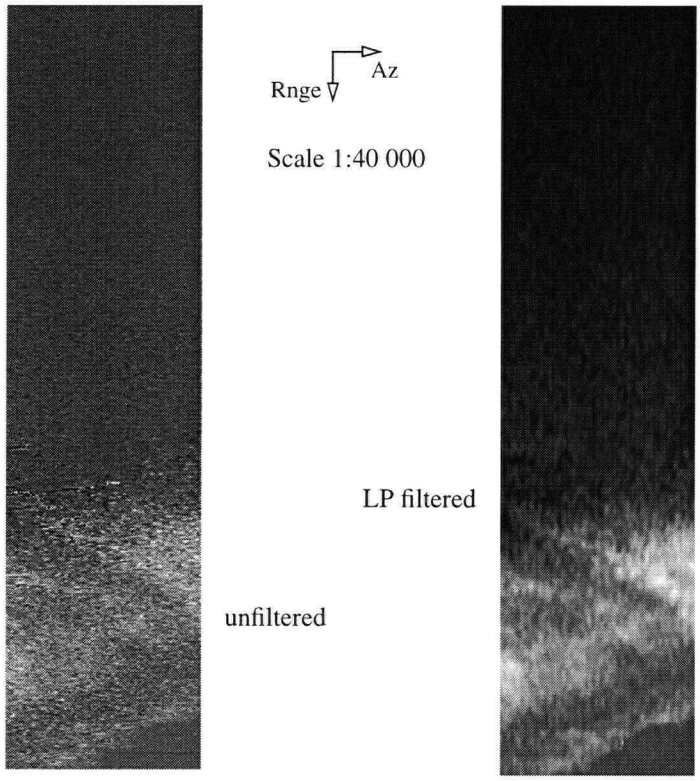

Figure 4.13 Phase Image of Chip #8 Scene C, land and tidal current

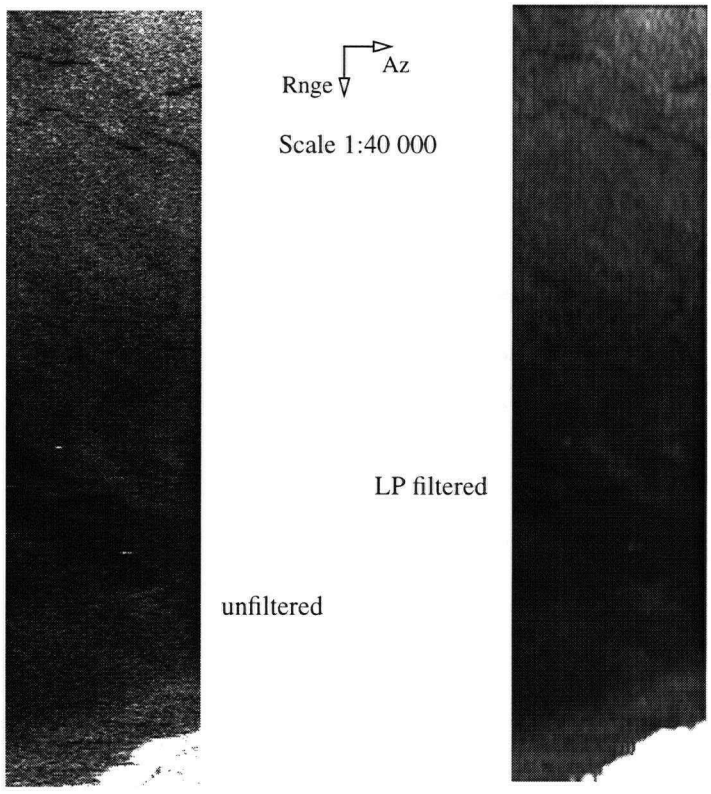

Figure 4.14 Backscatter Intensity Image of Chip #8 Chip C, land and tidal current

Appendix E. Signal and Statistics of Targets

ati_measurements3

Description	Signal Type	Image	Feature	mu feature	sigma feature	mu scene	mu vicinity	sigma vicinity	C_local	C_general	C_index	TCR	TSR SNR_dB	length	width	size (K)	P_det	Df P_det	Det NRG(K)
Original (unre-aligned)	phase	Chip #1	ship	-1.35	2.17	-2.52	-2.56	0.11	0.47	0.46	0.47	0.53	-2.8 dB	1060	80	86	0.60	60 %	52
Original (unre-aligned)	phase	Chip #1	DTW	-2.63	0.13	-2.52	-2.56	0.11	0.03	0.04	0.04	0.29	-5.4 dB	2160	64	138	0.56	6 %	77
Original (unre-aligned)	phase	Chip #1	Dark Kelvin Arm	-2.63	0.11	-2.52	-2.56	0.11	0.03	0.04	0.04	0.32	-5.0 dB	2160	60	130	0.56	6 %	73
Original (unre-aligned)	phase	Chip #1	Brt Kelvin Arm	-2.53	0.11	-2.52	-2.56	0.11	0.012	0.00	0.01	0.14	-8.7 dB	1800	48	86	0.53	3 %	46
Re-aligned	phase	Chip #1	ship	0.58	1.33	1.01	0.91	0.18	0.36	0.43	0.41	0.22	-6.6 dB	720	64	46	0.54	4 %	25
Re-aligned	phase	Chip #1	DTW	0.71	0.22	1.01	0.91	0.18	0.22	0.30	0.27	0.50	-3.0 dB	2120	68	144	0.60	10 %	86
Re-aligned	phase	Chip #1	Dark Kelvin Arm	0.69	0.24	1.01	0.91	0.18	0.24	0.32	0.29	0.52	-2.8 dB	2000	48	96	0.60	10 %	58
Re-aligned	phase	Chip #1	Brt Kelvin Arm	0.98	0.17	1.01	0.91	0.18	0.08	0.03	0.04	0.20	-7.0 dB	1800	48	86	0.54	4 %	47
Unfiltered	phase	Chip #1	ship	0.58	1.33	1.01	0.91	0.18	0.36	0.43	0.41	0.22	-6.6 dB	720	64	46	0.54	4 %	25
Unfiltered	phase	Chip #1	DTW	0.71	0.22	1.01	0.91	0.18	0.22	0.30	0.27	0.50	-3.0 dB	2120	68	144	0.60	10 %	86
Unfiltered	phase	Chip #1	Dark Kelvin Arm	0.69	0.24	1.01	0.91	0.18	0.24	0.32	0.29	0.52	-2.8 dB	2000	48	96	0.60	10 %	58
Unfiltered	phase	Chip #1	Brt Kelvin Arm	0.88	0.17	1.01	0.91	0.18	0.03	0.13	0.10	0.09	-10.7 dB	1800	48	86	0.52	2 %	45
Unfiltered	phase	Chip #3	ship	0.62	1.5	-0.36	-0.35	0.07	2.77	2.72	2.74	0.62	-2.1 dB	500	120	60	0.62	12 %	37
Unfiltered	phase	Chip #3	Kelvin Arms	-0.4	0.07	-0.36	-0.35	0.07	0.14	0.11	0.12	0.35	-4.6 dB	1120	32	36	0.57	7 %	20
Unfiltered	phase	Chip #3	Stern Wake	-0.37	0.21	-0.36	-0.35	0.07	0.06	0.03	0.04	0.07	-11.5 dB	n/a	20	n/a	0.51	1 %	n/a
Unfiltered	phase	Chip #3	DTW	-0.30	0.082	-0.36	-0.35	0.07	0.14	0.17	0.16	0.32	-4.9 dB	1720	140	241	0.56	6 %	136
2-D Filtered	phase	Chip #1	ship	0.10	0.59	1.00	0.91	0.082	0.89	0.90	0.90	1.21	0.8 dB	700	120	84	0.73	23 %	61
2-D Filtered	phase	Chip #1	DTW	0.71	0.14	1.00	0.91	0.082	0.22	0.29	0.27	0.90	-0.5 dB	2200	140	308	0.67	17 %	208
2-D Filtered	phase	Chip #1	Dark Kelvin Arm	0.71	0.14	1.00	0.91	0.082	0.22	0.29	0.27	0.90	-0.5 dB	2000	120	240	0.67	17 %	162
2-D Filtered	phase	Chip #1	Brt Kelvin Arm	0.98	0.07	1.00	0.91	0.082	0.08	0.02	0.04	0.46	-3.4 dB	2120	96	204	0.59	9 %	120
2-D Filtered	phase	Chip #3	ship	2.42	0.16	-0.36	-0.34	0.035	8.12	7.72	7.84	14.15	11.5 dB	480	120	58	1.00	50 %	58
2-D Filtered	phase	Chip #3	Kelvin Arms	-0.38	0.032	-0.36	-0.34	0.035	0.12	0.06	0.07	0.60	-2.2 dB	2200	96	211	0.62	12 %	130
2-D Filtered	phase	Chip #3	Stern Wake	n/a	n/a	-0.36	-0.34	0.035	n/a	n/a	n/a	n/a	n/a	n/a	n/a	n/a	n/a	n/a	n/a
2-D Filtered	phase	Chip #3	DTW	-0.3	0.038	-0.36	-0.34	0.035	0.12	0.17	0.15	0.55	-2.6 dB	2200	180	396	0.61	11 %	241
1-D Azimuth Filtered	phase	Chip #1	ship	-0.46	1.31	1.00	0.91	0.17	1.51	1.46	1.47	0.93	-0.3 dB	700	120	84	0.68	18 %	57
1-D Azimuth Filtered	phase	Chip #1	DTW	0.67	0.34	1.00	0.91	0.17	0.26	0.33	0.31	0.47	-3.3 dB	2200	140	308	0.59	9 %	183
1-D Azimuth Filtered	phase	Chip #1	Dark Kelvin Arm	0.68	0.23	1.00	0.91	0.17	0.25	0.32	0.30	0.58	-2.4 dB	2000	120	240	0.61	11 %	147
1-D Azimuth Filtered	phase	Chip #1	Brt Kelvin Arm	0.98	0.16	1.00	0.91	0.17	0.08	0.02	0.04	0.21	-6.7 dB	2120	96	204	0.54	4 %	110
1-D Range Filtered	phase	Chip #1	ship	0.10	0.6	1.00	0.91	0.084	0.89	0.90	0.90	1.18	0.7 dB	700	120	84	0.72	22 %	61
1-D Range Filtered	phase	Chip #1	DTW	0.73	0.12	1.00	0.91	0.084	0.20	0.27	0.25	0.88	-0.5 dB	2200	140	308	0.67	17 %	207
1-D Range Filtered	phase	Chip #1	Dark Kelvin Arm	0.71	0.14	1.00	0.91	0.084	0.22	0.29	0.27	0.89	-0.5 dB	2000	120	240	0.67	17 %	161
1-D Range Filtered	phase	Chip #1	Brt Kelvin Arm	0.98	0.07	1.00	0.91	0.084	0.08	0.02	0.04	0.45	-3.4 dB	2120	96	204	0.59	9 %	120
Filtered & aligned	phase	Chip #3	ship	2.42	0.16	-0.36	-0.34	0.04	8.12	7.72	7.84	14.15	11.5 dB	480	120	58	1.00	50 %	58
Filtered & aligned	phase	Chip #3	Kelvin Arms	-0.39	0.032	-0.36	-0.34	0.04	0.15	0.08	0.10	0.75	-1.3 dB	2200	96	211	0.65	15 %	136
Filtered & aligned	phase	Chip #3	DTW	-0.30	0.038	-0.36	-0.34	0.04	0.12	0.17	0.15	0.55	-2.6 dB	2200	180	396	0.61	11 %	241
Filtered & aligned	phase	Chip #4	Land	-0.019	0.020	-0.37	-0.40	0.04	0.95	0.95	0.95	6.68	8.3 dB	900	300	270	1.00	50 %	270
Filtered & aligned	phase	Chip #4	Shadow current	-0.26	0.042	-0.37	-0.40	0.04	0.35	0.30	0.31	1.77	2.5 dB	2800	1200	3360	0.81	31 %	2729
Filtered & aligned	phase	Chip #5	Small Ships	-0.26	0.048	-0.37	-0.34	0.03	0.24	0.30	0.28	1.07	0.3 dB	500	32	16	0.70	20 %	11
Filtered & aligned	phase	Chip #6	Linear Wake	-0.31	0.080	-0.36	-0.39	0.03	0.21	0.14	0.16	0.75	-1.2 dB	2000	65	130	0.65	15 %	84
Filtered & aligned	phase	Chip #7	ship	0.33	0.082	-0.36	-0.34	0.08	1.97	1.92	1.93	4.27	6.3 dB	120	48	6	0.98	48 %	6
Filtered & aligned	phase	Chip #7	Linear Wake	-0.16	0.062	-0.36	-0.34	0.08	0.47	0.50	0.49	1.17	0.7 dB	1200	40	48	0.72	22 %	35
Filtered & aligned	phase	Chip #8	Land	-0.008	0.020	-0.36	-0.31	0.05	0.97	0.98	0.98	4.65	6.7 dB	n/a	n/a	n/a	0.99	49 %	n/a
Filtered & aligned	phase	Chip #8	Tidal current	0.21	0.12	-0.36	-0.31	0.05	1.68	1.58	1.61	3.15	5.0 dB	n/a	n/a	n/a	0.94	44 %	n/a
Filtered & aligned	RCS	Chip #3	ship	17.5	8.63	3.12	4.03	2.08	3.34	4.81	4.23	1.26	1.0 dB	100	60	6	0.74	24 %	4
Filtered & aligned	RCS	Chip #3	Kelvin Arms	4.87	1.39	3.12	4.03	2.08	0.21	0.56	0.46	0.24	-6.2 dB	900	50	45	0.55	5 %	25
Filtered & aligned	RCS	Chip #3	DTW	3.17	1.34	3.12	4.03	2.08	0.21	0.02	0.08	0.25	-6.0 dB	1720	168	289	0.55	5 %	159
Filtered & aligned	RCS	Chip #4	Land	40	24	2.12	1.12	1.46	34.71	17.87	22.92	1.53	1.8 dB	560	320	179	0.78	28 %	139
Filtered & aligned	RCS	Chip #4	Shadow current	1.25	0.29	2.12	1.12	1.46	0.12	0.41	0.32	0.07	-11.3 dB	n/a	n/a	n/a	0.51	1 %	n/a
Filtered & aligned	RCS	Chip #5	Small Ships	44.1	36.8	2.12	4.48	0.79	8.84	19.80	16.51	1.05	0.2 dB	200	40	8	0.70	20 %	6
Filtered & aligned	RCS	Chip #6	Linear Wake	4.52	1.36	4.3	3.42	0.78	0.32	0.05	0.13	0.51	-2.9 dB	2000	55	110	0.60	10 %	66
Filtered & aligned	RCS	Chip #7	ship	8.25	2.28	4.3	2.1	1.02	2.93	0.92	1.52	1.86	2.7 dB	60	40	2	0.82	32 %	2
Filtered & aligned	RCS	Chip #7	Linear Wake	1.88	0.43	4.3	2.1	1.02	0.10	0.56	0.43	0.15	-8.2 dB	600	20	12	0.53	3 %	6
Filtered & aligned	RCS	Chip #8	Land	37	18.7	4.3	0.75	0.31	48.33	7.60	19.82	1.91	2.8 dB	n/a	n/a	n/a	0.83	33 %	n/a
Filtered & aligned	RCS	Chip #8	Tidal current	0.9	0.54	4.3	0.75	0.31	0.20	0.79	0.61	0.18	-7.5 dB	n/a	n/a	n/a	0.54	4 %	n/a

Appendix F. CFAR Detection Results

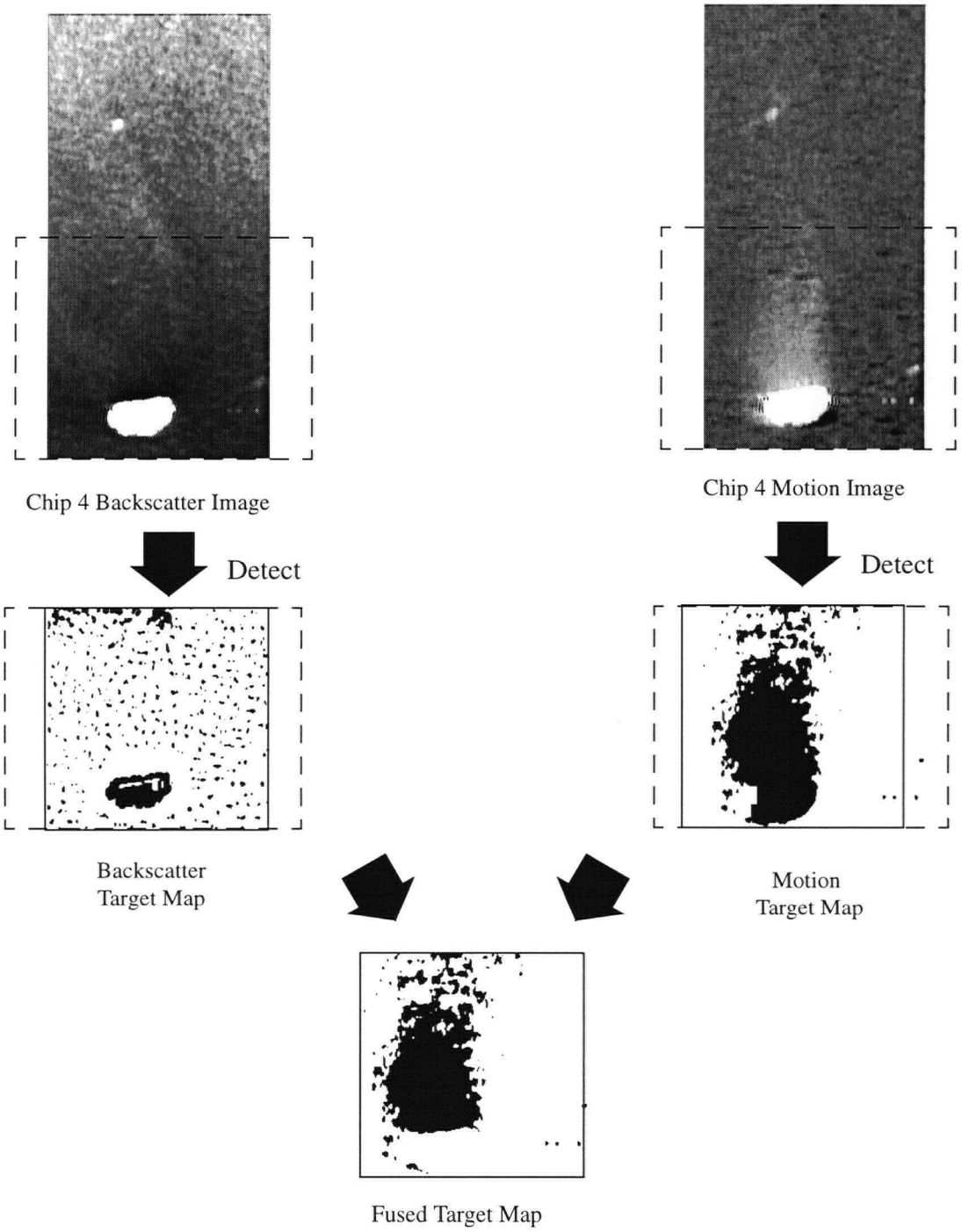

Figure A.1. Detector Output and Fused Output Images of Chip 4

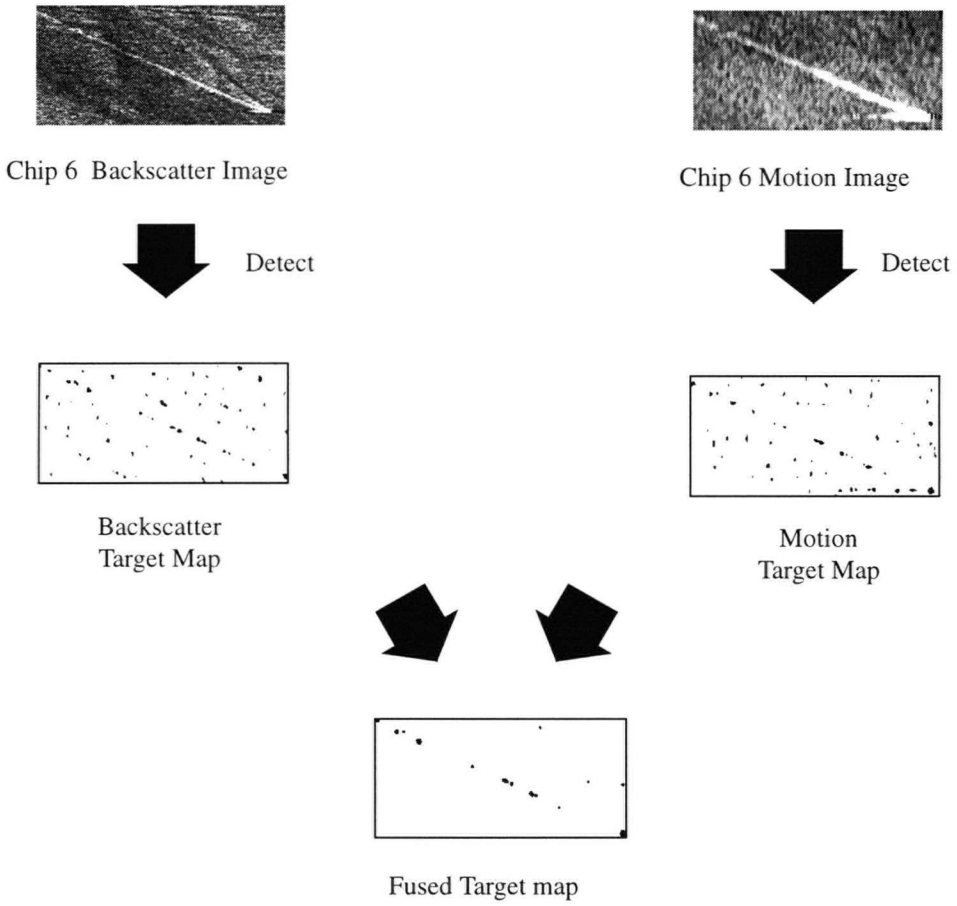

Figure A.2. Detector Output and Fused Output Images of Chip 6

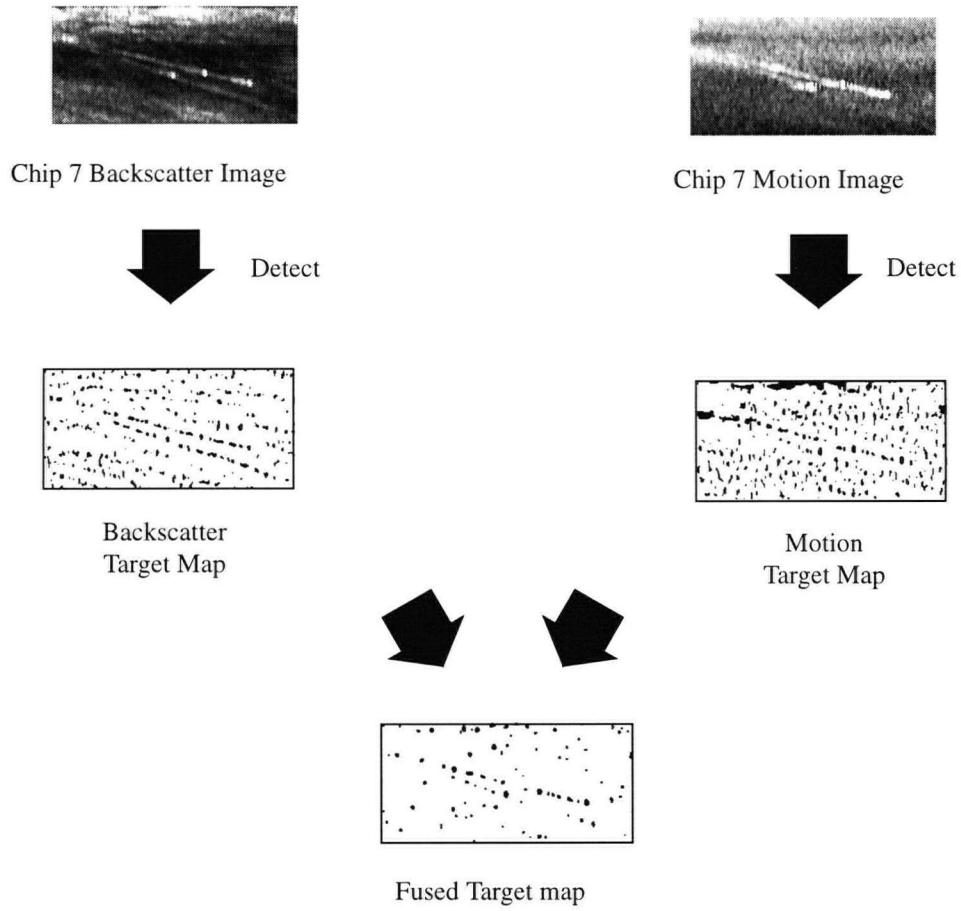

Figure A.3. Detector Output and Fused Output Images of Chip 7

Bibliography

[1] T. Ngo & I.G. Cumming, Technical Note 1: Literature Survey, submitted under DREO contract PWGSC 39V.W7714-5-9889

[2] T. Ngo & I.G. Cumming, Technical Note 2: Analysis of Coregistration Methods and Production of Interferograms for Airborne ATI, submitted under DREO contract PWGSC 39V.W7714-5-9889, March 1996

[3] T. Ngo & I.G. Cumming, Technical Note 3: Comparison of Magnitude and Phase Representation of Ship Wake Features in ATI Interferograms, submitted under DREO contract PWGSC 39V.W7714-5-9889, May 1996

[4] T. Ngo & I.G. Cumming, Technical Note 4: Parametric Analysis of C-band SAR Along-Track Interferometers, submitted under DREO contract PWGSC 39V.W7714-5-9889, Oct 1996

[5] T. Ngo & I.G. Cumming, Final Report: SAR Along-Track Interferometry for Enhanced Vessel Wake Detection, submitted under DREO contract PWGSC 39V.W7714-5-9889, July 1996

[6] H. Shnitkin, Joint STARS Phased Array Radar Antenna, *Proceedings of the IEEE Antennas and Propogation symposium*, 1994.

[7] R.M. Goldstein and H.A. Zebker, Interferometric radar measurements of ocean surface currents. *Nature* (328), 1987.

[8] A.K. Jain, Fundamentals of Digital Image Processing, Prentice-Hall, Inc., 1989.

[9] R.J. Tough and K.D. Ward, Detection of Sea Surface Features by Coherent Radar. *IEE Colloquium (1990) No. 182 Monitoring the Sea.*

[10] Geomatics Canada brochure, Canada Centre For Remote Sensing Airborne C/X-SAR, Copyright Minister of Supply and Services Canada 1994, Cat No. M77-42/1994E.

[11] A.L. Gray, M.W.A. van der Kooij, K.E. Mattar and P.J. Farris-Manning. Progress in the Development of the CCRS Along-Track Interferometer. *Proceedings of the International Geoscience and Remote Sensing Symposium*, 1994, Pasadena, USA.

[12] C.E. Livingstone, A.L. Gray, P.W. Vachon, M. Lalonde, R.K. Hawkins,T.I. Lukowski, K. Mattar, J.W. Campbell, The Canadian Airborne R&D SAR facility: The CCRS C/X SAR, *Proceedings of the International Geoscience and Remote Sensing Symposium*, 1996, Lincoln, USA.

[13] W.H. Press, S.A Teukolsky, W.T. Vetterling, B.P. Flannery, Numerical Recipes in C. The Art of Scientific Computing, Second Edition. Cambridge University Press, Reprinted 1995, p. 113-116

[14] R. Bamler and R. Hanssen, Decorrelation Induced by Interpolation Errors in InSAR Processing, *Proceedings of Int'l Geoscience and Remote Sensing Symposium 1997, Singapore.*

[15] H.A. Zebker and J. Villasenor, Decorrelation in Interferometric Radar Echoes, *IEEE Transaction on Geoscience and Remote Sensing* 30(5), Sept 1992.

[16] A. Monti Guarnieri, Residual SAR Focusing: An Application to Coherence Improvement, *IEEE Transaction on Geoscience and Remote Sensing* 34(1), Jan 1996.

[17] K. Ouchi and D.A. Burridge, Resolution of a Controversy Surrounding the Focusing Mechanisms of Synthetic Aperture Radar Images of Ocean Waves. *IEEE Transaction on Geoscience and Remote Sensing* 32(5), September 1994.

[18] J.C. Curlander, Synthetic Aperture Radar: Systems and Signal Processing, John Wiley & sons, Inc, 1991.

[19] D.R. Thompson and J.R. Jensen, Synthetic Aperture Radar Interferometry Applied to Ship Generated Internal Waves in the 1989 Loch Linnhe Experiment. *Journal of Geophysical Research,* 91 (B5), p. 4993-4997, 1990

[20] C. Elachi, Spaceborne Radar Remote Sensing: Applications and Techniques, IEEE Press, New York, 1989.

[21] R. Carande, Estimating Ocean Coherence Time Using Dual-Baseline Interferometric Synthetic Aperture Radar. *IEEE Transaction on Geoscience and Remote Sensing* 32(4), July 1994.

[22] E. Jakeman and P.N. Pusey, A Model for Non-Rayleigh Sea Echo. *IEEE Transaction on Antennas and Propagation* 24(6), Nov 1976.

[23] R.J. Tough, D. Blacknell, S. Quegan, Estimators and Distributions in Single and Multi-look Polarimetric and Interferometric Data. *Proceedings of Int'l Geoscience and Remote Sensing Symposium 1994,* Pasadena, USA.

[24] R.S. Raghavan, A Method for Estimating Parameters of K-Distributed Clutter. *IEEE Transaction on Aerospace and Electronic Systems* 27(2), Mar 1991.

[25] J.S. Lee, A.R. Miller and K.W. Hoppel, Statistics of phase difference and product magnitude of multi-look processed Gaussian signals. Waves in Random Media 4, 1994.

[26] J. Minkoff, Signals, Noise and Active Sensors: Radar Sonar, Laser Radar. John Wiley & Sons, Inc, 1992.

[27] N. C. Currie, Radar Reflectivity Measurement: Techniques and applications. Artech House, 1989.

[28] E. Rodriguez and J.M. Martin, Theory and design of interferometric synthetic aperture radars, *IEE Proceedings-F 139(2), Apr 1992.*

[29] Personal Communication, P.W. Vachon, CCRS

[30] P.W. Vachon, J.W.M. Campbell, C. Bjerkelund, F.W. Dobson, M.T. Rey, Validation of Ship Detection by RADARSAT SAR, *Proceedings of PORSEC 96*, Aug 1996

[31] M. Bao, C. Bruning and W. Alpers, On the Nonlinear Imaging of Two-Dimensional Ocean Surface Wave Fields by Interferometric SAR, *Proceedings of the International Geoscience and Remote Sensing Symposium*, 1995, Florence, Italy.

[32] W. Alpers, SAR Imaging of Ocean Waves - A Review, *Proceedings of the International Geoscience and Remote Sensing Symposium*, 1992, Houston, USA.

[33] B.A. Hughes, Effect of the Kelvin Wake Transverse Wake Component on SAR Imagery of Surface Wave Wake.

[34] F. E. Nathanson, J. Reilly and M. Cohen, Radar Design Principles. McGraw-Hill, 1990.